Optogenetic Methods for Spatiotemporally Resolved Observation of H_2O_2 in Biological Systems

Justin Lee

A dissertation

submitted in partial fulfillment of the

requirements for the degree of

Doctor of Philosophy

University of Washington

2024

Reading Committee:
Andre Berndt
Charles Chakvin
David L. Mack
Patrick M. Boyle

Program Authorized to Offer Degree:

Molecular Engineering and Sciences

© Copyright 2024

Justin Lee

University of Washington

Abstract

Optogenetic Methods for
Spatiotemporally Resolved Observation of H_2O_2 in Biological Systems

Justin Lee

Chair of the Supervisory Committee:

Andre Berndt

Department of Bioengineering

While hydrogen peroxide (H_2O_2) is widely recognized as a key redox signaling molecule essential for normal cellular functions, its supraphysiological accumulation is associated with the pathogenesis and progression of various diseases—including atherosclerosis, Duchenne muscular dystrophy (DMD), Alzheimer's disease, and cancer—making it a primary target of antioxidative therapeutics. Due to its significant physiological role, precise understanding of peroxide dynamics at both intracellular and intercellular levels is crucial for effective and safe therapeutic discovery. Developing tools that enable site-specific and real-time detection of H_2O_2 in cells and model organisms is therefore essential.

Guided by experimental and computational structural analyses, we engineered oROS, a multicolor fluorescence sensor suite for highly sensitive, real-time, *in situ* detection of H_2O_2. From human stem cell-derived models to animal models, oROS sensors demonstrate robust functionality in clinically relevant systems for studying peroxide biology. For instance, oROS elucidated the therapeutic efficacy of a putative antioxidative agent for Alzheimer's disease and detected H_2O_2 signals *in vivo* to validate the NADPH

oxidase-dependent opioid receptor inactivation mechanism in a systemic context. Furthermore, its multiplexed use with calcium and redox potential indicators enabled time-locked monitoring of H_2O_2 in relation to its key interactants. Lastly, oROS sensors were targeted to various subcellular compartments, including microdomains near the inner and outer plasma membranes, providing unprecedented precision in monitoring membrane H_2O_2 topology. We envision that oROS and its applications will stimulate new questions and discoveries in redox biology and medicine.

Table of contents

Acknowledgement

Firstly, I would like to express my deepest gratitude to my thesis advisor, Dr. Andre Berndt. I will forever be grateful for your mentorship and guidance, which have shaped me as a scientist, engineer, and individual. You have been not only an exceptional teacher but also a remarkable role model. It has been an honor to join your lab during its early days, to witness, and be part of, the groundbreaking discoveries and developments emerging from the Berndt Lab. I look forward to the future accomplishments you and your team will achieve, and I am proud to have been part of this journey. I will miss our daily scientific discussions, as well as the many small conversations about food, movies, games, the world, and our lives. Thank you for the trust and confidence you have placed in me throughout this process. I hope that one day I can become a mentor as you have been to me.

I would also like to extend my heartfelt thanks to my committee members for their guidance and support. Dr. Charles Chavkin, thank you for your initiative, continuous support, and invaluable guidance throughout this doctoral thesis project. Dr. David L. Mack, thank you for being a steadfast supporter of my academic journey even before I began my doctoral studies. Dr. Patrick M. Boyle, thank you for your critical insights and feedback, which ensured the rigor and excellence of my dissertation research. Dr. Ronald Y. Kwon, thank you for your support to ensure successful completion of my doctoral study and for providing me with the proper guidance during this strenuous process.

A special thank you to Dr. Michael Rappleye and Sarah J. Wait for being amazing colleagues and even better friends. Working with you both was foundational for the work described in this dissertation. I always found inspiration and joy in our work together. The same goes for my wonderful Berndt Lab colleagues—Jeanot Muster, Lily Torp, Yuxuan Wang, and others. This work would not have been possible without my incredible mentees: Yihan Wang, Amanda Nguyen, Shani Zuniga, Aida Moghadasi, and Vedant Chavan. Thank you for your patience, and for helping me grow as both a mentor and a scientist. I am

immensely proud of your remarkable achievements, and it has been an honor to work with such passionate, intelligent, and kind individuals. I would like to thank Netta Smith for being the backbone of the lab. Your excellence and rigor in both experimental work and administrative support fueled my creativity and productivity, especially during the challenges of the pandemic. Your contributions were truly indispensable.

I would like to thank my friends and colleagues within the scientific community—Dr. Changho Chun, Dr. Jongseob Choi, Juyoung Seong, Kyunghoon Kim, Yu Jung Shin, Dr. Junghyun Lee, Dr. Hyejin Kim, and Dr. Jaepil Kim. I am also deeply grateful to my amazing friends—Sam Colby, James Jo, Sungjun Hong, Seok-Jin Lim, Myungkyu Lee, and many others. A special thank you to Pastor Youshin Kim and the True Light Church for your prayers and unwavering support. My heartfelt gratitude goes to Dr. Hyunjung Lee and Dr. Jinah Jang for being the strongest supporters of my academic journey.

I would like to express my deepest thanks to my family, who have been my greatest advocates and support in pursuing my passion for science. In particular, I thank my mother, Kyung Hye An, the strongest and wisest person I know, who has sacrificed so much and given everything for me to become who I am today. Thank you to my father, Jin Suk Lee, whose courage has inspired me to believe that nothing is impossible. To my brother, Jiho Lee, thank you for always being a constant source of inspiration. I am also deeply grateful to my grandmother, Byungwi Min, for instilling my passion for biomedical science and for her prayers. Looking back, I realize that having such incredible people—both listed and not listed above—by my side has been the greatest blessing of this journey. I thank God for allowing me to be surrounded by these wonderful individuals and for shaping me through them in my life.

Chapter 1. Introduction

1.1. H_2O_2 in biology and disease.

1.1.1. Need for precision in ROS measurement.

The emergence of biological machinery capable of utilizing oxygen as a terminal electron acceptor in the electron transport chain marked a pivotal evolutionary milestone, closely aligning with the rise and diversification of complex life[1,2]. This advancement in cellular respiration, however, came with the production of Reactive Oxygen Species (ROS), a collective term encompassing various oxygen derivatives that are normal attributes to aerobic metabolism. Supraphysiological levels of Reactive Oxygen Species (ROS), whether as primary or secondary contributors to pathogenesis, are commonly associated with injuries and diseases. Moreover, high reactivity of ROS can damage biomolecules such as nucleic acids, lipids, and proteins, often casting them as harmful agents to biological systems. However, advancements in redox biology have shown that endogenous ROS are tightly regulated by cellular redox networks and play essential roles as regulators in various cellular processes. Failure of this tight regulatory system often leads to pathological outcomes, known as oxidative stress, observed in traumatic tissue injury, neurological and muscular degeneration, cancer, cardiovascular diseases and so much more. Despite its significance, targeting redox regulation for therapeutic outcome is challenging, and antioxidative therapeutic candidates have been unsuccessful in preclinical and clinical trials. Consequently, experts call for improved precision in analytic methods and how we view ROS in a biological system. Specifically, identifying systemic elevation of ROS and oxidative stress as a causal variable is discouraged. Instead, it is recommended to chemically specify **(molecular specificity)** the oxidative agent involved in the paradigm and their source and sink with subcellular detail **(locality)**.

1.1.2. H_2O_2 in physiology.

Superoxide is a primary form of ROS molecule in aerobic metabolism generated via NADPH oxidase, mitochondrial electron transport and numerous enzymes compartmentalized for local superoxide production.

However, superoxides are dismutases into H_2O_2 enzymatically (e.g. superoxide dismutase) and naturally due to their highly reactivity, and overall cellular concentration of superoxide is several order of magnitude lower than the concentration of H_2O_2. Owing to its stability, H_2O_2 is maintained at 1~100nM and its cellular level is tightly controlled by more than 40 enzymes[3]. Like Ca^{2+}, H_2O_2 acts as a secondary messenger participating in redox regulation of biological activities[3]. Steady-state physiological flux of H_2O_2 to specific protein targets leads to reversible oxidation, thereby altering protein activity, localization and interactions, which contributes to orchestration of various processes in cells and organs, including cell proliferation, differentiation, migration and angiogenesis[3]. For example, H_2O_2 regulates glucose transport activation in mammalian skeletal muscle. Specifically, In the absence of insulin, H_2O_2 at low micromolar concentrations activates the canonical IRS-1/PI3K/Akt insulin signaling pathway, along with other pathways like AMPK and p38 MAPK, to enhance basal glucose transport activity[4]. Conversely, H_2O_2 antagonizes the insulin signaling pathway by recruiting serine/threonine kinases contributing to insulin resistance[4]. H_2O_2 local plasma membrane H_2O_2 to be highly involved in modulation of diverse membrane receptor modulation, and distinct microdomain of H_2O_2 pool proximal to inner plasma membrane was reported[5–7]. In development, H_2O_2 plays an important role in cell morphogenesis and differentiation. For example, stem cells maintain a low basal (1-10nM) level of H_2O_2, which increases with differentiation[8]. This fine redox homeostasis maintains stem cell function and balances the cell among quiescence, proliferation, and differentiation state. In addition, H_2O_2 plays a vital role in neuronal growth and development[9,10]. At physiological levels, H_2O_2 supports the growth of both axons and dendrites, contributing to balanced neural development. A moderate increase in H_2O_2 concentration has been linked to enhanced dendritic growth, particularly relevant for axonal regeneration following injury. However, excessive H_2O_2 levels trigger oxidative stress, perturbing axonal growth and subsequent degeneration. Intriguingly, insufficient H_2O_2 levels also hinder neuronal development, exemplifying the importance of maintaining appropriate H_2O_2 levels for physiological neural function.

1.1.3. H_2O_2 in pathology.

The pathological roles of hydrogen peroxide (H_2O_2) are multifaceted, contributing to disease development both through oxidative damage and through interference with signaling pathways. Supraphysiological level of H_2O_2 leads to oxidative stress, where excessive accumulation of H_2O_2 overwhelms the cellular antioxidant defenses. This phenomenon is a hallmark of many conditions, including cardiovascular disorders, neuromuscular degenerative disorders, and cancer. In Alzheimer's disease, oxidative stress resulting from elevated H_2O_2 levels is known to exacerbate key pathological features such as amyloid-beta aggregation, tau hyperphosphorylation, and synaptic dysfunction[11–13]. Reactive astrocytes in the brain, which overproduce H_2O_2 via monoamine oxidase-B (MAO-B), contribute to heightened neuroinflammation and neuronal degeneration[14]. Notably, MAO-B, located on the outer mitochondrial membrane, has a distinct ability to directly influence cytoplasmic redox dynamics, making its pathological effects potentially pronounced[15]. This highlights the importance of considering both the levels and spatial origin of H_2O_2 when examining its role in disease. At lower concentrations, H_2O_2 can still "disrupt" cellular function by interfering with redox-sensitive signaling processes leading to undesirable physiological outcomes. For instance, NADPH oxidases (NOX) produce H_2O_2 in a G-protein-driven pathway, which has been linked to the inactivation of mu-opioid receptors (MORs) through a mechanism independent of β-arrestin-mediated desensitization[6,16]. Opioid overdose is one of the biggest challenges to public health. To address this crisis, we need to understand opioid receptor activation and delineate its downstream effects in more detail. Recent research has focused on biased MOR agonists, such as morphine, which preferentially activate G-protein pathways to produce pain relief with reduced side effects like respiratory depression[17]. However, the same pathway has been shown to lead to MOR inactivation through NOX-derived H_2O_2, challenging the assumption that G-protein signaling alone is a safer alternative[6]. This redox-mediated disruption likely contributes to opioid tolerance and decreased receptor responsiveness, complicating efforts to design effective and sustainable pain management strategies. These distinct roles of H_2O_2—as both a driver of oxidative damage and a disruptor of signaling—highlight its central role in disease

processes. Effective therapeutic approaches must address not only the excessive production of H_2O_2 but also its ability to interfere with critical cellular pathways. A deeper understanding of how H_2O_2 contributes to disease at both high and low levels will inform the development of targeted treatments for conditions ranging from neurodegeneration to opioid use disorders.

1.2. Molecular methods and unmet needs for probing H_2O_2 dynamics *in situ.*

An ideal H_2O_2 monitoring tool should enable the detection of spatially specific production of H_2O_2 within various intracellular compartments of cells, such as the plasma membrane, cytoplasm, mitochondria, and nucleus. Additionally, the tool should allow targeted expression to facilitate monitoring in a systemic context across multiple cell types, including organoids, tissue-on-a-chip systems, *ex vivo* tissues, and *in vivo* models. Most synthetic tracers for H_2O_2 detection fall short of meeting these requirements due to their short working time windows, low sensitivity, and limited specificity. These drawbacks make it challenging to accurately monitor intracellular H_2O_2 dynamics over extended temporal periods[18]. For instance, boronate-based probes[19,20], some of which are commercially available, are among the preferred small-molecule tracers. However, these probes require rigorous controls to confirm specificity for H_2O_2, and their sensitivity is inadequate for detecting physiological H_2O_2 levels. Similarly, Amplex Red, in combination with horseradish peroxidase (HRP), can be used to measure H_2O_2 released from cells, provided that other reducing agents or competing peroxidase substrates are absent[18].

Optogenetic H_2O_2 sensors overcome the shortcomings of synthetic dyes, as they can be genetically targeted to specific cell subtypes and intracellular compartments. For instance, the roGFP sensor family fuses roGFP, a redox-sensitive GFP variant, with hydrogen peroxide-specific enzymes such as Orp1 (thiol peroxidase) or Tsa2 (typical 2-Cys peroxiredoxin) from yeast. This fusion enables H_2O_2-specific fluorescence changes through a redox relay mechanism[21,22]. Similarly, the HyPer sensor family relies on the direct fusion of a circularly permuted fluorescent protein to the regulatory domain of the bacterial H_2O_2 sensor protein OxyR[23–28]. This design achieves H_2O_2-specific fluorescence changes through conformational coupling. **Although both**

sensor classes have been instrumental in advancing the field of redox biology, they exhibit certain limitations, such as incompatibility with mammalian expression systems, restricted spectral flexibility, and undesired photoswitching properties. These issues have hindered their widespread application, highlighting the need for further optimization to expand their utility.

Chapter 2. Engineering of a Fast Genetically Encoded Sensor for Real Time H_2O_2 Monitoring.

- This chapter has been published in the following manuscript

Lee JD, Won W, Kimball K, Wang Y, Yeboah F, Evitts KM, Neiswanger C, Schattauer S, Rappleye M, Bremner SB, Chun C., Smith N, Mack DL, Young JE, Lee CJ, Chavkin C, Berndt A. Structure-guided engineering of a fast genetically encoded sensor for real-time H_2O_2 monitoring.

https://doi.org/10.1101/2024.01.31.578117 (bioRxiv: 2024 Feb 4.)

2.1. Abstract

Hydrogen Peroxide (H_2O_2) is a central oxidant in redox biology due to its pleiotropic role in physiology and pathology. However, monitoring H_2O_2 in living cells and tissues in real time remains challenging. Here, we developed an optogenetic hydRogen perOxide Sensor (oROS) with improved kinetics over previous probes, leveraging a structure-guided approach that aimed to preserve the innate kinetics of its sensing domain ecOxyR. Our resulting green-fluorescent H_2O_2 sensor oROS-G exhibits faster off-kinetics while offering equivalent sensitivity compared to the peroxide sensor HyPer7. High sensitivity and fast on-and-off kinetics render oROS-G ideal for monitoring intracellular H_2O_2 dynamics over extended periods. We continuously tracked real-time transient and steady-state H_2O_2 levels in diverse biological systems for up to 40 hours, including human stem cell-derived neurons and cardiomyocytes, primary neurons and astrocytes, and mouse brains *ex vivo* and *in vivo*. These applications demonstrate oROS's capabilities to monitor H_2O_2 as a secondary response to pharmacologically induced oxidative stress and when adapting to varying metabolic stressors. We showcased use of the sensor in oxidative stress models of astrocytes, highlighting the sensor's relevance in validating neurodegenerative disease models. Lastly, we demonstrated the acute opioid-induced generation of H_2O_2 signals *in vivo*, highlighting a redox-based GPCR regulation mechanism. oROS is a versatile tool, offering a window

into the dynamic landscape of H_2O_2 signaling. Our findings provide new rationales for effective genetically encoded sensor engineering and expand the optogenetic sensor toolkit. These sensors can deepen our understanding of redox physiology, with significant implications for understanding diseases associated with oxidative stress, such as cancer, neurodegenerative, and cardiovascular diseases.

2.2. Introduction

Endogenous Reactive Oxygen Species (ROS) are indispensable components of aerobic metabolism, which hallmarks the rise of complex life[1,2]. Due to their damaging impact on biological macromolecules at high concentrations, redox homeostasis is tightly regulated in most aerobic systems, and high-level accumulation of ROS is often viewed as a pathogenic marker in degenerative diseases (e.g. Alzheimer's disease, Duchenne Muscular Dystrophy), tumorigenesis, and inflammation[29–32]. Furthermore, an increasing number of studies report the role of low-level ROS as a physiologic mediator in normal cellular signaling processes[33–35]. Specifically, H_2O_2 is a key redox signaling molecule, owing to its relative stability and ability to modify cysteine residues in proteins, enabling selective downstream signaling[36]. On the other hand, excessive H_2O_2 is a common pathological marker affecting phenotypic and disease progression in various cell types[14,37,38]. Nevertheless, limited analytic tools to spatiotemporally monitor specific oxidants in situ with precision have been a bottleneck to deciphering their specific role in physiology and the cause and effect of their imbalance[3,39]. Thus, methods to interrogate the role of H_2O_2 would be broadly applicable to the study of redox biology[39].

Most synthetic ROS-sensitive dyes are unsuited for these considerations because of their short working time window, low sensitivity, and low specificity[18]. Alternatively, protein-based peroxide sensors have been engineered to overcome these shortcomings. For example, the roGFP sensor family fuses roGFP, a redox-sensitive green fluorescent protein variant, to H_2O_2-specific enzymes like Orp1 (thiol peroxidase), or Tsa2 (typical 2-Cys peroxiredoxin) from yeast to achieve peroxide-specific roGFP fluorescence changes via redox relay[22,40]. The HyPer sensor family is based on the direct fusion of circularly permuted fluorescent protein (cpFP) to the regulatory domain of bacterial peroxide sensor protein OxyR for conformational coupling that

leads to H_2O_2-specific fluorescence change[23–28]. HyPer sensors either use nmOxyR (Neisseria meningitidis OxyR) or ecOxyR (Escherichia coli OxyR), the most extensively studied OxyR variant, as their sensing domain. Remarkably existing ecOxyR-based peroxide sensors exhibit slow oxidation kinetics (seconds under saturation conditions)[25,26,41], while studies reported peroxide-dependent oxidation of ecOxyR at a sub-second scale[42]. Based on our structural analysis, we hypothesized that the discrepancy stems from the disruption of structural flexibility in the sensors. Under this consideration, we developed oROS-G (optogenetic hydRogen perOxide Sensor, Green), an ecOxyR-based peroxide sensor with a green fluorescent reporter protein (GFP, excitation: 488 nm, emission: 515 nm). oROS-G exhibits faster kinetics, enabling the visualization of peroxide diffusion in cells and their environment. We also engineered oROS-Gr, a ratiometric variant of oROS-G by fusing it with mCherry, which improves monitoring precision by normalizing sensor fluorescence intensity to the H_2O_2 inert red fluorescence. Here, we present diverse use cases of oROS sensors to monitor steady-state and transient H_2O_2 levels in various model systems. Specifically, we showed how oROS can detect varying H_2O_2 levels in astrocytes in the context of Alzheimer's disease models and assessed the efficacy of a drug in reducing aberrant peroxide levels. Also, we investigated how different glucose levels can result in different intracellular oxidative environments in conjunction with mitochondrial respiratory depression. Lastly, we monitored opioid-dependent acute H_2O_2 generation in mouse brains both ex vivo and in vivo, demonstrating the potential utility of oROS sensors as a functional downstream reporter for G-protein-biased opioid receptor activation.

2.3. Results

2.3.1 Structure-guided engineering to improve sensitivity and kinetics of ecOxyR-based H_2O_2 sensor.

2.3.1.1. Rational engineering strategies for oROS-G.

ecOxyRs is an H_2O_2 sensor protein that regulates the transcription of antioxidative genes in response to low-level cellular H_2O_2 in *E.Coli*. The specificity of OxyR stems from its unique H_2O_2 binding pocket[43]. Previous studies have shown that binding H_2O_2 leads to an intermediate state that facilitates the disulfide bridging of two conserved cysteine residues (C199-C208, based on exOxyR-RD numbering[26]) which triggers

the transition into the oxidized conformational state of OxyR. Due to its characteristic as an H_2O_2 sensor with low scavenging capacity[43], OxyR is an ideal scaffold for building a protein-based H_2O_2 reporter. However, the slow kinetics of existing ecOxyR sensors[23,25–27,41] deviate from the reported ecOxyR properties. Hence, we revisited the sensor design **[Fig. 1A],** to create a green genetically encoded indicator for H_2O_2 with accelerated kinetics **[Supp. Fig. 1A].** OxyR-based peroxide sensors integrate circular permuted fluorescent proteins (cpFP) within the loop between residues C199 and C208. However, the crystal structure of oxidized ecOxyR [PDB:1I6A] predicted an evident peak of B-factor **[Fig. 1B]** indicating this loop region is more flexible than its surroundings. We hypothesized that inserting the cpFP in the region (e.g. in HyPer sensors) may increase the conformational entropy of the intermediate state that brings C199 and C208 into proximity[43]. We performed a pairwise residue distance analysis between oxidized and reduced ecOxyR structures and found that the region between residues 209-220 goes through noticeable peroxide-dependent conformational change **[Supp. Fig. 1B].** cpGFP insertion between residue 211 and 212 elicited a robust response (ΔF/Fo = 97.55%; confidence interval 95% (ci) = [96.6, 98.52]) to 300 μM extracellular peroxide in HEK293 cells, which fully oxidizes previous OxyR-based sensors[26] **[Supp. Fig. 1C].** The 211-212 variant exhibited a faster change in fluorescence in response to H_2O_2 (time from 25% to 75% max. sensor response = 1.06s; ci = [1.05, 1.07]) compared to other ecOxyR-based sensors[23,25,26,41]. Moreover, the variant showed improved response amplitudes (ΔF/Fo = 20.41%; ci = [19.62, 21.17]) to low peroxide levels (10 μM) compared to HyperRed (ΔF/Fo = 2.8%; ci = [2.61, 3.0]), the previously most sensitive H_2O_2 sensor derived from ecOxyR[26]. **[Supp Fig. 1D].** To further optimize the dynamic range of the 211-212 variant, we applied engineering principles from the calcium indicator GCaMP5[44], and introduced large and hydrophobic amino acid tyrosine at the residue sites proximal to the cpGFP opening to reduce solvent access. We found the E215Y mutation increased response amplitude (ΔF/Fo) by 2.1-fold at full oxidation (ci = [1.99, 2.26]) **[Supp. Fig. 1E]** and named this variant oROS-G **[Supp. Fig. 1A, 2]**. Furthermore, the H_2O_2-induced fluorescence increase was effectively disrupted by the C199S mutation. This confirms the sensor function is dependent on interactions at the C199-C208 pair consistent with the OxyR conformational

changes in response to peroxide **[Supp. Fig. 3A]**. We also confirmed the sensor activation is fully reversible following treatment with the reducing agent Dithiothreitol (10 mM, DTT) **[Supp. Fig. 3B]**.

Figure 1 Structure-guided engineering to improve sensitivity and kinetics of ecOxyR-based H_2O_2 sensor.

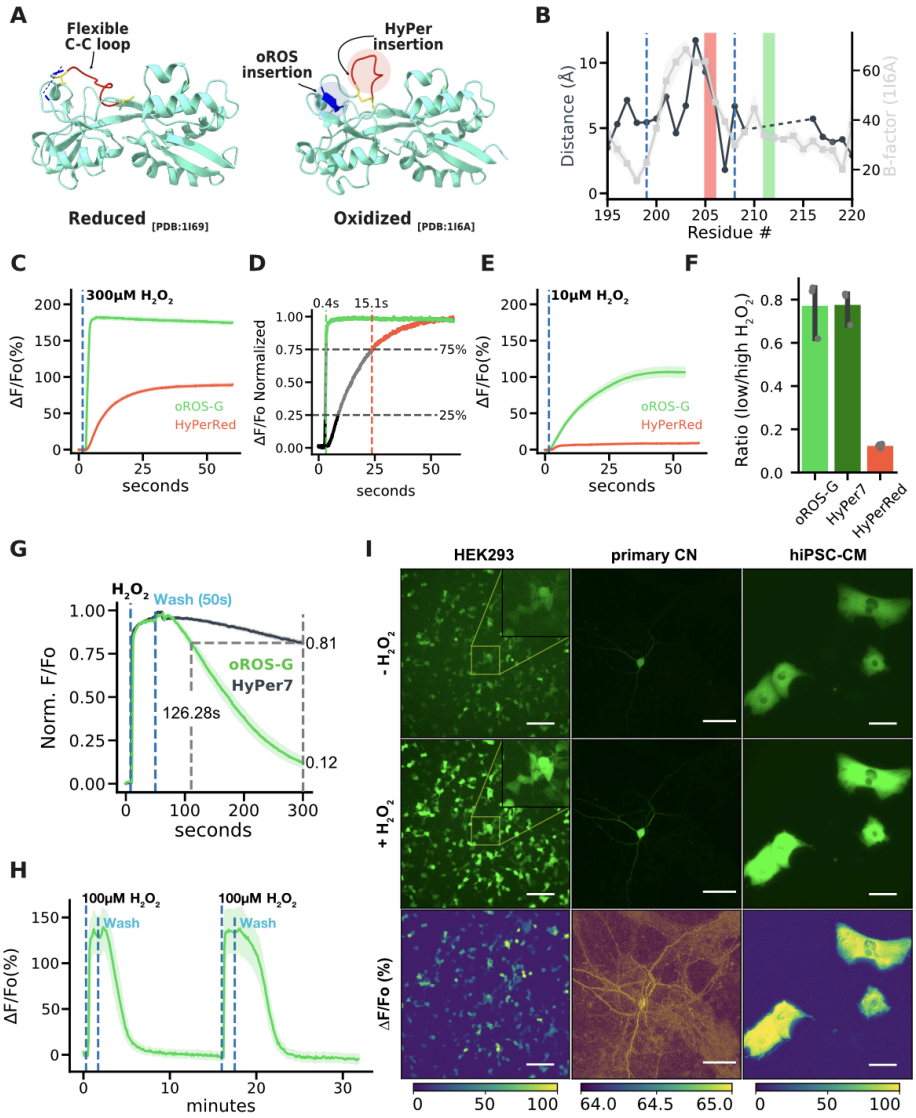

A-B Structure-guided design of an oROS sensor. **A** Crystal structure of reduced and oxidized forms of Regulatory Domain (RD) of *Escherichia coli* OxyR. C-C pair labeled in yellow. Red indicates the fluorescent protein insertion loop for HyPer sensors, and Blue indicates the newly identified fluorescent protein insertion site for oROS sensors. **B** Overlay of B-factor of oxidized OxyR structure and residue-to-residue distance plots for a zoomed-in view of the putative region with high conformational change between oxidized and reduced form of ecOxyR. The red and green boxes indicate the insertion sites of HyPerRed and oROS-G, respectively. The insertion site proposed for oROS-G is outside of the loop between C199 and C208 (blue dashed line) to maximize the flexibility of the loop. **C** Fluorescence responses of oROS-G and HyPerRed to 300 μM exogenous H_2O_2. The barplot represents the mean of the maximum fluorescent response of cells in ΔF/Fo (change of fluorescence over baseline). **D** On-kinetic analysis of oROS-G and HyPerRed. Representative trace of 300μM peroxide-induced saturation of both sensors with normalized ΔF/Fo. Vertical dotted lines represent 75% and 25% sensor activation, labeled with 25-75% activation completion time. 100% indicates full sensor saturation. **E** Fluorescence responses of oROS-G and HyPerRed to 10 μM exogenous H_2O_2. **F** Benchmark test of oROS-G, HyPerRed, and HyPer7 for their H_2O_2 sensitivity. Each sensor was expressed in HEK293 cells, and their ΔF/Fo were calculated for their responses to exogenous administration of either 300 μM (high) or 10

μM (low) H_2O_2. Bar plot represents the low/high response (10 μM/300 μM) ratio of each sensor. **G** Representative reduction kinetics of oROS-G and HyPer7 after 100 μM H_2O_2 stimulation followed by media wash (n>100 cells per sensor). **H** HEK293 expressing oROS-G were stimulated with 100 μM H_2O_2 followed by media wash. The sequence was repeated twice. **I** Expression of oROS-G in HEK293 (Scale bar: 100 μM), primary rat cortical neuron (Scale bar: 50 μM), and hiPSC-derived cardiomyocyte (Scale bar: 100μM), and their responses to 300μM H_2O_2 stimulation. **Descriptive statistics:** Error bars and bands represent the bootstrap confidence interval (95%) of the central tendency of values using the Seaborn (0.11.2) statistical plotting package. Cell-of-interests were collected from 3 biological replicates unless noted otherwise.

2.3.1.2. Characterization of kinetics and sensitivity of oROS-G in mammalian host systems.

We first characterized oROS-G sensor following expression in mammalian HEK293 cell cultures. Direct application of exogenous H_2O_2 increases intracellular H_2O_2 by diffusion across the plasma membrane through aquaporins, which creates a gradient of H_2O_2[45–47] across cell membranes. Under these conditions, the intracellular concentration of H_2O_2 is reported to be about 2 or 3 magnitudes lower than that of extracellular H_2O_2[26,48]. HyPerRed is the most sensitive sensor designed based on ecOxyR[26]. Thus, despite differences in spectral properties, we first sought to benchmark oROS-G against HyPerRed for their response to H_2O_2. The signal amplitude of oROS-G (ΔF/Fo = 192.34%; ci = [190.45, 194.23]) at saturation (300 μM H_2O_2) was ≈2-fold greater than that of HyPerRed (ΔF/Fo = 97.74%; ci = [96.52, 99.06]) **[Fig. 1C]** while oROS-G exhibited significant improvement in on-kinetics compared to HyPerRed with ≈23 times faster 25-75% ΔF/Fo kinetics *in situ* (oROS-G: 0.4 ; ci = [0.26, 0.51], HyPerRed: 9.19; ci = [8.92, 9.46]) **[Fig. 1D, Supp. Fig. 4]**. In addition, we observed a >7 times larger response at low-level peroxide stimulation (oROS-G: ΔF/Fo = 116.22%; ci = [110.85, 121.73] vs HyPerRed: ΔF/Fo = 16.45%; ci = [15.98, 16.95]) **[Fig. 1E]**. Improved sensitivity profile of oROS-G also found to be at equivalent level (i.e. 10 μM/300 μM exogenous H_2O_2 response ratio) compared to HyPer7, the newest iteration of HyPer sensor family **[Fig. 1F]**. oROS-G and HyPer7 take an fundamentally different approach to gain sensitivity as HyPer7 was designed by swapping the sensing domain with a more sensitive OxyR variant from *Neisseria meningitidis* (nmOxyR) with fluorescent reporter insertion contained to the C-C loop region **[Fig. 1F]**[28]. Intriguingly, oROS-G exhibited much faster off-kinetics in HEK293 cells while they both exhibit near-immediate response to saturating level of bolus H_2O_2 **[Fig. 1G]**. When both oROS-G and HyPer7 were activated with 100 μM H_2O_2 followed by media wash to measure

endogenous reduction kinetic in HEK293 cells, oROS-G reached ≈90% reduction from its maximum saturation in 4.17 minutes, whereas HyPer7 only achieved about ≈20% reduction from its full saturation in the same duration, consistent with previous studies. (HyPer7: 0.81; ci = [0.8, 0.82], oROS-G: 0.12; ci = [0.1, 0.15]) In contrast, oROS-G showed 2.63 times faster decay kinetics than HyPer7 based on the reduction time to 85% of the saturation level **[Fig. 1G, H, Supp. Fig. 5]**. Lastly, we confirmed the robust expression and function of oROS-G in rat cortical neurons and human-induced pluripotent stem cell-derived cardiomyocytes (hiPSC-CMs) demonstrating a versatile application range **[Fig. 1I]**.

2.3.2. Visualizing extracellular and intracellular diffusion H_2O_2 using oROS-G.

We exploited oROS-G's fast kinetics by visualizing H_2O_2 diffusion in the extracellular environment and in intracellular space in HEK293 cells. Due to its slower kinetics, the HyPerRed exhibits spatially uniform sensor activation across the field of view (660 x 660 μm) in response to exogenous H_2O_2 stimulation **[Fig. 2A]**. In contrast, oROS-G's faster response allowed the spatial H_2O_2 propagation to be visualized in the image field of view **[Fig. 2B]**. To better estimate the diffusion kinetics of the H_2O_2 propagation in the field-of-view, we transformed the time-series fluorescence profile into a time-series pixel-wise activation map that depicts when pixel intensity reached 50% of the observed maximum **[Supp. Fig 6 A, B]**. Convolution of the activation map perpendicular to the direction of H_2O_2 propagation revealed the speed of the H_2O_2 diffusion across the field-of-view to be ≈ 0.8 mm/s **[Fig. 2C]**. Next, we created a pixel-wise chronological activation map that depicts H_2O_2 diffusion kinetics within cells. **[Fig. 2D]**. Intriguingly, patterns of intracellular H_2O_2 entry were diverse, potentially representing aquaporin-driven passive transmembrane diffusion[46,49]. For example, we noticed cells exhibiting a radial entry pattern along their membranes **[Fig. 2Ei]**, while others displayed a more polarized entry pattern aligned with the direction of global H_2O_2 diffusion **[Fig. 2Eii]**. It was also revealed that neighboring cells were topologically distinguishable from each other, implying that H_2O_2 transport at the cell-to-cell junctions may also be limited by the abundance of the transporters present at the cell-cell interface **[Fig. 2Eiii]**. Taken together, visualization of bolus H_2O_2 exposure using oROS-G allowed real-time observation

of extra and intracellular peroxide diffusion. The significance of the heterogeneous intracellular H_2O_2 diffusive pattern could hint to potential factors, like aquaporins, that regulate H_2O_2 diffusivity within spatial contexts. These insights could support studies on how extracellular H_2O_2 build-up effects intracellular H_2O_2 pools[50].

Figure 2 Visualizing extracellular and intracellular diffusion H_2O_2 using oROS-G.

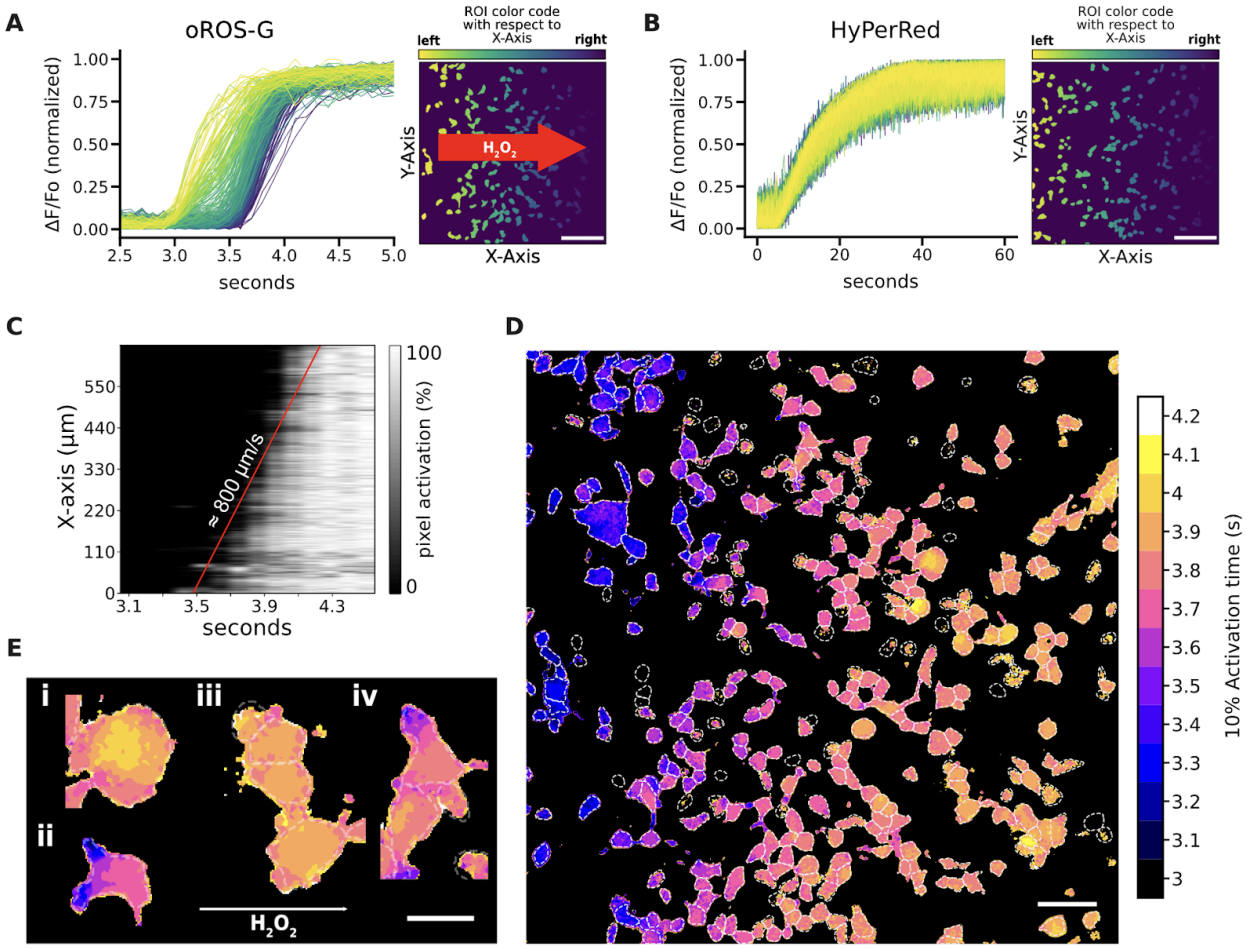

A-B Normalized (min-max scaled) fluorescence response of oROS-G **(A)** and HyPerRed **(B)** to 300µM H_2O_2 stimulation captured at 10Hz. Region-of-interests (ROI) were color-coded for their respective X-axis location. Scale bar = 150µm.Traces show oROS-G responses at varying locations along the X-axes. **C** Diffusion map derived from Fig. 2A. The image was transformed into an activation map that depicts the ratio of responding (i.e. activated) pixels along the x-axis over time. The map reveals the speed of the H_2O_2 diffusion to be ≈800µm/s. **D** Chronological pixel activation map of oROS-G expressing HEK293 cells. Colormap represents the time each pixel passes the 10% of the maximum threshold. Scale bar = 50µm. White dashed line: segmented cell outline. **E** Representative images of intracellular H_2O_2 diffusion. **(i)** radial diffusion **(ii)** polarized diffusion **(iii), (iv)** neighboring cell cluster. Scale bar = 25 µm. White dashed line: segmented cell outline.

2.3.3. Ratiometric variant oROS-Gr improves temporal flexibility of H_2O_2 measurement.

2.3.3.1. Design of oROS-Gr: a ratiometric variant of oROS-G for improved precision of long-term H2O2 monitoring.

We created oROS-Gr, by fusing mCherry to oROS-G, creating an equimolar reference point inert to H_2O_2. Flow cytometry analysis confirmed a strong linear correlation between green (Em. 510 nm) and red (Em. 605 nm) emission intensity of oROS-Gr expressed in HEK293 cells (n = 16,326) **[Fig. 3A]**. Thus, oROS-Gr can be used for long-term and non-continuous monitoring by calculating the green-to-red light emission ratio independent of sensor expression levels. Upon exogenous H_2O_2 stimulation, the oROS-Gr ratio (Em. 510/605) showed a dose-dependent response in HEK293 cells. (1 μM: 0.06 (n = 327); ci = [0.06, 0.06], 10 μM: 0.11 (n = 306); ci = [0.1, 0.11], 25 μM: 0.14 (n = 405); ci = [0.14, 0.14], 50 μM: 0.15 (n = 469); ci = [0.15, 0.15]) **[Fig. 3B]** In addition, the oROS-Gr green-to-red ratio predictably followed a sequence of exogenous H_2O_2 stimulation (100 uM) and DTT (10 mM) reduction **[Fig. 3C, Supp. Fig. 7]**. Menadione treatment has been widely used to model oxidative stress in biological systems [11,51–54] **[Supp. Fig. 8A]**. Still, studies to monitor its intracellular effect have been mostly limited to short time windows or non-continuous snapshots at varying time points, which do not enable insights into the real-time impact on redox homeostasis and its impact over a longer period. In HEK293 cells, oROS-G acutely responded to 10 μM and 50 μM menadione in a dose-dependent manner (ΔF/Fo, 10 μM: 89.56 %; ci = [81.79, 97.57], 50 μM: 173.68%; ci = [166.81, 180.35]) in HEK293 cells **[Supp. Fig. 8B].** The trend was consistent in human primary astrocytes **[Supp. Fig. 8C]**. Next, we continuously measured the effects of menadione on cellular H_2O_2 levels over a ten-hour time window in HEK293 cells. Initially, menadione at 0, 1, 10, and 50 uM induced acute dose-dependent elevation of H_2O_2. However, within 30 minutes, the H_2O_2 levels at 10 μM exposure were higher than those at 50 μM, which returned to a dose-dependent trend within four hours **[Fig. 3D]**. Further analysis of intracellular redox landscape analysis and the functional role of putative cellular antioxidative elements[55,56] is required to understand this phenomenon fully. Nevertheless, the impact of menadione on intracellular H_2O_2 levels demonstrates the

necessity to measure cellular oxidative stress at various time points. We also evaluated whether oROS-Gr improved the readout precision over oROS-G. We compared the coefficient of variation (CoV) of the ratiometric signal (Em. 510/605 ratio) against the single wavelength signal (Em. 510 nm) **[Fig. 3D, E].** The ratiometric readout showed about 2-fold lower CoV compared to the single wavelength mode, confirming improvements in precision [Ratiometric: 0.27 (n = 484), non-Ratiometric: 0.46 (n = 484)].

2.3.3.2. Glucose-dependent basal oxidation level in mammalian cells.

Superoxide and peroxide are continuously generated as byproducts of electron transfer during aerobic metabolism[57,58,59]. In this context, glucose, as one of the primary substrates of aerobic metabolic pathways, plays a crucial role in modulating cellular metabolic activity[60]. Intriguingly, low as well as high glucose levels were reported to result in depressed respiratory activity in cultured human podocytes[61]. The study also showed that the reduction of metabolic rates in high-glucose conditions can be reversed by incubation with the antioxidant N-acetyl cysteine (NAC), indicating that respiratory suppression is correlated with oxidative stress. Thus, we hypothesized that high glucose (HG = 25 mM) and low glucose (LG = 1 mM) media would result in higher basal peroxide levels than medium glucose (MG = 10 mM). We incubated HEK293 cells for 48 hours in HG, NG, and LG media and compared the ratiometric oROS-Gr signals. Here, low and high glucose conditions caused greater peroxide levels than MG (MG: 0.38; ci = [0.378, 0.382], LG: 0.402; ci = [0.4, 0.404], HG: 0.392; ci = [0.389, 0.394]). **[Fig. 3F].** We directly measured metabolic activities and found that basal and maximum respiratory rates were also the lowest under low and high glucose conditions **[Supp. Fig. 9A]**, indicating an inverse correlation with increased peroxide levels. Indeed, cells pre-incubated with 1 mM of the antioxidant NAC under HG conditions brought the oROS-Gr level 84% closer to MG conditions, indicating modest suppression of oxidative stress **[Supp. Fig. 9B].**

Figure 3 Ratiometric variant oROS-Gr improves temporal resolution of H_2O_2 measurement.

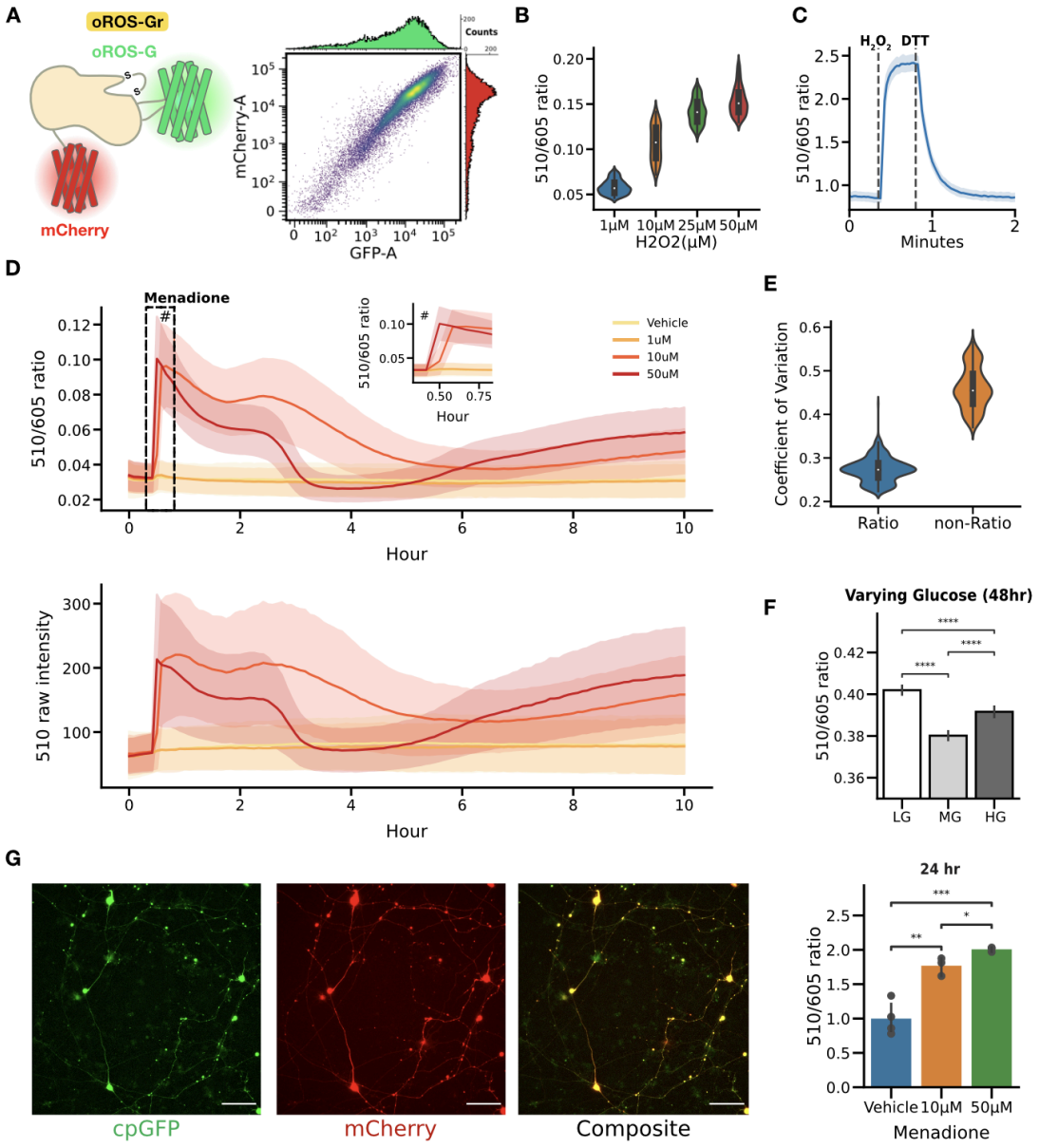

A ***left*** Schematic illustration of the oROS-Gr sensor design. oROS-Gr is an oROS-G variant with a C-terminus fusion of mCherry red fluorescent protein. ***right*** Flow cytometry result showed the linear relationship of green and red fluorescence levels of the oROS-G1r sensor expressed in HEK293 cells. **B** 510/605 nm emission ratio of oROS-Gr expressed in HEK293s stimulated with various concentrations of H_2O_2. Fluorescence emission ratios were captured a minute after the exposure. (n>100 cells per condition) **C** 510/605 nm emission ratio change of oROS-Gr during activation and reversal upon stimulation with 100 μM H_2O_2 and 10 mM DTT in HEK293 WT cells (n=82 cells). **D** Continuous (10 hours) monitoring of oROS-Gr stable cells in response to various concentrations of menadione (n>100 cells per condition). ***Top*** Ratio: 510/605 nm emission ratio of oROS-Gr ***Bottom*** Non-ratio: unnormalized 510 nm emission intensity profile. **E** Aggregated Coefficient of Variation (CoV) of 510/605 nm emission ratio and 510 nm emission intensity from Figure 4D. **F** Observation of glucose-level dependent basal oxidation level of oROS-Gr (510/605 ratio) in oROS-Gr stable cells. The cells were incubated in LG (low glucose, 1 mM), NG, and HG incubation for 48 hours after they were serum-deprived overnight. The sensors were least oxidized in NG, exhibiting a U-shape dose-dependent response (n>100 cells per condition). **G** Resting oROS-Gr ratio expressed in hiPSC-derived cortical neurons incubated in various levels of menadione for 24 hours. (n=3-4 wells per condition) **Descriptive statistics:** Error bars and bands represent the bootstrap confidence interval (95%) of the central tendency of values using the Seaborn (0.11.2)

statistical plotting package. Cell-of-interests were collected from 3 biological replicates unless noted otherwise. **Inferential statistics:** F - t-test independent samples. *P < 0.05, **P < 0.01, ***P < 0.001.

2.3.3.3. oROS-Gr in human stem cell-derived cardiomyocytes and cortical neurons.

We confirmed the robust expression and functionality of oROS-Gr in various human stem cell-derived cells. For example, we measured peroxide levels in hiPSC-derived cortical neurons in response to 24-hour 10 μM and 50 μM Menadione incubation to be 1.77-fold and 2-fold of oROS-Gr ratio observed at vehicle negative control, respectively (Vehicle: 1.0; ci = [0.82, 1.21], 10 μM: 1.77; ci = [1.62, 1.88], 50 μM: 2.01; ci = [1.97, 2.03]) **[Fig. 3G]**. Next, we used the sarcoendoplasmic reticulum calcium ATPase (SERCA) blocker cyclopiazonic acid (CPA, 10 μM) to elevate Ca^{2+} in the cytosol of hiPSC-cardiomyocytes (CM)[62]. When hiPSC-CMs expressed oROS-Gr, we measured increased cytosolic peroxide levels within 2 hours of CPA incubation **[Supp. Fig. 10].** As previously reported, this portrays a tight coupling between intracellular Ca^{2+} and ROS levels[63–66].

2.3.4. Monitoring the effect of antioxidants on intracellular peroxide level in Alzheimer's model.

Next, we explored using oROS-G in the context of antioxidants that target intracellular peroxides. N-acetyl-cysteine (NAC) is a cysteine prodrug widely used as a classical "antioxidant". Although its detailed mechanism of action has not been established, recent studies highlight its antioxidative role via the production of low-level sulfane sulfur species[67,68]. Using oROS-G, we measured the effect of NAC-dependent catabolism on cellular H_2O_2 levels in real-time. With a 1-hour preincubation of 1 mM NAC, oROS-G expressed in HEK293 showed a 73% diminished response to exogenous 10 μM peroxide exposure **[Supp. Fig. 11A]**. Similarly, we incubated oROS-G expressing HEK293 cells to either NAC (10 mM) or Vehicle (DMSO) for 20 minutes before 10 μM menadione exposure. NAC significantly attenuated the response by 72 percent **[Supp. Fig. 11B]**. We next examined the ability of the oROS-G sensor in primary cultured astrocytes to detect intracellular H_2O_2 levels to assess the H_2O_2-scavenging effects of molecules. Initially, we expressed oROS-G in the astrocytes and tested H_2O_2 concentration-dependent functionality **[Supp. Fig. 11C]**. We observed an increase of 21.3 ± 5.3%

and 57.7 ± 9.4% in fluorescence with 10 and 100 μM H_2O_2, respectively **[Supp. Fig. 11D-F]**, indicating a functional response of the oROS-G sensor in primary cultured astrocytes. Previously, we have shown that aberrant H_2O_2 production by reactive astrocytes, a pathological form of astrocytes, is a contributing factor to

Figure 4 Monitoring the effects of antioxidants on intracellular peroxide levels in an Alzheimer's model.

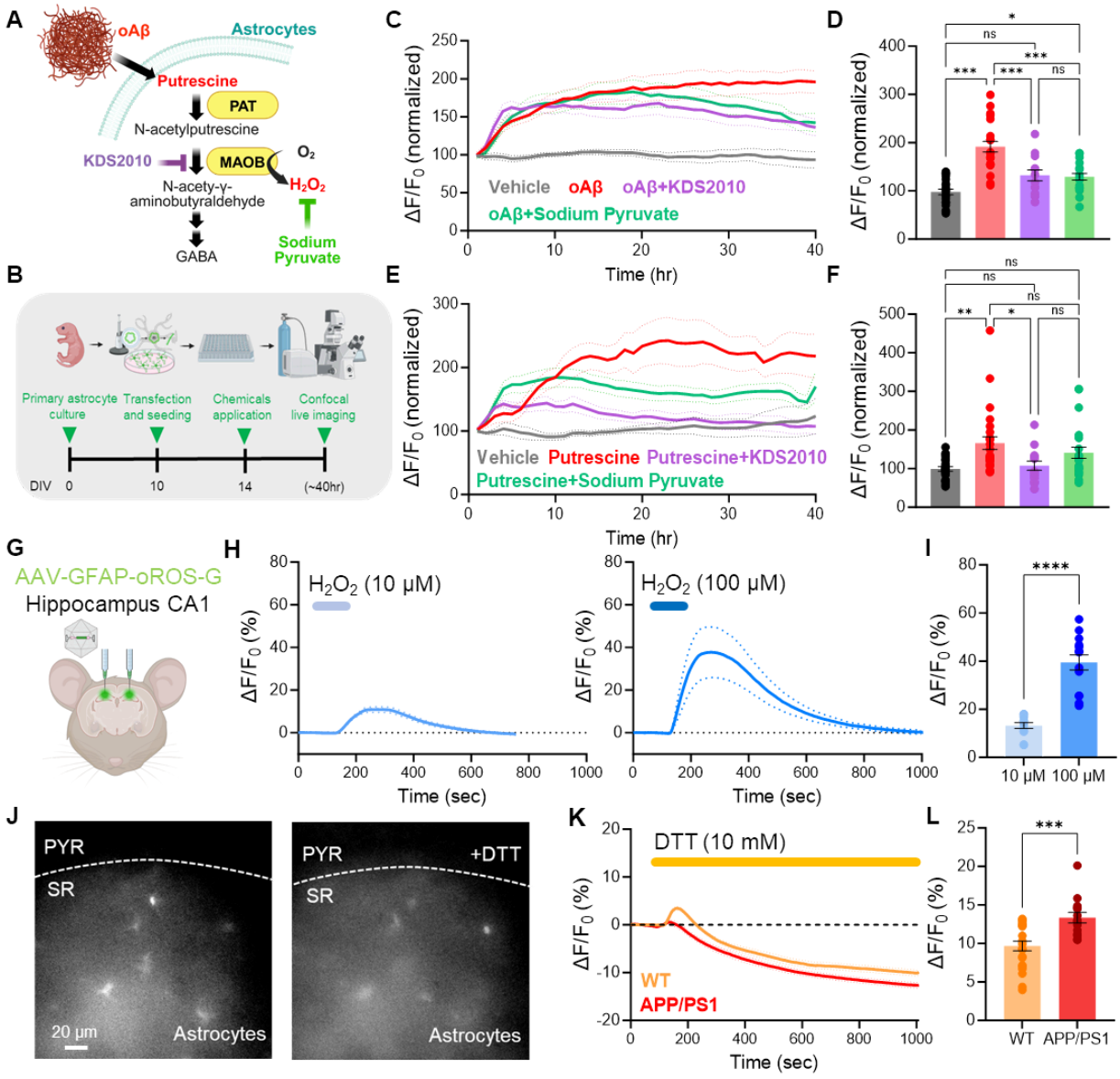

A Schematic illustration of the experimental timeline showing oROS-G transfected primary astrocytes seeded in a 96-well plate, administered with 5 μM oligomerized Amyloid beta (oAβ), 180 μM putrescine, 1 μM KDS2010 (selective and reversible MAOB inhibitor), and 1 mM sodium pyruvate (H_2O_2 scavenger) followed by 40-hour of confocal live imaging to monitor intracellular H_2O_2 and antioxidant effects. **B** Schematic diagram of the oAβ and putrescine induced H_2O_2 production. **C** 40-hour monitoring of oAβ-induced H_2O_2 production and antioxidant effects with KDS2010 and sodium pyruvate (Vehicle: n=22, oAβ: n=22, oAβ+Sodium Pyruvate: n=23, oAβ+KDS2010: n=13). **D** Summary bar graph representing fluorescence values normalized to the baseline, measured during the first hour. **E** Monitoring of putrescine-induced H_2O_2 production and antioxidant effects with KDS2010 and sodium pyruvate (Vehicle: n=24, Put.: n=25, Put.+Sodium Pyruvate: n=22,

Put.+KDS2010: n=14). **F** Summary bar graph representing fluorescence values normalized to the baseline. **G** Schematic illustration of the bilateral virus injection of experimental design. **H** Fluorescence response of oROS-G to 10 μM (n=13) or 100 μM H_2O_2 (n=14) in astrocytes of hippocampal tissue. **I** H_2O_2 dose-dependent summary bar graph. **J** Representative images captured with a CMOS camera illustrating the expression of oROS-G in astrocytes located in the stratum radiatum (SR) of the hippocampal CA1 region, in coronal brain slices ex vivo. oROS-G virus, driven by the GFAP promoter, is selectively expressed in astrocytes, with no expression in pyramidal neurons (PYR). **K** Fluorescence response of oROS-G to 10 mM (DTT) in astrocytes of hippocampal tissue (WT: n=22, APP/PS1 n=14). **L** Summary bar graph representing the difference between baseline fluorescence and saturation values after DTT administration. **Descriptive statistics:** Data are presented as mean ± SEM. **Inferential statistics:** D, F - One-way ANOVA with Tukey's multiple comparison test, I, J - Unpaired t-test, two-tailed *P < 0.05, **P < 0.01, ***P < 0.001.

Alzheimer's disease (AD) pathology[14,69]. In detail, upregulated monoamine oxidase B (MAOB) in reactive astrocytes produces H_2O_2 by breaking down oligomerized amyloid beta (oAβ)-metabolites, such as putrescine, leading to pathological H_2O_2 generation[70,71] **[Fig. 4A].** Therefore, we tested whether we could monitor aberrant endogenous H_2O_2 production in oROS-G transfected astrocytes treated with oAβ (5 μM) or putrescine (180 μM). Over a 40-hour continuous recording **[Fig. 4B]**, we observed a significant increase in oAβ-induced oROS-G fluorescence, indicating a notable rise in H_2O_2 **[Fig. 4C, D].** Conversely, the application of KDS2010 (1 μM), a selective MAOB inhibitor, and sodium pyruvate (1 mM), a potential H_2O_2 scavenger, showed a smaller increase in H_2O_2 levels. Additionally, incubation with putrescine, a pre-substrate of MAOB, also significantly increased oROS-G sensor fluorescence **[Fig. 4E, F]**. However, this H_2O_2 elevation was significantly reduced by KDS2010 and partially reduced by sodium pyruvate. Taken together, these results suggest that the oROS-G sensor in primary cultured astrocytes is a reliable tool for monitoring endogenous H_2O_2 production under AD-like conditions and evaluating the efficacy of potential H_2O_2-scavenging compounds.

Then, we asked whether we could measure the endogenous H_2O_2 levels in mouse brains. To test this idea, we bilaterally injected the AAV5-GFAP104-oROS-G virus into the CA1 hippocampus of APP/PS1 mice[71,72], a well-characterized Alzheimer's disease model, to express oROS-G sensor specifically in the astrocytes **[Fig. 4G].** Two weeks post-injection, we prepared brain slices and tested the H_2O_2 concentration-dependent functionality of the sensor. Again, to test the functionality of the sensor, we applied 10 and 100 μM H_2O_2 through bath application. We found an increase of 13.2 ± 1.2% and 39.5 ± 3.12% in

fluorescence with 10 and 100 μM H_2O_2, respectively **[Fig. 4H, I].** Like *in vitro*, the oROS-G sensor functions effectively in astrocytes *ex vivo*. Next, we examined the capability to measure elevated H_2O_2 levels in astrocytes of APP/PS1 mice. We hypothesized that treatment with DTT would unmask the portion activated by astrocytic H_2O_2. Following DTT (10 mM) administration, we observed a reduction in fluorescence below the baseline levels. Notably, we demonstrated that APP/PS1 mice exhibited a greater reduction compared to wild-type, suggesting a potential method for measuring endogenous H_2O_2 levels **[Fig. 4J-L].** Taken together, these results demonstrate that the oROS-G sensor functions effectively *ex vivo*, presenting a potential method for measuring endogenous H_2O_2 levels and investigating the antioxidant capacity of various molecules.

2.3.5. G-protein biased agonists elicit H_2O_2 generation in κ and μ opioid receptor-expressing neurons in the Ventral Tegmental Area *ex vivo* and *in vivo*.

We previously reported that peroxide generated by a NADPH oxidase (NOX) mechanism regulated opioid receptor signaling[6,16], which exemplifies intricate functional G-protein biased agonists' influence on arrestin-independent inactivation profile of μ and κ opioid receptors. Briefly, G-protein-biased opioid receptor activation triggers cJUN N-terminal kinase (JNK) phosphorylation. Phosphorylated JNK then activates peroxiredoxin 6 (PRDX6), producing superoxide (SO) from NOX. SO can quickly oxidize the Gαi protein complex to inactivate the opioid receptors. This event can be captured using H_2O_2 as a marker of opioid receptor activation because superoxide is readily transformed into H_2O_2 by superoxide dismutase[73–76] **[Fig. 5A]**. Given the robust responses of oROS-Gr, we sought to monitor transient H_2O_2 generation in the animal brain in response to G-protein-biased agonists.

As a proof of concept, we showed that morphine, a potent G-protein biased agonist of μ-opioid receptors (MOR), triggers transient peroxide generation in MOR-expressing neurons in the ventral tegmental area (VTA) of MOR-Cre transgenic mice, which is consistent with our previous findings. The oROS signals were measured using 2-photon microscopy on *ex vivo* live brain slices after viral delivery of the AAV1-DIO-oROS-Gr into the VTA of MOR-Cre transgenic mice. Expression of oROS-Gr in the VTA was verified with one-photon confocal

microscopy of post-mortem fixed brain slices **[Fig. 5B]**. The VTA in *ex vivo* brain slices showed an acute increase in sensor fluorescence during bath application of 1 μM morphine over 30 minutes of monitoring. This increase was blocked by the opioid receptor antagonist 1 μM Naloxone (Normalized ΔF/Fo to first 5 baseline frames, MOR: 3.35; ci = [1.94, 4.82], MOR+NLX: 0.63; ci = [0.42, 0.85]) **[Fig. 5C]**.

κ-opioid receptor (KOR) has emerged as a promising drug target for pain management with fewer side-effects[77]. We previously showed behavioral and pharmacological evidence on how the oxidative pressure of JNK-PRDX6-PLA2-NOX cascade from KOR results in acute analgesic tolerance, as shown in the warm water tail withdrawal assay[6]. Nalfurafine is a functionally selective G-protein biased κ-opioid agonist shown to have therapeutic potential as a non-dysphoric antipruritic analgesic[78]. Here, we explored the use of the oROS sensor to directly monitor acute H_2O_2 response to Nalfurafine *in vivo*, confirming activation of JNK-PRDX6-PLA2-NOX in KOR-positive neurons in the VTA. KOR-Cre transgenic mice were injected with AAV1-DIO-oROS-Gr, and the sensor fluorescence (ex:488/em:510) was monitored by fiber photometry in the VTA **[Fig. 5D]**. Intraperitoneal administration of 100 μg/kg Nalfurafine led to a transient increase of H_2O_2. Mice pre-treated 30 min prior to a 100 μg/kg Nalfurafine injection with a high dose of naloxone (10 mg/kg), sufficient to block KOR[79], showed no significant increase in fluorescence compared to mice only treated with Nalfurafine **[Fig. 5E]**. This confirms that the Nalfurafine-induced H_2O_2 signal in KOR-expressing neurons of VTA is opioid receptor-specific.

Figure 5 G-protein biased agonists elicit H_2O_2 generation in κ and μ opioid receptor-expressing neurons in the Ventral Tegmental Area *ex vivo* and *in vivo*.

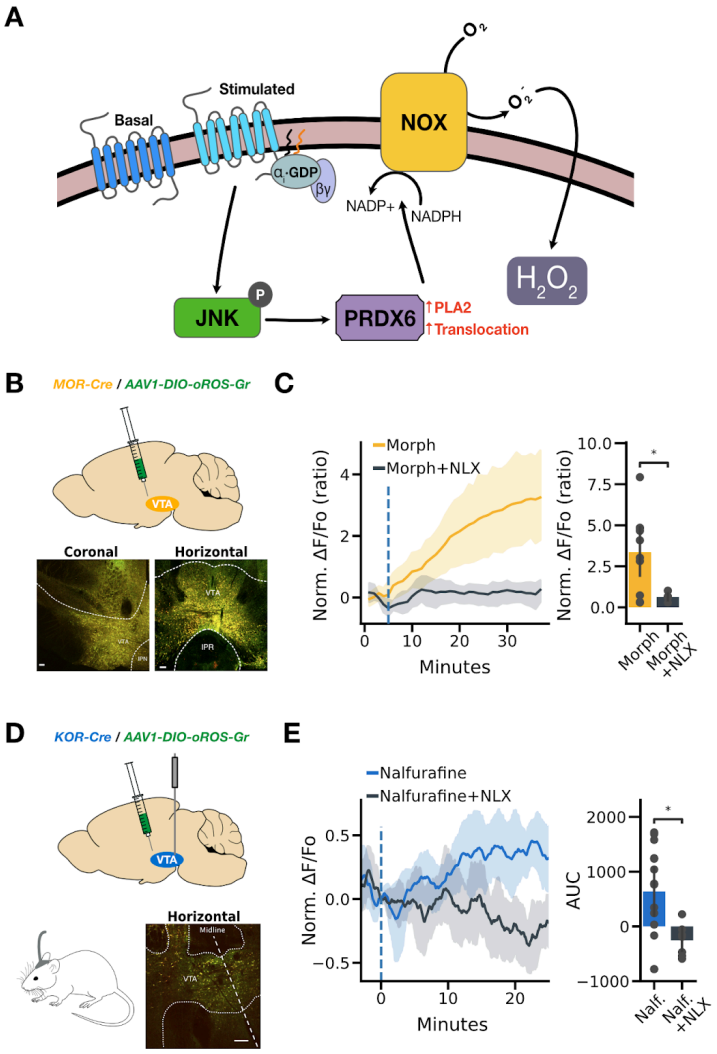

A Schematic illustration of the JNK/PRDX6/NOX pathway for opioid receptor-dependent generation of H_2O_2. **B** Targeted expression of oROS-Gr in μ opioid receptor (MOR) positive neurons of Ventral tegmental Area (VTA) was achieved by AAV1-DIO-oROSGr injection in VTA of *Oprm1*-Cre animals. Fluorescent images show histological validation of post-mortem slices via confocal microscopy. Scale bar = 100 μm **C** *Ex vivo* brain slice showing morphine-dependent H_2O_2 increase in MOR-positive neurons. (Morph: 1 μM Morphine, n=10 slices. Morph + NLX: 1 μM Morphine co-administered with 1 μM Naloxone, n=9 slices) ***left*** real-time trace of morphine-induced oROS-Gr signals detected in μOR positive neurons of VTA. Naloxone, a competitive mu-opioid receptor antagonist, effectively diminishes Morphine-induced oROS-Gr signals. ***right*** maximal fluorescence response for each condition. **D** Schematic description of fiber photometry experimental set-up with *Oprk1*-Cre transgenic mouse injected with AAV1-DIO-oROSGr in VTA. Bottom-right fluorescent image shows histological validation of post-mortem slices via confocal microscopy. Scale bar = 100 μm **E** *in vivo* fiber photometry of oROS-Gr (only ex:488/em:510) showed significant fluorescence increase in response to Nalfurafine (100 μg/kg), which is readily blocked by pre-treatment of Naloxone (10 mg/kg). (Nalfurafine: n=14, Nalfurafine + NLX: n=7 mice) ***left*** real-time trace of fiber signal from oROS-Gr detected in KOR (trans positive neurons of VTA. ***right*** Area under curve (AUC) integrated for each animal in each condition using the composite trapezoidal rule (trapz function in NumPy python package: version 1.26). **Descriptive statistics:** C, E - Error bars and bands represent the bootstrap confidence interval (95%) of the central tendency of values using the Seaborn (0.11.2) statistical plotting package. **Inferential statistics:** C,E - t-test independent samples. *P < 0.05, **P < 0.01, ***P < 0.001.

2.4. Discussion

Our refinement of the oROS sensor framework resulted in significant improvements in the kinetics and sensitivity compared to previous ecOxyR-based peroxide sensors. This optimization can largely be attributed to the relocation of the cpGFP insertion site to maintain the flexibility of the C199-C208 loop in ecOxyR and the incorporation of bulky residues adjacent to the cpGFP barrel opening. Interestingly, the diversity of OxyR variants in nature, each characterized by a conserved peroxide oxidation mechanism, opens avenues for exploring a range of sensor functionalities. Notably, OxyRs from different bacterial strains exhibit distinct reduction mechanisms; ecOxyR predominantly follows a Grx (glutaredoxin)-dependent reduction pathway, where Grx proteins facilitate the reduction of oxidized proteins[80]. In contrast, other variants like nmOxyR (*Neisseria meningitidis*), used by HyPer7[81], might employ a Trx (thioredoxin)-dependent reduction mechanism involving the Trx system known for mitigating cellular oxidative stress. This variation necessitates further exploration of these domains for sensors in mammalian systems, and they could serve as complementary tools for dissecting peroxide biology in various redox environments[81]. In addition, our study demonstrated the versatility of oROS sensors in a range of experimental applications. We successfully monitored H_2O_2 levels in astrocytes, both *in vitro* and *ex vivo*, shedding light on elevated oxidative stress in Alzheimer's models. Moreover, the ratiometric oROS-Gr sensor enabled us to observe the effects of glucose on cytoplasmic peroxide levels, which correlated with known patterns of mitochondrial oxidative stress. Additionally, our work highlights the oROS sensor's efficacy in detecting opioid-induced peroxide increase *in vivo*, further emphasizing the role of ROS in signaling mechanisms. In conclusion, oROS sensors, exemplified by oROS-G and oROS-Gr, offer real-time application across various model systems. They can monitor complex redox processes that are present in virtually all eukaryotic cells, with significant implications for unraveling the pathophysiology of oxidative stress in diseases.

2.5. Acknowledgments

J.D.L was supported by 1F31DA056121-01A1 and an ISCRM Fellowship. A.B was supported by the Brain Research Foundation, UW Royalty Research Fund, UW ISCRM IPA, NIGMS R01 GM139850-01, P30 DA048736, NIMH RF1MH130391, NINDS U01NS128537, NIDA R21DA051193 and the McKnight Foundation's Technologies in Neuroscience Award. K. E. was supported by T32AG066574. The research received additional support from the Lynn and Mike Garvey Imaging Core, the UW NAPE Center, and ISCRM Shared Equipment. We want to thank Dr. Randy Moon for his support. Also, this work was supported by the Institute for Basic Science, Center for Cognition and Sociality (IBS-R001-D2) to C.J.L. We are also grateful to the IBS virus facility for providing a virus packaging service for in vivo experiments.

Resource and Data Availability

Plasmid name: Addgene #

pC3.1_CMV_oROS-G: 216111, pC3.1_CMV_oROS-G_LF: 216112, pCAG_oROS-Gr: 216113, pCAG_oROS-Gr-LF: 216114, AAV2_CAG_oROS-G: 216115, AAV2_CAG_oROS-G_LF: 216116

Ethics Statement

All animal procedures performed at the University of Washington have been approved by the University of Washington's Animal Use Committee (protocol #4422-01) and follow the National Institute of Health and the Association for Assessment and Accreditation of Laboratory Animal Care International guidelines. Handling and animal care have been performed according to the Institutional Animal Care and Use Committee of the Institute for Basic Science.

2.6. Methods

2.6.1. Protein structure analysis

Protein structure analysis and plotting were performed using Chimera-X-1.2.1. Oxidized [PDB:1I6A] and reduced [PDB:1I69] crystal structures of ecOxyR were imported from the Protein Data Bank (PDB). Pairwise residue distance between reduced and oxidized ecOxyR structure was achieved by aligning both structures using a matchmaker algorithm that superimposes protein structures by creating a pairwise sequence alignment and then fitting the aligned residue pairs to derive pairwise residue distances.

2.6.2. Molecular Biology

oROS-G variants were cloned based on the pC1 plasmid backbone from pC1-HyPer-Red (Addgene ID: 48249). Primers for point mutations or fragment assembly required to generate the oROS-G screening variants were designed for In Vitro Assembly cloning (IVA) technique[82], Gibson Assembly (New England Biolabs; E2611L) or blunt-end amplification for KLD-based site-directed mutagenesis methods. Primers were ordered from Integrated DNA Technologies (IDT). All gene fragment amplifications were done using either Q5-polymerase (New England Biolabs; M0492L) or Superfi-II polymerase (Invitrogen; 12368010). Amplification of DNA fragments were verified with agarose gel electrophoresis. 30 minutes of DpnI enzyme treatment were done on every PCR product to remove the plasmid template from PCR samples. For IVA cloning circularization or assembly of the PCR products was achieved by transforming linear DNA products into competent *E.Coli* cells (DH5α or TOP10) and grown on agar plates that contain either ampicillin or kanamycin selection antibiotic (50 µg/mL). For gibson assembly and KLD cloning, circularized DNA was transformed as above. Upon colony formation, single colonies were picked and grown in 5mL cultures containing LB Broth (Fisher BioReagents; BP9723-2) and selection antibiotic (ampicillin/kanamycin; 50 µg/mL) overnight (37°C, 230 RPM). DNA was isolated using Machery Nagel DNA prep kits (Machery Nagel; 740490.250). Sanger sequencing (Genewiz; Seattle, WA) or Whole plasmid nanopore sequencing (Plasmidsarus; Eugene, OR) of the isolated plasmid DNA was used to confirm the presence of the intended mutation. Genes encoding the final variants were cloned into a

CAG-driven backbone, pCAG-Archon1-KGC-EGFP-ER2-WPRE (Addgene; #108423), using the methods above(New England Biolabs; E2621L). All subsequences were verified with Sanger sequencing (Genewiz; Seattle, WA) or Whole plasmid nanopore sequencing (Plasmidsarus; Eugene, OR)

2.6.3. Chemicals

H_2O_2 working solutions were freshly prepared before every experiment from H_2O_2 solution 30% (w/w) in H_2O (Sigma-Aldrich, H1009). Stock solution of Menadione (VENDOR, CAT) was prepared in 100% DMSO at 50mM. Stock solution of Cyclopiazonic Acid (Tocris, 1235) was prepared in 100% DMSO at 20mM. Chemicals specific to other method sections can be found in their respective sections.

2.6.4. Cell culture and transfection

Human Embryonic Kidney (HEK293; ATCC Ref: CRL-1573) cells were cultured in Dulbecco's Modified Eagle Medium + GlutaMAX (Gibco; 10569-010) supplemented with 10% fetal bovine serum (Biowest; S1620). When cultures reached 85% confluency, the cultures were seeded at 150,000/75,000 cells per well in 24/48-well plates, respectively. 24 hours after cell seeding, the cells were transfected using Lipofectamine3000 (Invitrogen; L3000015) at 1000/500 ng of DNA per well of a 24/48-well plate, according to the manufacturer's instructions.

2.6.5. Primary rat neuron isolation

Primary cortical neurons were prepared as previously described [47,48]. Briefly, 24-well tissue culture plates were coated with Matrigel (mixed 1:20 in cold-PBS, Corning; 356231) solution and incubated at 4°C overnight prior to use. Sterile dissection tools were used to isolate cortical brain tissue from P0 rat pups (male and female). Tissue was minced until 1 mm pieces remained, then lysed in equilibrated (37°C, 5% CO_2) enzyme (20 U/mL Papain (Worthington Biochemical Corp; LK003176) in 5mL of EBSS (Sigma; E3024)) solution for 30 minutes at 37°C, 5% CO_2 humidified incubator. Lysed cells were centrifuged at 200 xg for 5 minutes at room temperature, and the supernatant was removed before cells were resuspended in 3 mL of EBSS (Sigma; E3024). Cells were triturated 24x with a pulled Pasteur pipette in EBSS until homogenous. EBSS was added until the sample volume reached 10 mL prior to spinning at 0.7 rcf for 5 minutes at room temperature. Supernatant was

removed, and enzymatic dissociation was stopped by resuspending cells in 5 mL EBSS (Sigma; E3024) + final concentration of 10 mM HEPES Buffer (Fisher; BP299-100) + trypsin inhibitor soybean (1 mg/mL in EBSS at a final concentration of 0.2%; Sigma, T9253) + 60 µl of fetal bovine serum (Biowest; S1620) + 30 µl 100 U/mL DNase1 (Sigma;11284932001). Cells were washed 2x by spinning at 0.7 RCF for 5 minutes at room temperature and removing supernatant + resuspending in 10 mL of Neuronal Basal Media (Invitrogen; 10888022) supplemented with B27 (Invitrogen; 17504044) and glutamine (Invitrogen; 35050061) (NBA++). After final wash spin and supernatant removal, cells were resuspended in 10 mL of NBA++ prior to counting. Just before neurons were plated, matrigel was aspirated from the wells. Neurons were plated on the prepared culture plates at desired seeding density. Twenty-four hours after plating, 1 µM AraC (Sigma; C6645) was added to the NBA++ growth media to prevent the growth of glial cells. Plates were incubated at 37°C and 5% CO_2 and maintained by exchanging half of the media volume for each well with fresh, warmed Neuronal Basal Media (Invitrogen; 10888022) supplemented with B27 (Invitrogen; 17504044) and glutamine (Invitrogen; 35050061) every three days.

2.6.6. Human primary astrocytes, and stem cell derived cardiomyocytes and neurons

Astrocytes: Human primary cortical astrocytes were purchased from ScienCell Research Laboratories (Carlsbad, CA) and were stored, thawed and sub-cultured based on the manufacturer's protocol. Briefly, the astrocytes were cultured for 72 h in a base medium with an astrocyte growth supplement and fetal bovine serum provided by the same manufacturer. Cultures were maintained in a 37°C/5% CO_2 incubator throughout the culture period, and the astrocytes with low passage numbers (p0-p3) were used to guarantee consistent phenotype expression. When the culture became 70% confluent, the cells were dissociated with TrypLE (Thermo Fisher), followed by passaging on the PDL-coated 24 coverslips for oROS-G1 transfection. The transfected cells were then cultured for an additional 96 h before H_2O_2 treatment (10 µM, 100 µM) for recording the fluorescence response upon H_2O_2 stimulation.

Cardiomyocytes: Undifferentiated IMR90 (WiCell) hiPSCs were maintained on Matrigel (Corning) coated

tissue culture plates in mTeSR1 (Stemcell Technologies). Cardiomyocyte directed differentiation was performed using a modified small molecule Wnt-modulating protocol using Chiron 99021 and IWP-4 as previously described.[83,84]. Lactate enrichment was performed following differentiation to purify hiPSC-CMs[85].

Cortical neurons: Neurons were generated from the previously characterized wild type CV background human induced pluripotent stem cell line (Young et al. 2015). Neural progenitor cells (NPCs) from this cell line were differentiated from hiPSCs using dual-SMAD inhibition and NPCs were differentiated to neurons as previously described (Knupp et al., 2020; Shin et al., 2023). Briefly, for cortical neuron differentiation from NPCs, NPCs were expanded into 10 cm plates in Basal Neural Maintenance Media (BNMM) (1:1 DMEM/F12 (#11039047 Life Technologies) + glutamine media/neurobasal media (#21103049, GIBCO), 0.5% N2 supplement (# 17502-048; Thermo Fisher Scientific,) 1% B27 supplement (# 17504-044; Thermo Fisher Scientific), 0.5% GlutaMax (# 35050061; Thermo Fisher Scientific), 0.5% insulin-transferrin-selenium (#41400045; Thermo Fisher Scientific), 0.5% NEAA (# 11140050; Thermo Fisher Scientific), 0.2% β-mercaptoethanol (#21985023, Life Technologies) + 20 ng/mL Fibroblast Growth Factor (FGF) (R&D Systems, Minneapolis, MN). Once the NPCs reached 100% confluence, they were switched to Neural Differentiation Media (BNMM +0.2 mg/mL brain-derived neurotrophic factor (CC# 450–02; PeproTech) + 0.2 mg/mL glial-cell-derived neurotrophic factor (CC# 450–10; PeproTech) + 0.5 M dbcAMP (CC# D0260; Sigma Aldrich). Neural Differentiation Media was changed twice a week for 21 days at which point the differentiation is considered finished. Neurons were replated at a density of 500,000 cells/cm^2.

2.6.7. Imaging and data collection

Imaging experiments described in this study were performed as follows unless specifically noted. Epifluorescence imaging experiments were performed on a Leica DMI8 microscope (Semrock bandpass filter: GFP ex/em: FF01-474-27/FF01-520-35, RFP ex/em:FF01-578-21/FF01-600-37) controlled by MetaMorph Imaging software, using a sCMOS camera (Photometrics Prime95B) and 20x magnification lens (Leica HCX PL FLUOTAR L 20x/0.40 NA CORR) or 10× objective (Leica HCX PL FLUOTAR L 10x/0.32 NA). Confocal

imaging experiments were performed on a Leica SP8 confocal microscope from the Lynn and Mike Garvey Imaging Core at the Institute of Stem Cell and Regenerative Medicine. Cells were imaged in live cell imaging solution with 10 mM glucose (LCIS+, Gibco, A14291DJ) unless noted otherwise.

2.6.8. Analysis

2.6.8.1. Extraction and analysis of cellular fluorescence profiles

Extraction of cell fluorescence imaging data was done by FUSE, a custom cloud-based semi-automated time series fluorescence data analysis platform written in Python. First, the cell segmentation quality of the selected Cellpose[86] model was manually verified. For the segmentation of cells expressing cytosolic fluorescent indicators, model 'cyto' was selected as our base model. If the selected Cellpose model was low-performing, we further trained the Cellpose model using the Cellpose 2.0 human-in-the-loop system[87]. Using an "optimized" segmentation model, fluorescence time-series data is extracted for each region of interest. This allows for unbiased extraction of change in cellular fluorescence information for a complete set of experimental samples. When it is necessary, extracted fluorescence data is represented as ΔF/Fo(%) (eq. 1).

$$\{\backslash Delta\}\, F/\{F\}\_\{0\} = \backslash frac\{(F - \{F\}\_\{0\})\}\{\{F\}\_\{0\}\}\backslash times\, 100 \qquad (eq.\, 1)$$

2.6.8.2. Spatiotemporal diffusion mapping

The spatiotemporal diffusion profile was analyzed using a custom-developed Python script. To construct a time-series pixel-wise activation map, the intensity of each pixel at each time point was normalized by dividing by the maximum observed intensity, followed by background subtraction. This resulted in a ratio value for each pixel, which was then used to create a boolean map where pixels with a ratio above 50% were assigned a value of 1, and those below 50% were assigned a value of 0. For global diffusion speed analysis, we assumed that the diffusion direction was parallel to the x-axis, as observed. We calculated the ratio of the number of activated pixels (value of 1) to the number of pixels activated at any time point throughout the experiment, and applied min-max normalization to express this as a percentage, creating a diffusion distance map. Diffusion speed was estimated from the time points at which the number of activated pixels reached 10% of the total, without

interpolation. Finally, a chronological activation map was generated by determining the time at which 10% of pixels became activated in the previously mentioned activation map, which was smoothed using a Gaussian kernel (size 1.5) in FIJI software (version 2.14.0), to enhance spatial visualization.

2.6.9. Astrocyte study

Primary mouse astrocyte culture: Primary mouse cultured astrocytes were prepared from P1-P3 C57BL/6J mouse pups as previously described.[88] Briefly, 60-mm culture dishes were coated with 0.1 mg/ml poly-D-lysine (PDL, Sigma; P6407) solution prior to use. The hippocampal tissue was isolated, and dissociated into single cell suspension by trituration in Dulbecco's modified Eagle's medium supplemented with 4.5 g/L glucose, L-glutamine, sodium pyruvate (DMEM, Corning; 10-013-CV) + 10% heat-inactivated horse serum (Gibco; 26050-088) + 10% heat-inactivated fetal bovine serum (Dawin bio; A0100-010) + 1000 unit/ml penicillin-streptomycin (Gibco; 15140122). Dissociated cells were plated onto the PDL coated dishes. Cultures were maintained at 37°C in an incubator with a humidified atmosphere containing 5% CO_2. On the third day, cells were vigorously washed with repeated pipetting using medium to remove debris and other floating cell types.

On the 10th day of culture, cultured primary astrocytes were electrophoretically transfected with oROS-G plasmid with a voltage protocol (1200 V, 20 pulse width, 2 pulses) using the Microporator (Invitrogen Neon Transfection System; MPK5000S) and replated onto coverslip coated with PDL (Sigma; P6407) or µ-Plate 96 Well Black (ibid; 89626).

Imaging of cultured primary mouse astrocytes: On the 14th day of culture, the oROS-G transfected cultured primary astrocytes were transferred to a recording chamber which were mounted on an inverted Nikon Ti2-U microscope and continuously perfused with an external solution contained (in mM): 150 NaCl, 10 HEPES, 5.5 glucose, 3 KCl, 2MgCl2, 2 CaCl2, and pH adjusted to pH 7.3. Intensity images of 525 nm wavelength were taken at 485 nm excitation wavelengths using ORCA-Flash4.0 CMOS camera (Hamamatsu; C13440). Imaging workbench (INDEC Biosystem) and ImageJ (NIH) were utilized for image acquisition and ROI analysis of

cultured astrocytes. To examine H_2O_2-dose dependent responses of oROS-G transfected cultured astrocytes, concentrations of either 10 or 100 μM of H_2O_2 (Sigma; 88597) were introduced by bath application. The peak response of the sensor was normalized to its baseline (ΔF/Fo), which was measured 90 seconds before introducing H_2O_2. For confocal live-cell imaging and monitoring antioxidant drugs, confocal imaging was performed by using a Nikon A1R confocal microscope mounted onto a Nikon Eclipse Ti body with 20x objective lens. A Live-cell imaging chamber and incubation system were used for maintaining environmental conditions at 10% CO_2 and 37°C during 40-hour continuous recording. Images were acquired by using NIS-element AR (Nikon). For image analysis, NIS-element (Nikon) and ImageJ (NIH) were used.

Animals: All APP/PS1 mice were group-housed in a temperature- and humidity-controlled environment with a 12 h light/dark cycle and had free access to food and water.

Virus injection: The AAV5-GFAP104-oROS-G viral vector was cloned and AAV containing GFAP-104-oROS-G was packaged by the IBS virus facility (Daejeon, Korea). Mice were deeply anesthetized via vaporized 1% isoflurane and immobilized in a stereotaxic (RWD Life Science). Following an incision on the midline of the scalp, bilateral craniotomies were performed above the hippocampus CA1 (anterior/posterior, -2 mm; medial/lateral, ±1.6 mm; dorsal/ventral, -1.45 mm from the bregma) using a microdrill. The virus was bilaterally microinjected (0.1 μl/min for 10 min; total 0.8 μl) using a syringe pump (KD Scientific).

oROS-G imaging of GFAP-positive astrocytes in the brain slices: 2 weeks after viral injection into the hippocampus, animals were anesthetized with 1% isoflurane and then decapitated. The brains were submerged in chilled cutting solution that contained (in mM): 250 Sucrose, 26 NaHCO3, 10 D(+)-glucose, 4 $MgCl_2$, 0.1 $CaCl_2$, 2.5 KCl, 2 Sodium Pyruvate, 1.25 NaH_2PO_4, 0.5 ascorbic acid, and pH adjusted to pH 7.4. Coronal slices (300 μm thick) were prepared with a vibrating-knife microtome D.S.K LinearSlicer pro 7 (Dosaka EM Co. Ltd). For stabilization, brain slices were incubated at room temperature for at least 1 h before imaging. For imaging, the slices were transferred to a recording chamber which were mounted on an upright Zeiss Examiner D1 microscope and continuously perfused with an artificial cerebrospinal fluid (aCSF) solution that contained

(in mM): 130 NaCl, 24 $NaHCO_3$, 1.25 NaH_2PO_4, 3.5 KCl, 1.5 $MgCl_2$, 1.5 $CaCl_2$, D(+)-glucose, and pH adjusted to pH 7.4. All solutions were equilibrated with 95% O_2 and 5% CO_2. Imaging was acquired at 0.25 frame per second with 60X water-immersion objective lens, a ORCA-Flash4.0 CMOS camera (Hamamatsu; C13440), and a LED (CoolLED) filtered with 485-nm fluorescence was applied. Imaging workbench (INDEC Biosystem) and ImageJ (NIH) were utilized for image acquisition and ROI analysis. To examine H_2O_2-dose dependent responses of sensor-expressing astrocytes, concentrations of either 10 or 100 μM of H_2O_2 were introduced by bath application. The peak response of the sensor was normalized to its baseline (ΔF/Fo), wich was measured 90 seconds before introducing H_2O_2. To measure endogenous H_2O_2 in astrocytes of APP/PS1 mice and their littermates, we used 10 mM DTT (Thermo; R0861). This method reduced the oROS-G sensor bound to H_2O_2, resulting in fluorescence below the baseline levels. These reduced fluorescence responses were normalized to its baseline (ΔF/Fo), suggesting the basal endogenous H_2O_2 levels.

2.6.10. Generation of stable oROS-Gr expressing HEK293 cells

HEK293 cells in a T75 flask were transfected (using lipofection, as described above) with oROS-Gr-P2A-Puromycin plasmid. 3 Days after the transfection, cells were passaged to 2 T75 flasks. 2 Days after, puromycin-based selection was performed for a week using complete DMEM media (as previously described) supplemented with puromycin (1 μg/mL). Cells after selection were expanded for 3 passages. Enrichment of cell populations with robust oROS-Gr expression was achieved with BD FACSAria II Cell Sorter at Flow and Imaging Core Lab of University of Washington South Lake Union Campus.

2.6.11. Glucose experiment and Seahorse Assay

oROS-Gr stable cells cultured in complete DMEM with 10 mM glucose were plated at 75,000/well in 24-well plates. oROS-Gr stable cells were plated at 75,000/well in 24-well plates. 1 day post seeding, FBS in the DMEM media was brought down to 2% from 10%. 2 day post seeding cells were in serum-free DMEM with various levels of glucose. Mannose was supplemented as needed to keep osmotic pressure of each media consistent (final total sugar content: 25 mM). oROS-Gr ratio (GFP/RFP) were imaged in LCIS media with

varying glucose and mannose level. For Seahorse assay, oROS-Gr stable cells mentioned above were plated in a Matrigel-coated 96 well Seahorse plate at a density of 2×10^5 cells/well for an equivalent procedure as above. The MitoStress protocol in the Seahorse XF96 Flux Analyzer (Agilent Technologies, Santa Clara, CA, USA) was performed two weeks later. An hour before the assay, the culture media was replaced with media (Agilent Seahorse XF base medium, 103334-100 Agilent Technologies, Santa Clara, CA, USA) supplemented with 25 mM glucose and 1 mM Sodium pyruvate (11360070 Gibco/Thermo Scientific, Waltham, MA, USA). Substrates and select inhibitors of the different complexes were added during the measurement to achieve final concentrations of oligomycin (2.5 μM), FCCP (1 μM), rotenone (2.5 μM) and antimycin (2.5 μM). The oxygen consumption rate (OCR) values were then normalized with readings from Hoechst staining (HO33342 Sigma-Aldrich, St. Louis, MO, USA), which corresponded to the number of cells in the well.

2.6.12. Opioid receptor study

AAV: An adenovirus associated double floxed inverted (AAV1-DIO) virus was generated containing the oROS-Gr by cloning oROS-Gr into pAAV1-Ef1a-DIO using Nhe1 and Asc1 restriction sites. AAV1 were prepared by the NAPE Molecular Genetics Resources Core as described previously (Gore, et al, 2013). HEK293T cells were transfected with 25 μg AAV1 vector plasmid and 50 μg packaging vector (pDG1) per 15 cm plate. Two days after transfection, cells were harvested and subjected to three freeze–thaw cycles. The supernatant was transferred to a Beckman tube containing a 40% sucrose cushion and spun at 27,000 rpm overnight at 4°C. Pellets were resuspended in CsCl at a density of 1.37 g/ml and spun at 65000 rpm 4 hours at 4°C. 1 ml CsCl fractions were run on an agarose gel, and genome-containing fractions were selected and spun at 50000 rpm overnight at 4°C. The 1 ml fractions were collected again, and genome containing fractions were dialyzed overnight. The filtered solution was transferred to a Beckman tube containing a 40% sucrose cushion and spun at 27,000 rpm overnight at 4°C. The pellet (containing purified AAV) was resuspended in 150 μl 1× HBSS. Virus was aliquoted and stored at -80 ° C until use.

Animals and surgeries: Test naive C57BL/6 male mice were ear punched at least 21 days after birth and genotyped using Transnetyx genotyping services. PCR screening was performed for the presence of Cre recombinase. For brain slice studies, mice between 5-7 weeks of age were injected with 0.5 µL AAV1-Efla-FLEX-oROS-mCherry (CITE) construct containing oROS-Gr into a *Oprm1*-CRE positive mouse bilaterally into the VTA using coordinates: ML: +/- 0.5, AP: -3.28, DN: -4.5 zeroed at bregma. Isoflurane was used for anesthesia and carprofen for pain relief. Mice were mounted on a stereotaxic alignment system and injections were made using a Hamilton 2.0 µL model 7002 KH syringe. Similarly, for fiber photometry experiments, mice were injected with 0.5 µL AAV1-Efla-FLEX-oROS-mCherry unilaterally at a 15-degree angle, using the coordinates ML: -1.71, AP: -3.28, DN: -4.67 then implanted with a 400/430 µm diameter Mono fiberoptic cannula from Doric Lenses.

2-photon imaging of µ-opioid receptor expressing neurons in VTA: Two-four weeks after viral injection, the brain was dissected and 200 µm horizontal slices were prepared using a vibratome. Slices were incubated in NMDG (92 mM NMDG, 2.5 mM KCl, 1.25 mM NaH_2PO_4, 30 mM $NaHCO_3$, 20mM HEPES, 25 mM Glucose, 2 mM Thiourea, 5 mM Na-ascorbate, 3 mM Na-pyruvate, pH to 7.4, 0.5 mM $CaCl•4H_2O$, 10 mM $MgSO_4•7H_2O$). Recordings were made in a HEPES solution (92 mM NaCl, 2.5 mM KCl, 1.25 mM NaH_2PO_4, 30 mM $NaHCO_3$, 20 mM HEPES, 25 mM Glucose, 2 mM Thiourea, 5 mM Na-Ascorbate, 3 mM Na-Pyruvate). Image collection was done using a Bruker Investigator 2-photon microscope, software Prairie View 5.5, simultaneously collecting both the mCherry (1040 nm fixed) and GFP (920 nm tunable) signals with a Nikon 16X water immersion objective, as well as a z-stack spanning 60 µm across an hour time course. Baseline recordings were made in ACSF (124 mM NaCl, 3 mM KCl, 2 mM $MgSO_4$, 1.25 mM NaH_2PO_4, 2.5 mM $CaCl_2$, 26 mM $NaHCO_3$, 10 mM Glucose) at 32ºC, before treatment. For confocal images, animals were perfused intracardially with phosphate-buffered saline (PBS) and 10% formalin. Brains were stored in 10% formalin for up to 24 hours then switched to a 20% sucrose solution at 4ºC until sectioning. Coronal slices of the VTA were

collected at 40 μm each and mounted using VECTASHIELD HardSet mounting Medium with DAPI. Confocal images were taken with the Leica SP8x Confocal microscope located in the Keck Center at UW.

Fiber photometry of kappa-opioid expressing neurons in the VTA: A real-time signal processor (RZ5P; Tucker-Davis Technologies) connected to Synapse Software (Fiber Photometry) to set frequency of light stimulation and to record input from photodetectors. The RZ5P was connected to a light emitting diode (LED) driver (Doric Lenses) that controlled the power of a 465 nm and 560 nm Doric LED. A low autofluorescence patch cord (400/430) was attached to the LED, to a fluorescent MiniCube (Doric Lenses) with dichroic mirrors. Connected optical patch cords to the MiniCube with pigtailed rotary joining (FRJ; Doric Lenses) allowed free animal movement during data collection. Patch Cords were bleached with light prior to photometry sessions to minimize autofluorescence. Power of the LED at the fiber tip was set to ~30 μW and was tested prior to the start of each session. Signals were collected at a sampling frequency of 1017 Hz. Each of the sessions was downsampled by a factor of 100 and normalized to a 15-minute baseline period in the beginning of the recording. Data were then smoothed using a moving average filter (100 sec window) to remove high frequency noise and detrended to remove linear drift. The isosbestic channel (405 nm) was fitted to the 470 nm channel using a least-squares method and subtracted to remove motion artifacts. Each session started with a 15 min baseline recording period prior to pharmacological experiments to calculate fluorescent change from baseline (ΔF/Fo; Change in fluorescence from baseline fluorescence/baseline fluorescence).

2.7. Appendix (Supplementary Information)

Supplementary Figure 1 Structure-guided engineering of oROS-G.

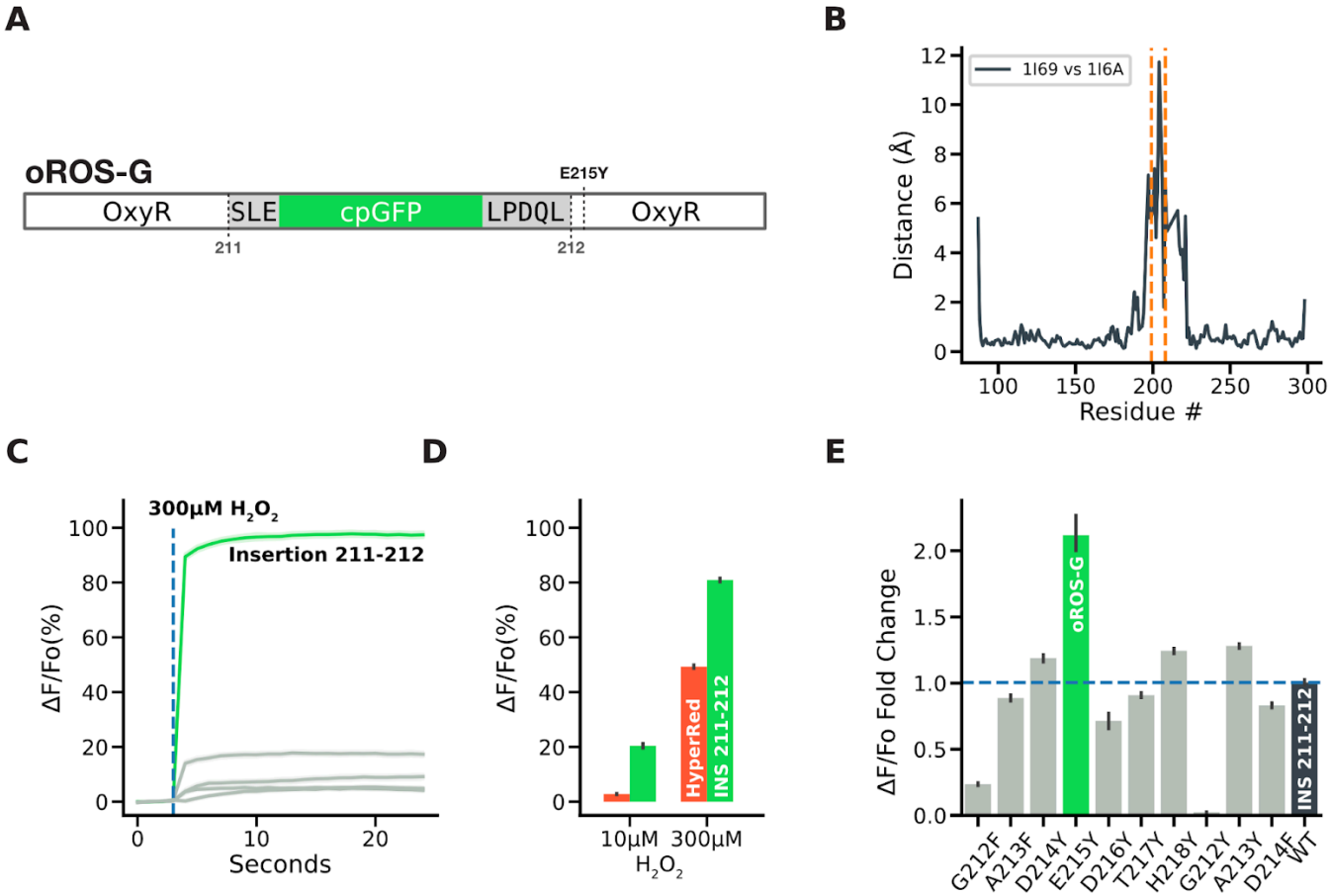

A Amino acid sequence design of oROS-G sequence design **B** Reduced [PDB:1I69] and oxidized [PDB:1I6A] form of OxyR was superimposed and calculated to residue-to-residue distance to estimate the degree of conformational change. Gray lines indicate C199 and C208. **C-E** Screening of oROG-G sensor variants. All the sensor variants were expressed and screened on HEK293 cells (n>100 cells per condition/variant). **C** fluorescence change (ΔF/Fo) in response to extracellular H_2O_2 (300 μM) stimulation on variants with cpGFP insertion to newly identified oROS insertion region. Insertion 211-212, a variant with exceptional response kinetic and dynamic range was identified. **D** Maximum fluorescence change (ΔF/Fo) of Insertion 211-212 and HyPerRed in response to high (300 μM) and low (10 μM) extracellular H_2O_2. **E** Maximum fluorescence change (ΔF/Fo) of site-directed mutagenesis variants predicted to reduce water access for cpGFP. Mutation E215Y on Insertion 211-212 variant led to engineering oROS-G. **Descriptive statistics:** Error bars and bands represent the bootstrap confidence interval (95%) of the central tendency of values using the Seaborn (0.11.2) statistical plotting package. Cells-of-interest were collected from 3 biological replicates unless noted otherwise.

Supplementary Figure 2 oROS-G response is C199-C208 mechanism specific.

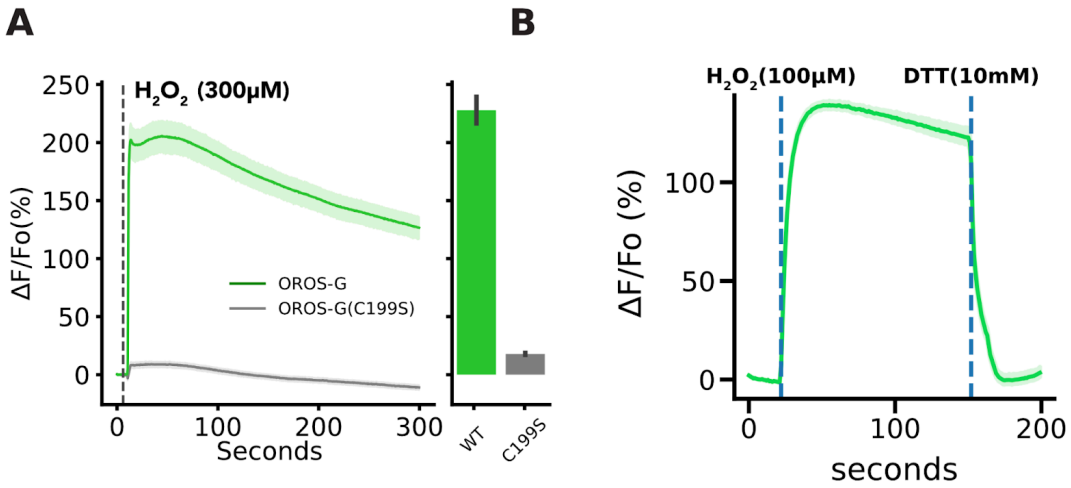

A HEK293s expressing oROS-G and oROS-G1-C199S (loss-of-function) were stimulated with 300 μM H_2O_2. The barplot represents the mean of the maximum fluorescent responses. **B** Induced reduction of oROS-G. HEK293s expressing oROS-G were first stimulated with 100 μM H_2O_2 and then 10 mM Dithiothreitol (DTT), a reducing agent, shortly after (n>100 cells). **Descriptive statistics:** Error bars and bands represent the bootstrap confidence interval (95%) of the central tendency of values using the Seaborn (0.11.2) statistical plotting package.

Supplementary Figure 3 Fluorescence spectra of oROS-G in HEK293 cells.

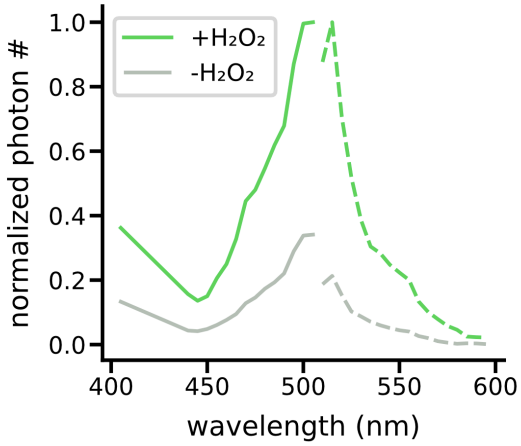

Excitation (solid line) and Emission (dotted line) spectra of oROS-G expressed in HEK293 acquired with Leica Stellaris confocal microscope. +H_2O_2: exogenous 300 μM H_2O_2 stimulation, -H_2O_2: resting state in HEK293 cells.

Supplementary Figure 4 On-kinetics of oROS-G and HyPerRed in HEK293 cells.

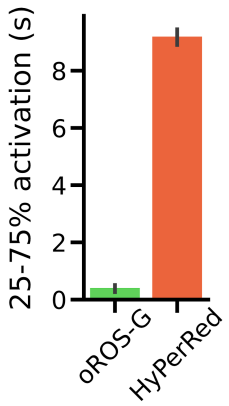

Derived from Fig 1 C,D. On-kinetic analysis of oROS-G (n=1128 cells) and HyPerRed (n=1141 cells). 300 µM peroxide-induced saturation of both sensors with normalized ΔF/Fo. Vertical dotted lines represent 75% sensor activation, labeled with 25-75% activation completion time. 100% indicates full sensor saturation. (n>100 cells per condition/variant). **Descriptive statistics:** Error bars and bands represent the bootstrap confidence interval (95%) of the central tendency of values using the Seaborn (0.11.2) statistical plotting package.

Supplementary Figure 5 Reduction kinetics of oROS-G and HyPer7 in HEK293 cells.

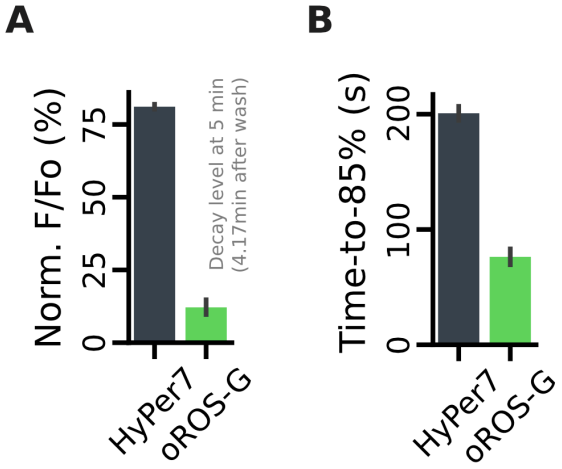

Derived *from Fig. 1G:* **A** Normalized ΔF/Fo (%) level of oROS-G (n=137, cells) and HyPer7 (n=222, cells) at 4.17 minutes after wash-induced reduction. The smaller value indicates a more efficient reduction. **B** Time measured for reduction to 85% fluorescence from the sensor saturation. **Descriptive statistics:** Error bars and bands represent the bootstrap confidence interval (95%) of the central tendency of values using the Seaborn (0.11.2) statistical plotting package.

Supplementary Figure 6 Visualizing extracellular and intracellular diffusion H_2O_2 using oROS-G.

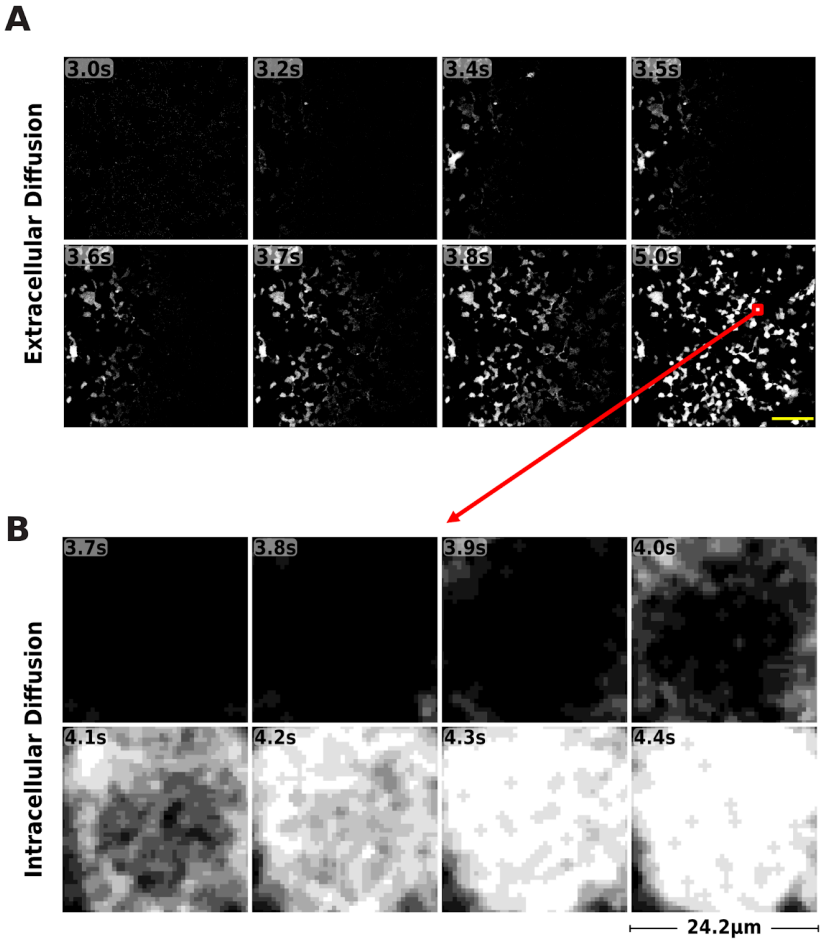

A Representative time-series frames of pixel-wise activation map derived from **Fig 2B** (before convolution)**.** For the transformation, pixel values are gated to be "Black (0)" at 0~50% sensor activation and White (1) at 50%~100% sensor activation to enhance visualization. Scale bar = 150 µm **B** Zoomed-in representative time-series frames showing intracellular diffusion of peroxide.

Supplementary Figure 7

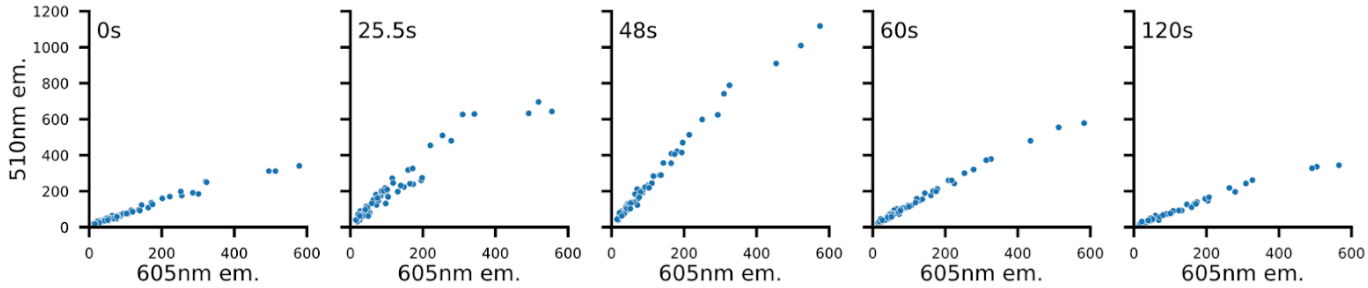

Distribution of 510 nm and 605 nm emission intensity of each ROI at selected temporal snapshots from Figure 3C.

Supplementary Figure 8

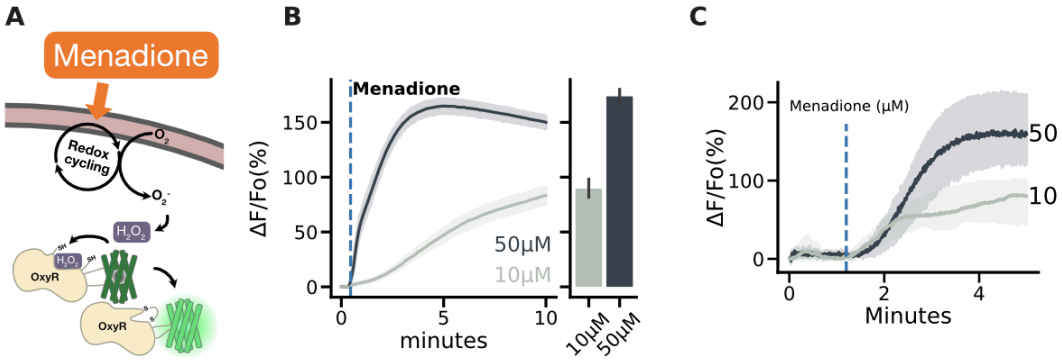

A Schematic illustration of cellular redox cycling dependent H_2O_2 producing mechanism of Menadione. **B** Fluorescence response of oROS-G to high (50 µM) or low (10 µM) menadione (n>100 cells per condition). The sensors were expressed in HEK293. The barplot represents the mean of the maximum fluorescent response of cells. **C** Dose-dependent fluorescence response of oROS-G to high (50 µM) or low (10 µM) menadione expressed in human primary astrocytes. (n=3 cells per condition) Fluorescence response of oROS-G to high (50 µM) or low (10 µM) menadione (n>100 cells per condition). The sensors were expressed in HEK293. The barplot represents the mean of the maximum fluorescent response of cells.

Supplementary Figure 9

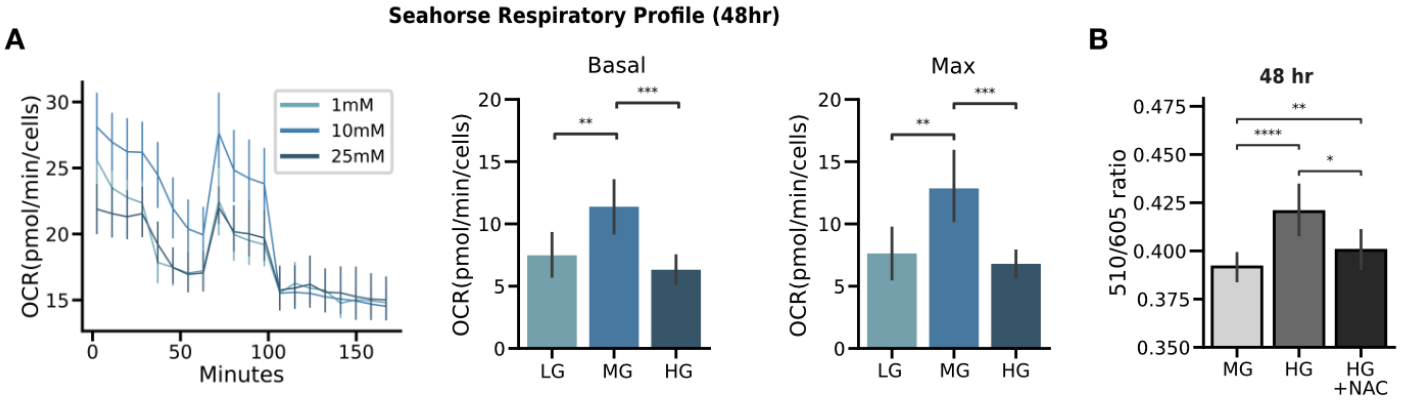

A Seahorse assay results after incubating oROS-Gr stable HEK293 cells in various glucose conditions (n=24 wells per condition). LG and HG conditions, which showed higher oxidation, also exhibited respiratory depression. **middle** Basal respiratory level calculated from Seahorse assay, units in Oxygen Consumption Rate (pMol/min, n=24 wells per condition) **right** Max respiratory capacity calculated from Seahorse assay, units in Oxygen Consumption Rate (pmol/min, n=24 wells per condition). **B** Observation of glucose-level dependent basal oxidation level of oROS-Gr (510/605 ratio) in stably expressing HEK293 cells. The cells were incubated in MG (Medium glucose, 10mM), HG (high glucose, 25mM), or HG+NAC (negative control, HG+1 mM of NAC) for 48 hours after they were serum-deprived overnight. NAC diminishes the oxidation level of HG (n>100 cells per condition). **Descriptive statistics:** Error bars and bands represent the bootstrap confidence interval (95%) of the central tendency of values using the Seaborn (0.11.2) statistical plotting package. Cells-of-interest were collected from 3 biological replicates unless noted otherwise. **Inferential statistics:** F - t-test independent samples. *P < 0.05, **P < 0.01, ***P < 0.001.

Supplementary Figure 10

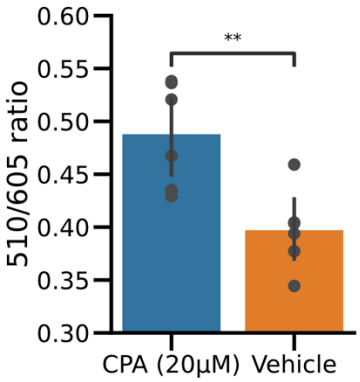

Resting oROS-Gr ratio expressed in hiPSC-derived cardiomyocytes incubated in SERCA blocker cyclopiazonic acid (CPA) for 2 hours. (CPA: 0.49 (n = 6); ci = [0.45, 0.52], Vehicle: 0.4 (n = 6); ci = [0.37, 0.43]) **Descriptive Statistics:** Error bars and bands represent the bootstrap confidence interval (95%) of the central tendency of values. **Inferential Statistics:** t-test independent samples. *P < 0.05, **P < 0.01, ***P < 0.001.

Supplementary Figure 11 Monitoring the effects of antioxidants on intracellular peroxide levels in Alzheimer's model.

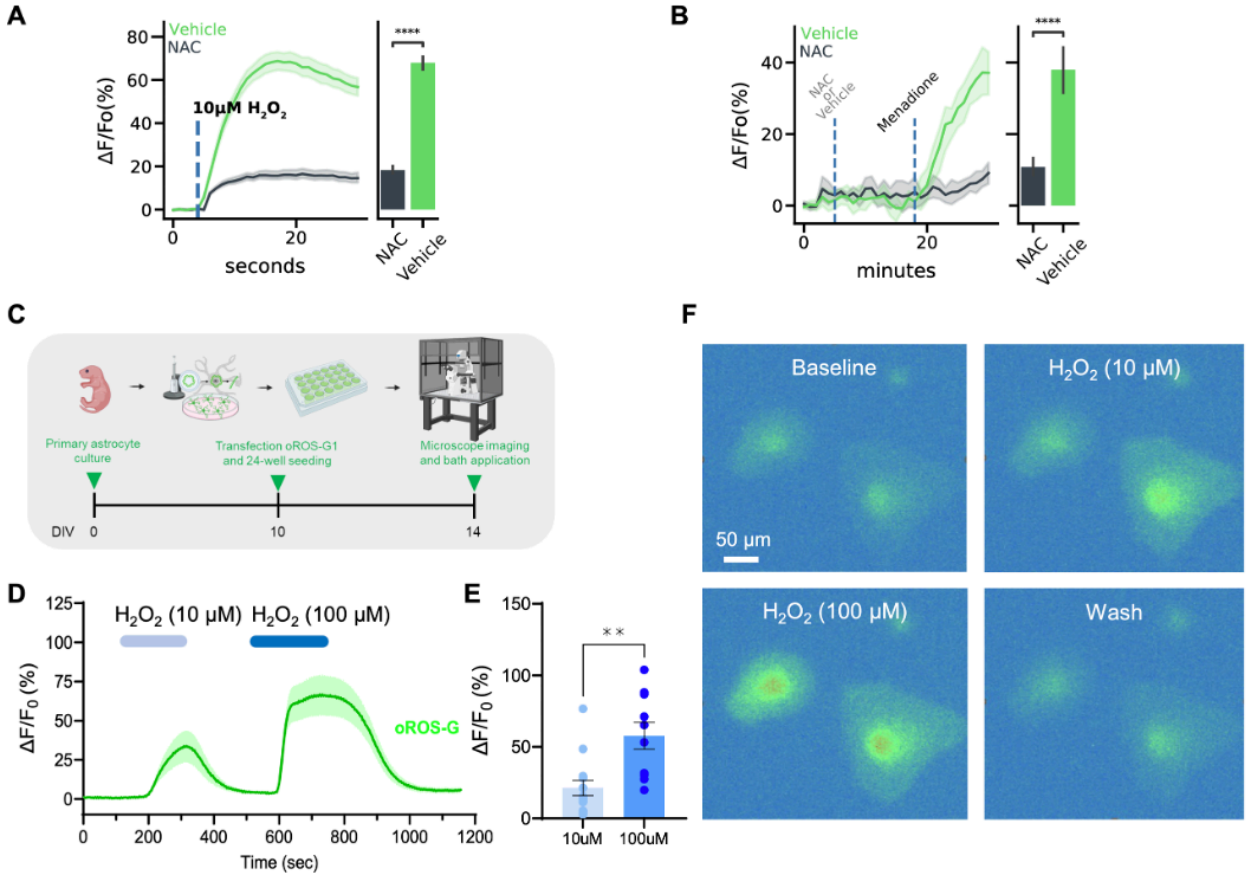

A-B oROS-G's response in the presence of the antioxidative agent, N-acetyl-cysteine (NAC). **A** HEK293 cells expressing oROS-G1 were stimulated with 10 mM NAC and 10 μM Menadione sequentially and imaged for 30 minutes. Barplot represents the mean of the maximum fluorescent response of ROI. **B** HEK293 expressing oROS-G were preincubated with 1 mM NAC for 1 hour, and then the fluorescence response to 10 μM H_2O_2 was monitored. **C** oROS-G expressed in primary astrocytes exposed in sequential H_2O_2 exposure (10 μM and 100 μM extracellular) over 20 minutes. **C** Schematic illustration of the experimental timeline showing oROS-G transfection in primary cultured astrocytes seeded on PDL-coated coverslip in a 24-well plate, followed by subsequent experimental procedures. **D** Representative fluorescence images showing oROS-G expression in astrocytes: baseline (control), bath application with 10 μM and 100 μM H_2O_2, and HEPES buffer (recovery). The sensor was expressed in cultured astrocytes. **E** Fluorescence response of oROS-G to 10 μM or 100 μM H_2O_2 in cultured astrocytes. **F** H_2O_2 dose-dependent summary bar graph. **Descriptive statistics:** Error bars and bands represent the bootstrap confidence interval (95%) of the central tendency of values using the Seaborn (0.11.2). **Inferential statistics:** A, B, D - t-test independent samples. *P < 0.05, **P < 0.01, ***P < 0.001, ****P < 0.0001.

Chapter 3. Spatiotemporally resolved H_2O_2 monitoring and multi parametric imaging applications.

Lee JD, Nguyen A, Gibbs CE, Jin ZR, Wang Y, Moghadasi A, Wait SJ, Choi H, Evitts KM, Asencio A, Bremner SB, Zuniga S, Chavan V, Pranoto IKA, Williams A, Smith N, Moussavi-Harami F, Regnier M, Baker D, Young JE, Mack D, Nance E, Boyle PM, Berndt A.

https://doi.org/10.21203/rs.3.rs-3974015/v1 (Under consideration: Nature Chemical Biology)

3.1. Abstract

Multiparametric monitoring of H_2O_2 dynamics, in conjunction with key biological interactants, is critical for elucidating the physiological outcome of cellular redox regulation. Here, we present a far-red chemigenetic H_2O_2 Indicator, oROS-HT_{635}. oROS-HT_{635} allows fast and sensitive H_2O_2 monitoring while overcoming critical drawbacks of existing red fluorescent H_2O_2 indicators, including oxygen and high pH sensitivity, photo-artifacts, and intracellular aggregation. oROS-HT_{635} enables real-time dual-color imaging in combination with blue-green fluorescent sensors for the interactants, allowing versatile optogenetic dissection of redox biology. Here, we demonstrated efficient subcellular targeting of oROS-HT_{635} and demonstrated its utility on spatially resolved H_2O_2 imaging in oxidative stress models, specifically in proximity to plasma membranes. Lastly, we used oROS-HT_{635} with other green fluorescence reporters to capture acute and real-time landscape of H_2O_2, intracellular redox potential, and Ca^{2+} levels in response to auranofin, an inhibitor of antioxidative agents, via polychromatic, dual-color imaging.

3.2. Introduction

Oxidative stress is often a key component of many disease progressions. Tremendous efforts have been made to develop therapeutic approaches to target the excessive presence of oxidants and their source. However, the unsatisfying results of antioxidative therapy call for a more nuanced understanding of cellular oxidants,

antioxidative defense networks, and their effect on the cellular system with precision and specificity to improve rationales on antioxidative therapeutics[59].

H_2O_2 is a major oxidant in redox biology that can also act as a pleiotropic secondary messenger in various cellular signaling processes[3,33–36]. Its precursor superoxide is a natural byproduct of aerobic metabolism, which rapidly gets converted to H_2O_2 naturally or by superoxide dismutase (SOD)[76]. The level of intracellular H_2O_2 is tightly regulated by peroxide-reducing mechanisms[89,90]. Although peroxide is considered less reactive than other cellular oxidative agents, its excessive accumulation is often observed in pathology, with growing evidence of its causal role in the progression of diseases[14,91,92]. The engineering of genetically encoded H_2O_2 indicators (GEHI, e.g. OxyR-based sensors[26,28,41], peroxidase-based sensors[22,40,93]) has been a significant step towards understanding the role of peroxide in redox biology by enabling real-time monitoring of peroxide dynamics in a wide array of biological hosts[18]. One advantage of GEHIs over redox-sensitive fluorescence dyes is their spatiotemporal flexibility: they can be expressed for extended periods of time and targeted to specific cell types or various cellular compartments when coupled with proper expression systems (e.g. promoters and trafficking/export tags). Specifically, red-fluorescent GEHIs facilitate multiparametric analysis of peroxide dynamics along with other key biomolecules or processes considering a large number of green fluorescent sensors for biological molecules and processes (e.g. Ca^{2+}, pH, voltage, redox potential, etc.)[94,95]. Nevertheless, current red-shifted GEHIs exhibit slow kinetics, a bottleneck for real-time peroxide imaging. Most importantly, blue-light-induced photochromic artifacts commonly associated with red fluorescent protein (FP)-based sensors make unobstructed polychromatic analysis alongside green fluorescent sensors prone to false signals[96]. Lastly, aggregation tendency and low brightness are also observed among red fluorescent proteins[97], thus diminishing the utility of existing red GEHIs.

In this study, we coupled the bacterial OxyR peroxide sensor with a rhodamine-HaloTag-based chemigenetic reporter system to create a first in its class far-red indicator for H_2O_2: oROS-HT_{635} (optogenetic hydRogen perOxide Sensor with HaloTag with JF635). We developed a rational engineering strategy based on

structural information derived from experimentally resolved structures and computational models (ColabFold)[98]. oROS-HT_{635} has excitation and emission wavelengths of 640 nm and 650 nm. We validated it in various biological host systems, including stem cell-derived cardiomyocytes *in vitro* and primary neurons *ex vivo*. Moreover, we found that the fast oROS-HT_{635} kinetics allows the observation of intracellular diffusion of H_2O_2. Also, oROS-HT_{635} is free from photochromic artifacts, allowing polychromatic analysis of contextual H_2O_2 dynamics. As a proof-of-concept, we showed the acute effect of the anti-inflammatory agent auranofin on peroxide levels together with changes in the cellular redox potential in HEK293 cells or Ca^{2+} levels in human-induced pluripotent stem cell-derived cardiomyocytes (hiPSC-CMs). These experiments establish more accurate spatial and temporal correlations between different physiological phenomena. Lastly, we used previously described chemogenetic and optogenetic methods of induced site-specific H_2O_2 generation to visualize the diffusion of H_2O_2 from mitochondria and outer plasma membranes toward the inner plasma membrane and to neighboring cells.

3.3. Results

3.3.1. Structure-guided engineering of oROS-HT_{635}: a bright far-red optogenetic sensor for H_2O_2.

OxyR is a bacterial transcription activator with high specificity and sensitivity toward H_2O_2 with low peroxidative capability (i.e. the protein exhibits high sensitivity towards peroxide with limited catalytic activity)[99]. Existing red-shifted GEHI, such as HyPerRed[26] and SHIRMP[41] utilize ecOxyR-LBD (ligand binding domain of OxyR from *Escherichia coli*), as their sensing domain. However, both red GEHIs show slower kinetics (10s to 100s seconds for full activation under saturation and half an hour for reduction) than the innate kinetics and sensitivity reported for ecOxyR itself[42,80,100]. Specifically, the rate of ecOxyR oxidation is at a sub-second scale, and its reduction takes 5~10 minutes. We hypothesized that the insertion of the fluorescence reporter domain may have slowed the activation and deactivation of ecOxyR in the currently available red-shifted GEHI sensors. Our engineering strategy aimed to maintain the flexibility of the protein loop that drives the conformational change in the sensing domain (i.e. ecOxyR-LBD) in the derived sensors, as we

previously validated in the development of a GFP-based oROS-G sensor[101]. Specifically, ecOxyR contains a hydrophobic pocket that forms the active center for peroxide interactions. Upon binding, peroxide forms a hydrogen bonding network with adjacent residues, bringing residues C199 and C208 into close proximity to form a disulfide bridge. By analyzing the B-factors of ecOxyR-LBD structures, we observed an evident high flexibility peak in the 199-208 region **[Fig. 1a].** We reasoned that preserving this flexibility is necessary for efficient OxyR activation by peroxide[43,99,102]. Thus, inserting a bulky fluorescent reporter between C199 and C208, as in HyPerRed, may be responsible for the slowed OxyR activation, and we explored alternatives outside this region **[Fig. 1b]**. Furthermore, red fluorescent proteins pose challenges for versatile use involving optical polychromatic analysis or neuron expression. For example, cpmApple, used in HyPerRed, exhibits a false positive photochromic artifact induced by blue light commonly used to excite green fluorescent proteins (e.g. 488 nm)[96] and neuronal aggregation[103].

Figure 1 Structure-guided engineering of oROS-HT$_{635}$: bright far-red optogenetic sensor for H_2O_2.

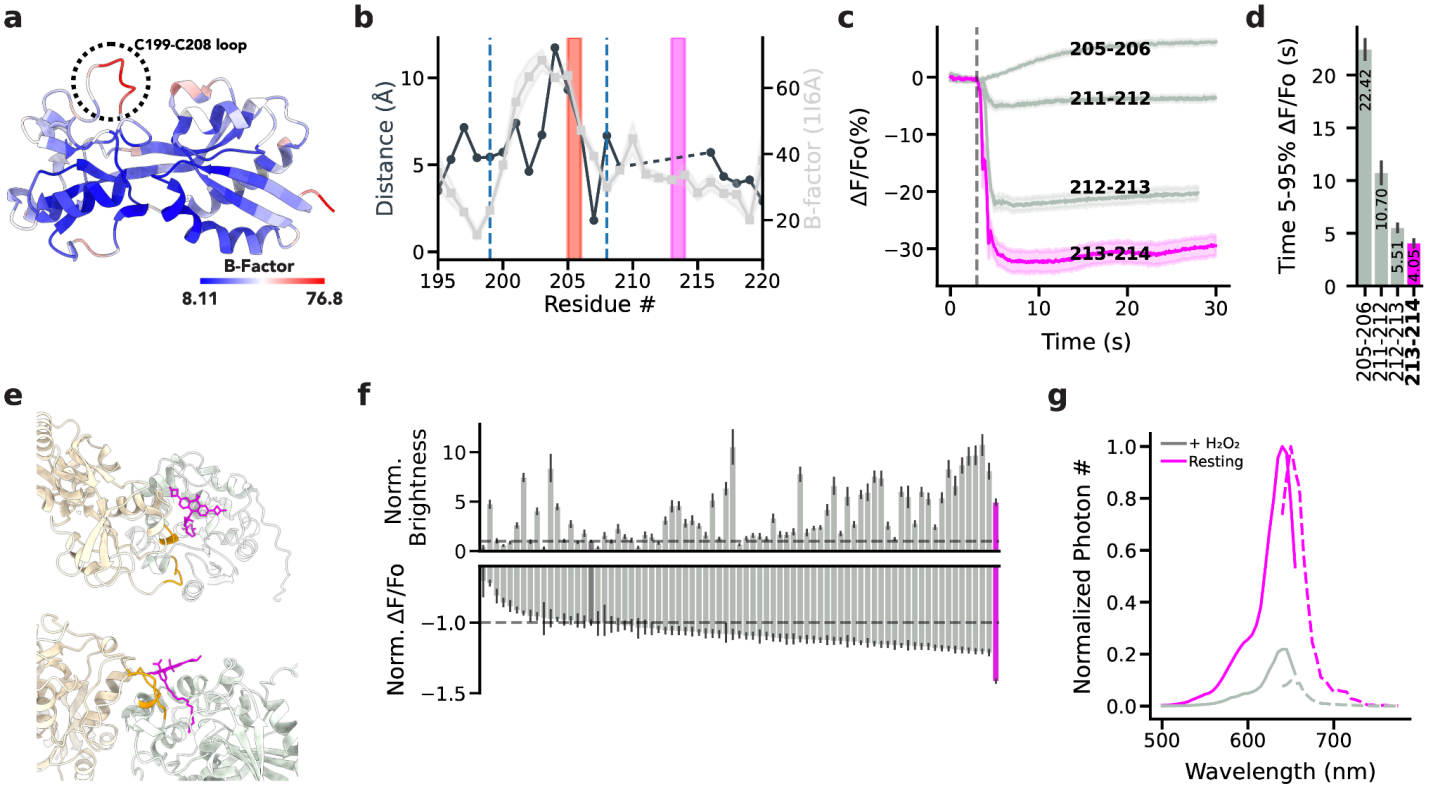

a B-Factor of the regulatory domain (RD) of the oxidized form of E. coli OxyR [PDB:1I6A] indicates flexible (red) and rigid regions (blue). The flexible loop between C199-C208 facilitates disulfide bridging of C199 and C208 residues. **b** Pairwise distance between residues #195 to #220 of oxidized [PDB:1I6A] and reduced [PDB:1I69] crystal structures of ecOxyR RD (Gray line) indicate intramolecular dynamics during H_2O_2 binding. Average B-factor of residues #195 to #220 in oxidized ecOxyR RD [PDB:1I6A] (Black line). The dashed lines indicate C199 and C208. The red and magenta bars indicate the insertion sites of fluorescence reporters in HyPerRed (cpmApple) and oROS-HT (cpHaloTag), respectively. **c** Prototype variants of oROS-HT_{635} from cpHaloTag (cpHaloTag7, from HaloCaMP1a) insertional screening between residues #211 to # 214 of ecOxyR. Fluorescence change (ΔF/Fo %) in response to extracellular H_2O_2 (300 μM) stimulation on the variants expressed in HEK 293 cells. (n>100 cells per variant) **d** Kinetics of variants depicted in (**c**) shown as time for the change in fluorescence from 5-95% ΔF/Fo. **e** Putative JF635 dye position bound to cpHaloTag (grey) in the predicted oROS-HT structure. The ColabFold predicted structure of the 213-214 cpHaloTag variant was superimposed with the cpHaloTag crystal structure (PDB:6U2M) to obtain a relative position of JF635 on the 213-214 cpHaloTag variant. *grey*: cpHaloTag (reporter domain) *beige*: OxyR (sensing domain) *orange*: linkers, *magenta:* JF635-HTL. **f** Random linker mutagenesis screening of linkers between both domains (X-cpHaloTag-XX) in HEK 293 cells. ***top*** Normalized brightness (213-214 variant at 1.0) of each sensor variant. ***bottom*** Normalized ΔF/Fo (213-214 variant at -1.0) of each sensor variant with 300 μM H_2O_2 stimulation. Magenta = oROS-HT, Dark Gray = variant 211-212, and dashed lines = mean of 211-212. **g** Spectral profile of oROS-HT expressed in HEK 293. Solid line: excitation spectra (peak: 640nm), dotted line: emission spectra (peak: 650nm). **Statistics:** Error bars and bands represent the bootstrap confidence interval (95%) of the central tendency of values using the Seaborn (0.11.2) statistical plotting package. Cells of interest were collected from three biological replicates unless noted otherwise.

Deo et al. proposed a chemigenetic solution for designing optogenetic sensors which entails incorporating a self-labeling enzyme (HaloTag) with an irreversible conjugation of rhodamine-based Janelia Fluorophores (JF)[104,105]. Red to far-red shifted JFs exhibit exceptional photophysical characteristics such as brightness and photostability, which surpass existing red FPs. We aimed to engineer a new class of GEHIs using cpHaloTag labeled with the far-red fluorescent JF635 as a reporter domain. Insertion of cpHaloTag into multiple positions outside of the C199-C208 loop in ecOxyR showed accelerated responses to 300 μM H_2O_2 in contrast to the variant with 205-206 insertion demonstrating improved sensor kinetics associated with alternative domain insertion strategy, and we identified a prototype sensor variant with insertion at 213-214 with a robust response to bolus 300 μM H_2O_2 (ΔF/Fo%: -38.23%; ci = [-40.36, -36.18], Time (s) ± stdev 5-95%: 4.05 ± 2.83) **[Fig. 1c, d].** Interestingly, we observed inverse responses (e.g. increase in peroxide level leads to decreased fluorescence) to peroxide in all cpHaloTag insertions outside of the C199-C208 loop. Therefore, we prioritized improving the brightness, guided by structures predicted from ColabFold (AlphaFold2 with MMseqs2 for multiple sequence alignment)[98]. The prediction yielded a highly confident structure of variant 213-214, exemplified by a dimeric interface of the sensing domain that closely resembles the dimeric interface of reduced ecOxyR resolved by

crystallography **[Supplementary Fig. 1a, b].** We superimposed the cpHaloTag-JF635 structure from [PDB: 6U2M] to identify the putative position of JF635 with the sensing domain of variant 213-214 **[Supplementary Fig. 1c].** The prediction showed "exposed" domain positioning, where OxyR sensing domain was oriented away from JF635 rather than enclosing the JF635 fluorophore **[Fig. 1e, Supplementary Fig. 2]**, increasing the potential influence of interdomain linker regions on the fluorophore's local environment. This configuration **[Supplementary Fig. 1b, 2]** is consistent with the spatial configuration of the chemigenetic calcium indicator HaloCaMP[104].

Consequently, random mutagenesis of interdomain linker residues (XX-cpHaloTag-X, X indicates mutagenesis targets) affected both the sensor brightness and dynamic range **[Fig. 1f].** From the linker variant library, we found a variant (TG-cpHaloTag-R) with 4.9-fold increased resting brightness and a 41% increase in dynamic range induced by 300 μM H_2O_2 compared to those of variant 213-214 (Relative fluorescence intensity: variant 213-214: 160.71; ci = [153.03, 168.79], TG-cpHaloTag-R: 788.24; ci = [742.26, 834.7]) (Dynamic range: 213-214: 160.71 (n = 1468); ci = [153.03, 168.79], TG-cpHaloTag-R: -67.99 (n = 1218); ci = [-68.52, -67.45]), which was later named oROS-HT_{635} **[Fig. 1g]**. In addition to the structural hypothesis of the interdomain linker's influence on both sensor dynamics and brightness, we also identified F209 to be a putative mutational site for the fluorophore local environment tuning, resulting in a more than a three-fold difference in resting brightness between the dimmest variant (F209L) and the brightest variant (F209R) and the trend was also consistent when the sensor was labeled with ligand JF585. Unfortunately, mutational benefits of TG-cpHaloTag-R and F209R were non-synergistic, which led us to exclude mutation F209R for our final variant **[Supplementary Fig. 3a-d]**.

3.3.2. oROS-HT_{635} is a highly sensitive and fast H_2O_2 sensor with far-red excitation/emission wavelengths.

We first characterized oROS-HT_{635} by exogenously applying H_2O_2 to cells expressing the sensor and second by applying menadione, which induces intracellular peroxide generation. Menadione generates H_2O_2 through various redox cycling mechanisms[51,52,54,106] **[Supplementary Fig. 4a]**. Saturation of oROS-HT_{635}

induced by 300 μM H_2O_2 revealed a fast sub-second activation that could capture the extracellular H_2O_2 diffusion across the imaging field of view. It implies that the kinetic efficiency of the sensor passed a milestone of no longer being reaction-limited in this scenario. Intriguingly, the response amplitude of oROS-HT_{635} at 10 μM external peroxide was -58.69% ΔF/Fo (ci = [-59.18, -58.18]), which is 87% of the amplitude at saturation upon 300 μM peroxide (-67.27% ΔF/Fo; ci = [-67.64, -66.91])), demonstrating the exceptional sensitivity of the sensor **[Supplementary Fig. 4b]** compared to previously reported red GEHIs**.** Previous studies showed the intracellular H_2O_2 concentrations in HEK293 cells are at approximately 10 and 300 nM under these external conditions, respectively[3,26]. Moreover, we titrated extracellular H_2O_2 as a sensitivity benchmark and found that oROS-HT is more sensitive than HyPerRed and HyPer7[28], a green fluorescent H_2O_2 sensor **[Fig. 2a]**. Furthermore, oROS-HT_{635} allowed the monitoring of titrated peroxide levels in HEK293 cells induced by 10, 20, and 50 μM of menadione. We measured a concentration-dependent response in oROS-HT_{635} signal of -26.8% ΔF/Fo (ci = [-27.63, -25.98]), -59.59% ΔF/Fo (ci = [-60.48, -58.67]), and -63.06% ΔF/Fo (ci = [-63.59, -62.51]) in ΔF/Fo, respectively **[Supplementary Fig. 4c]**. Interestingly, under 50 μM menadione, oROS-HT_{635} reaches near maximum fluorescence amplitudes but at much slower rates than exogenously induced instant H_2O_2 saturation (300 uM). Therefore, these kinetics most likely show the real-time increase of cytosolic peroxide by menadione.

Figure 2 Characterization of oROS-HT: a bright, sensitive, and fast H_2O_2 sensor.

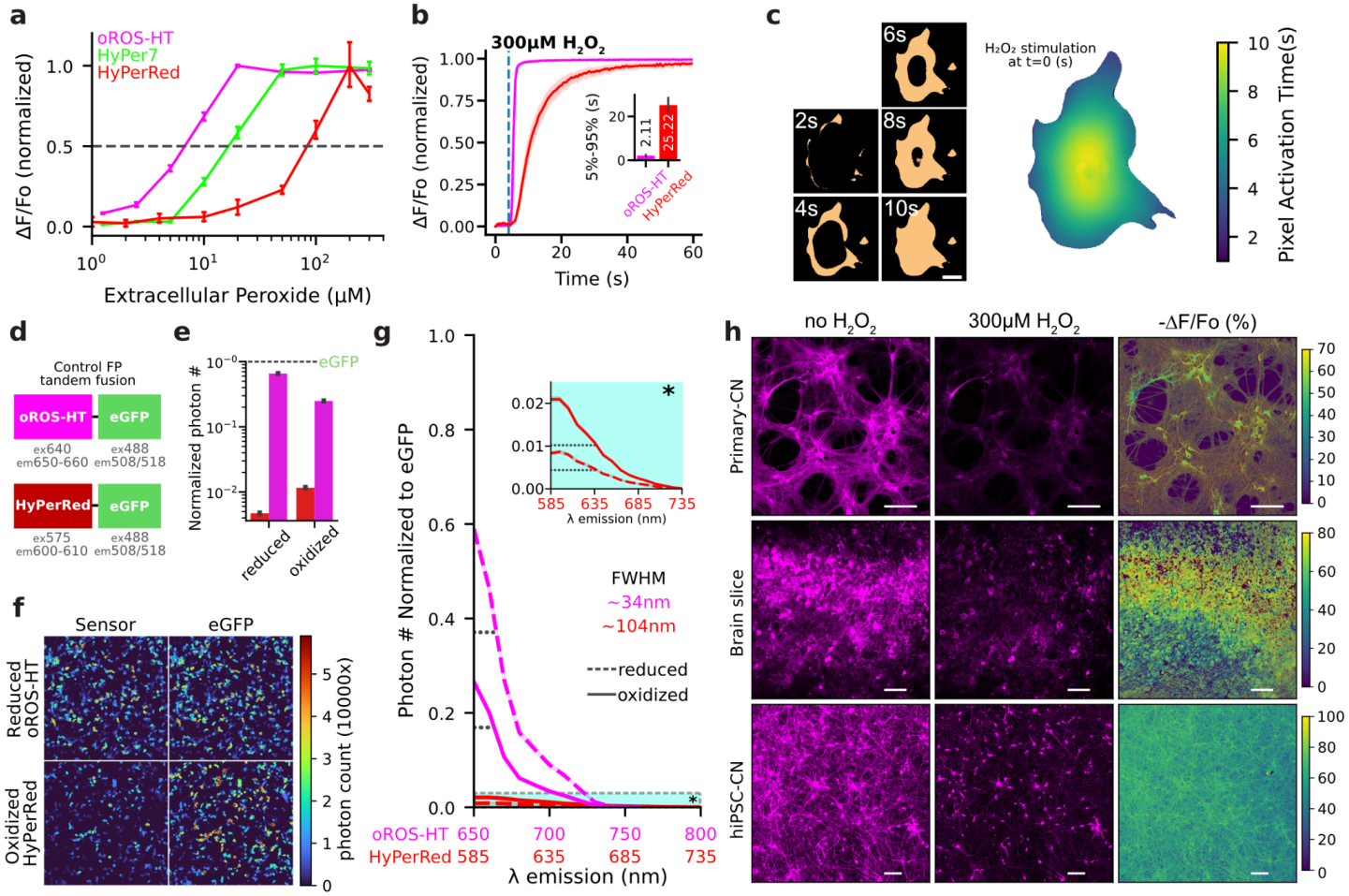

a H_2O_2 sensitivity benchmarking of oROS-HT, HyPer7, and HyPerRed using extracellular H_2O_2 titration. Each sensor was expressed in HEK293 cells. Fluorescence responses (ΔF/Fo) were scaled to the highest response observed (amongst all H_2O_2 conditions, n>100 cells each). **b** Normalized response of oROS-HT_{635} and HyPerRed to exogenous 300 μM H_2O_2 (n=23, cells per sensor). ***Inset:*** Time for change in fluorescence from 5-95% ΔF/Fo. **c** Intracellular diffusion of H_2O_2 across a hiPSC-CM expressing oROS-HT_{635} captured at 20Hz frame rate upon 300 μM H_2O_2 extracellular administration. ***Left:*** In the image series, pixel values are boolean-gated for 50% or above sensor activation to enhance contrast for H_2O_2 diffusion. Scale bar = 50 μm. ***Right*** A diffusion map representing pixel-wise activation time(s). **d** Assessment of relative cellular brightness with fluorescent protein eGFP fused to H_2O_2 sensors as reference. **e** Photon counts (#) reported for each sensor's emission window (at 10nm width) were normalized to corresponding eGFP photon counts from the same measurement. Reduced: photon counts at the resting state. Oxidized: photon counts after 300 μM H_2O_2 stimulation. Ratios were log-transformed for enhanced visual comparison (n>100 cells each, excitation intensity was matched among all constructs). **f** Representative raw images of each tandem fusion variant at their brightest states. Image size: 775 μm x 775 μm. **g** Quantitative emission spectra (starting from their respective emission maxima) for each sensor normalized to photon counts from its fused eGFP. Red: Hyper-Red, Magenta: oROS-HT. Sky blue inset: magnified HyPerRed-eGFP spectra (n>100 cells each). Dashed lines denote the half width at half maximum of oROS-HT and HyperRed spectra from which we approximated their full width at half maximum (FWHM). **h** Expression of oROS-HT in primary cortical neurons (Primary-CN), *ex vivo* rat cortex (Brain slice), and hiPSC-derived cortical neurons (hiPSC-CN) and their responses exogenous 300 μM H_2O_2. Scale bars: 100 μm. **Statistics:** Error bars and bands represent the bootstrap confidence interval (95%) of the central tendency of values using the Seaborn (0.11.2) statistical plotting package. Cells of interest were collected from three biological replicates unless noted otherwise.

Additionally, the oROS-HT$_{635}$ response kinetics were significantly faster under saturating 300 uM peroxide compared to HyPerRed (5-95% |ΔF/Fo| time, oROS-HT$_{635}$: 0.96 s; ci = [0.87, 1.04], HyPerRed: 7.8 s; ci = [6.98, 8.72]) **[Fig. 2b]**. Many experimental studies of intracellular peroxide often assume well-mixed uniformity of peroxide concentrations[18,48]. However, a previous model for cytosolic H_2O_2 also showed spatial peroxide gradients in mammalian cells can emerge upon external peroxide stimulation[48]. Exceptional kinetics of oROS-HT$_{635}$ demonstrated spatial peroxide diffusion in cardiomyocytes when exposed to bolus 300 μM H_2O_2 **.** For the first time, we optically monitored the influx of H_2O_2 into hiPSC-CMs with subcellular resolution, demonstrating that the sensor dynamics reflect the diffusion event **[Fig. 2c]**.

Next, we measured its brightness when expressed in cells since several studies indicate discrepancies between in vitro and cellular brightness[107,108]. First, we fused eGFP to the C-terminus of both sensors as a reference for fluorescent output. We conducted lambda scans across the visible spectrum using a confocal microscope with a white light laser. The detector system provided accurate photon counting with minimal dead time[109]. We measured each sensor's cellular brightness by normalizing photon counts at reduced and oxidized states to the photon count of their fused eGFP reference. Importantly, we excited eGFP, HyPerRed, and oROS-HT$_{635}$ at an equivalent laser power (49 μW) **[Fig. 2d]**. Based on the normalized photon count, the dimmest (e.g. oxidized) state of oROS-HT$_{635}$ was ~20-fold brighter than the brightest (e.g. reduced) state of HyPerRed **[Fig. 2e, f]**. In addition, oROS-HT displayed a narrower emission spectrum than HyPerRed, making it ideal for efficient spectral separation in multi-color imaging. The Full Width at Half Maximum (FWHM) is ~34 nm for oROS-HT and ~104 nm for HyperRed **[Fig. 2g]**. In addition, oROS-HT showed a better quantum efficiency (0.216) compared to existing far-red shifted fluorescence proteins[110]. oROS-HT$_{635}$ also displayed robust expression in various mammalian tissues (e.g. primary rat cortical neurons and *ex vivo* rat brain tissue) and human stem cell-derived models (e.g. cardiomyocytes and cortical neurons) **[Fig. 2h]**. Specifically, oROS-HT$_{635}$ expressed in cells did not produce noticeable aggregates, as often found in redFP-based indicators[111–113]. oROS-HT635 also displayed higher levels of monomericity compared to HyPerRed, as shown

by our OSER assay **[Supplementary Fig. 5]**. Lastly, oROS-HT$_{635}$ could be repeatedly activated and reduced back to baseline by serial peroxide stimulation and washout, demonstrating the reversibility of the sensor. Thus, the sensor can track real-time fluctuations of intracellular peroxide **[Supplementary Fig. 6]**.

Figure 3 Biophysical properties and versatility of oROS-HT$_{635}$ under varying environmental conditions.

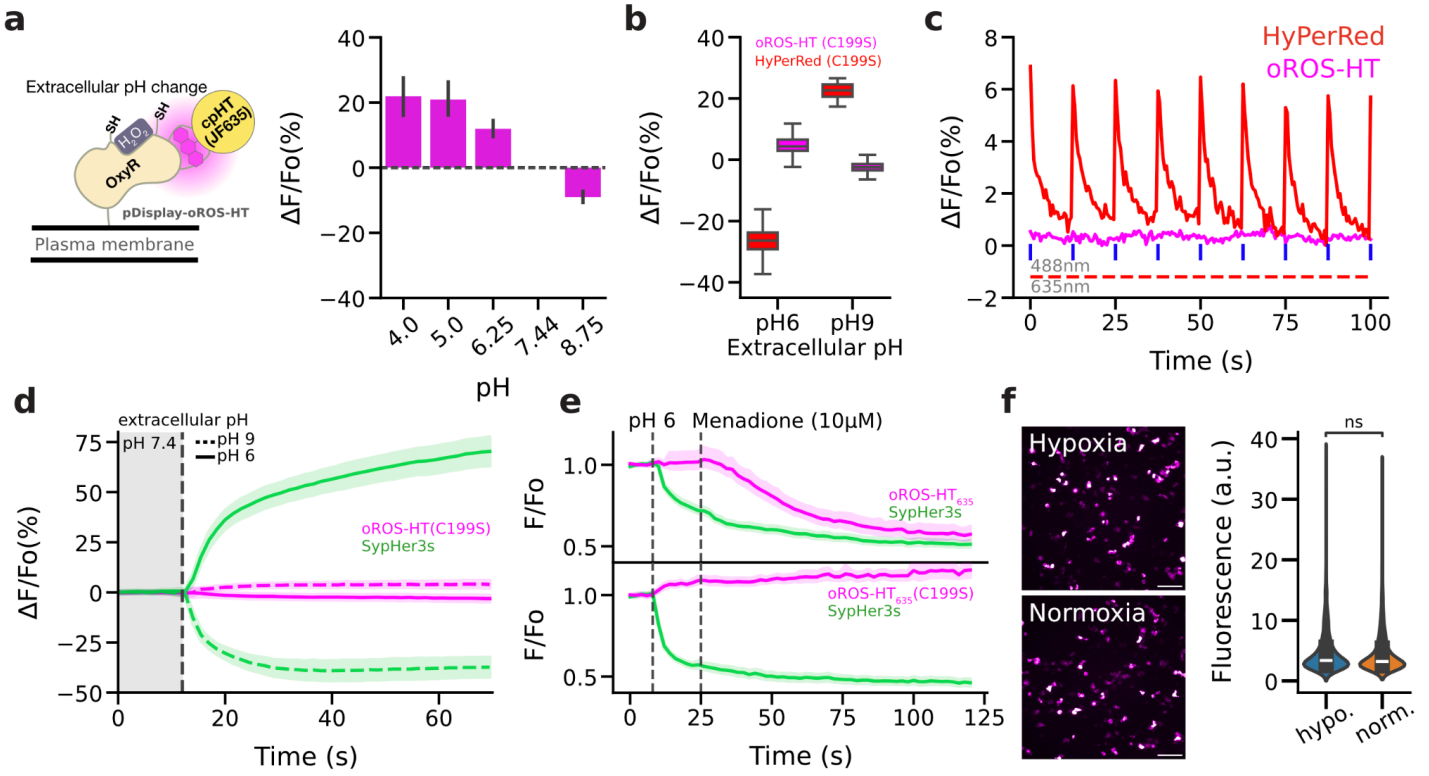

a pDisplay-oROS-HT$_{635}$ for extracellular expression of oROS-HT$_{635}$. pDisplay-oROS-HT$_{635}$'s fluorescence at varying media pH conditions (n>100 cells). Values change were normalized to fluorescence intensity at pH 7.44 as baseline (dashed line). **b** ΔF/Fo (%) of cytosolic oROS-HT$_{635}$-C199S (loss-of-function) and cytosolic HyPerRed-C199S expressed in HEK293 cells exposed at extracellular pH 9 or pH 6 (n>100 cells). **c** Representative fluorescence emission of oROS-HT and HyPerRed under their respective excitation wavelength (635nm and 597nm) and in response to 488nm light pulses. **d** Multiplexed imaging of oROS-HT$_{635}$-C199S and green fluorescent pH sensor SypHer3s co-expressed in HEK293 cells. Neutral imaging solution (pH 7.44) was switched to either acidic (pH6) or basic (pH9) imaging solution at the vertical dashed line (gray). **e** Dual monitoring of pH and H_2O_2 in mammalian cells. Either oROS-HT$_{635}$ or oROS-HT$_{635}$-C199S were paired with SypHer3s, a green fluorescence pH indicator, to be co-transfected on HEK 293 cells to monitor the sequential events of 1.) pH environment change (pH 6) and 2.) Menadione (10 μM) induced H_2O_2 increase. (n>100 per condition)**.** **f** Maturation of oROS-HT$_{635}$-C199S under hypoxic condition. HEK293 expressing loss-of-function oROS-HT(C199S) were incubated for 18 hours in either normoxia (atmospheric condition at 37°C) or hypoxia (N2 infused chamber at 37°C) overnight (18h). ***Left*** Representative images of oROS-HT$_{635}$-C199S maturated in HEK293 cells in Hypoxia or Normoxia conditions. Scale bar = 100 μm. ***Right*** Fluorescence intensity profile of oROS-HT$_{635}$-C199S (Hypoxia [n = 1246] / Normoxia [n=1765] collected from 8/11 biological replicates, respectively). **Descriptive Statistics:** Error bars and bands represent the bootstrap confidence interval (95%) of the central tendency of values or standard deviation from the mean (d) using the Seaborn (0.11.2) statistical plotting package. Cells of interest collected from 3 biological replicates. **Inferential Statistics:** f: t-test independent samples. *P < 0.05, **P < 0.01, ***P < 0.001.

3.3.3. oROS-HT$_{635}$ allows environmentally stable real-time H_2O_2 monitoring.

We envision users of oROS-HT$_{635}$ to study peroxide dynamics under varying conditions. Thus, we further characterized notable features of oROS-HT$_{635}$ that demonstrate its environmental resiliency. ecOxyR-based H_2O_2 sensors have been shown to possess superior specificity towards H_2O_2 compared to chemical H_2O_2 tracers[18,23,26]. This specificity stems from its unique hydrogen bond network in the ligand binding pocket network that induces H_2O_2-specific disulfide linkage between two highly conserved cysteine residues (exOxyR-RD C199-C208). Consistent with previous reports, disabling disulfide formation by a C199S mutation eliminates the H_2O_2-induced fluorescence (loss-of-function), demonstrating that oROS-HT$_{635}$ responses are H_2O_2 specific. Nevertheless, fluorescence is intrinsically prone to environmental artifacts, including pH change, absorption, and interference from autofluorescence. As a negative control, oROS-HT$_{635}$-C199S can reflect environmental effects on the fluorescent signals not generated by H_2O_2 sensing[26] **[Supplementary Fig. 7]**. oROS-HT$_{635}$ exhibits improved resiliency to environmental factors (e.g. pH, photo-artifact, aggregation, and oxygen) compared to the red-fluorescent H_2O_2 sensor, HyPerRed. We observed pH-dependent fluorescence changes in extracellular oROS-HT **[Fig. 3a].** However, a comparison between intracellular oROS-HT$_{635}$ and HyperRed demonstrated a noticeably improved pH resilience in oROS-HT$_{635}$ **[Fig. 3b]**. Red-shifted GEHIs are often limited for polychromatic use with green sensors due to a photochromic false positive artifact in response to blue light[114]**.** oROS-HT$_{635}$ lacks this artifact, rendering oROS-HT$_{635}$ more compatible with green reporters **[Fig. 3c].** To demonstrate its dual-color imaging capability, we co-expressed oROS-HT$_{635}$ or oROS-HT$_{635}$-C199S with a GFP-based pH indicator SypHer3s to simultaneously image H_2O_2 and pH changes. Extracellular pH insults (pH 6 and 9) resulted in corresponding cytosolic changes as confirmed by SypHer3s while the fluorescence of oROS-HT$_{635}$-C199S was not affected **[Fig. 3d]**. Next, we tested whether oROS-HT$_{635}$ maintains function under an acidic pH insult (pH 6). oROS-HT$_{635}$ did not respond to the initial change in pH, as confirmed by SypHer3s responses, but the menadione-induced increase in cytosolic peroxide was still detected **[Fig. 3e]**, exemplifying robust functionality under changing cellular pH environments**.** Most beta-barrel

fluorescent proteins in sensor designs require oxygen for their fluorophore maturation[115,116]. In addition, it was reported that GFP undergoes photoconversion under hypoxic conditions, where the excitation/emission spectra shift and become similar to RFP[117]. In contrast, the HaloTag-Rhodamine-based chemigenetic sensors incorporate synthetic fluorophores, which do not require oxygen for protein maturation. HEK293 cells transfected with oROS-HT_{635}-C199S did not significantly differ in fluorescence level when matured under normoxic or hypoxic conditions **[Fig. 3f]**.

3.3.4. Multiparametric analysis of the acute effect of auranofin on H_2O_2, redox potential, and Ca^{2+}.

3.3.4.1. Acute Trx/Gpx inhibition leads to transient H_2O_2 increase and Nrf2 nuclear translocation.

Grx1-roGFP2 is an indicator sensitive to glutathione redox potential (E_{GSH}). It is a fusion between glutaredoxin1 (grx1) and the redox-sensitive green fluorescent protein roGFP2. Multiplexed imaging of oROS-HT_{635} with Grx1-roGFP2 could enable peroxide imaging with augmented information about the redox cellular environment. Here, we monitored both sensors simultaneously in HEK293 cells upon 10 µM H_2O_2 exposure. We revealed sequential events of intracellular peroxide increase followed by a decrease in glutathione redox potential E_{GSH} ($peak_{oROS\text{-}HT}$ to $peak_{Grx}$ = 3.12 s) as indicated by the respective sensor responses **[Fig. 4a].** In contrast, the inhibition of cellular redox potential using the Trx/Grx (Thioredoxin/Glutaredoxin) inhibitor auranofin (1 µM) showed a rapid decay of E_{GSH} followed by a slow increase of the intracellular peroxide level. Interestingly, the auranofin-induced peroxide build-up was transient, as we observed the elevation in peroxide level for 45 minutes after the application, followed by a recovery to the baseline within the next 60 minutes **[Fig. 4b].** The reversal of peroxide levels could be triggered by increased stress-induced antioxidative response. We observed increased translocation of Nrf2 into the nucleus in HEK 293 cells within 30 minutes of exposure to 1 µM Auranofin **[Fig. 4c, Supplementary Fig. 8].** The translocation of Nrf2 is a hallmark of rapid cellular antioxidative responses consistent with the previous findings[55,118]. Aligning with our results, they confirmed fast Nrf2 nuclear translocation within 10 minutes to 1 hour. Hence, we conclude that Nrf2 triggered an antioxidant cellular response and subsequently reversed the pharmaceutically induced increase in H_2O_2 levels. The

multiplexed use of Grx1-roGFP2 with oROS-HT$_{635}$ established a temporal and spatial correlation between peroxide levels and the cellular redox environment.

Figure 4 Multiparametric analysis of the acute effect of auranofin on H_2O_2, redox potential, and Ca^{2+}.

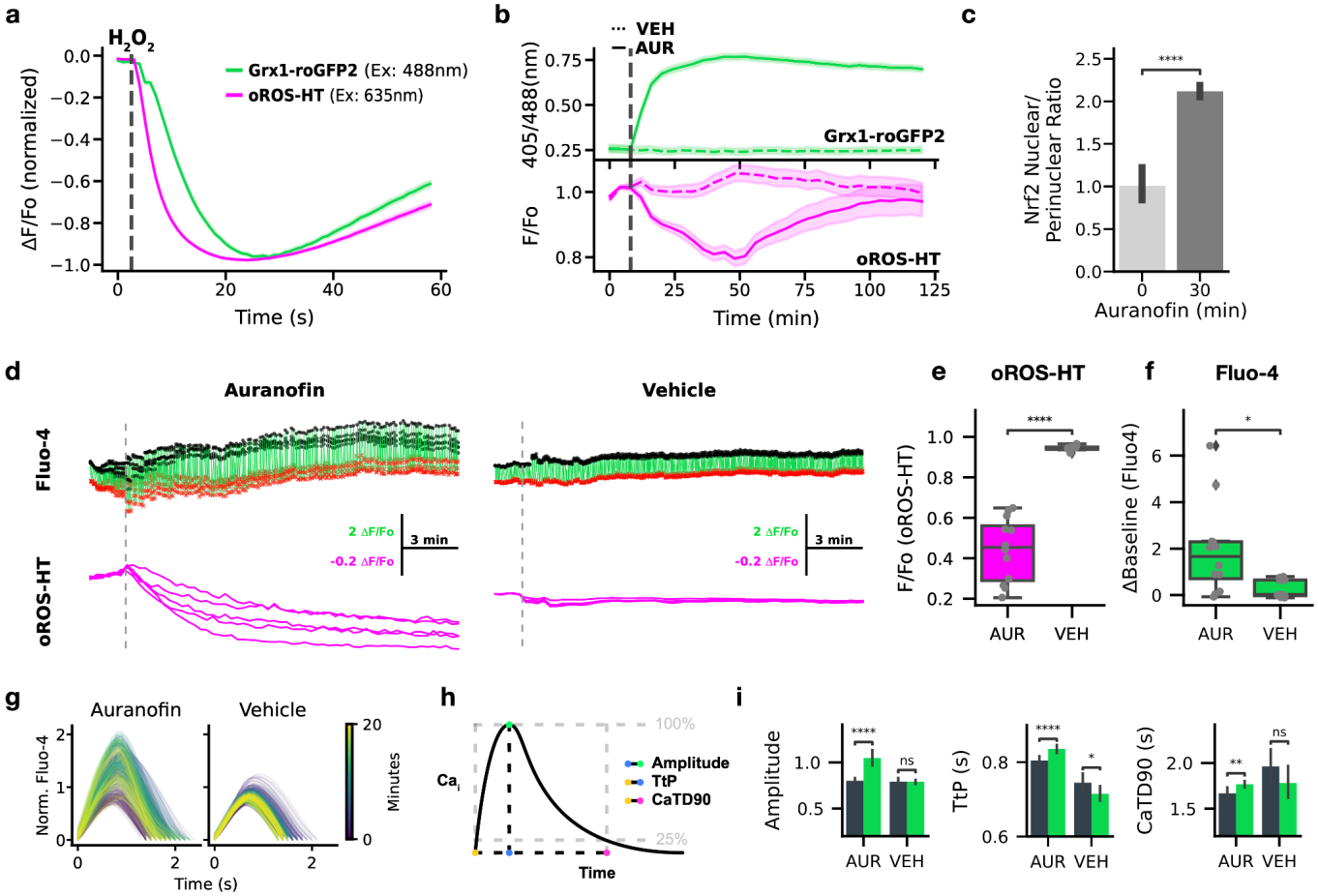

a-c Dual monitoring of intracellular glutathione redox potential and H_2O_2. **a** Normalized fluorescence change of Grx1-roGFP2 (green, glutathione redox potential sensor) and oROS-HT (magenta) co-expressed in HEK293 in response to 10 µM H_2O_2 (at the gray line, n>100 cells, collected from 3 biological samples). **b** Traces of auranofin (Trx/Gpx inhibitor) -induced changes on Grx1-roGFP2 and oROS-HT sensors co-expressed in HEK293 cells. Grx1-roGFP2 responses (green) are shown as the ratio of 510nm emission at 405 and 488nm excitation. oROS-HT's responses (magenta) are shown as relative fluorescence change from the baseline (ΔF/Fo). Auranofin or vehicle was applied shortly after the start of the imaging sessions (gray dashed line). The dotted trace for each sensor plot represents responses to vehicle treatment (n>100 cells per condition, collected from 3 biological samples per condition). **c** Translocation of Nrf2 (in nuclear/perinuclear ratio) quantified from immunofluorescence staining of Nrf2 in HEK293 cells exposed to 1 µM auranofin for 30 minutes or negative controls (n>100 cells per condition, collected from 5 biological samples per condition). Detailed analysis method described in Supp. Fig. 8. **d-i** Dual imaging of Ca^{2+} (Fluo-4, green fluorescence calcium dye) and H_2O_2 in hiPSC-CMs in response to 5 µM auranofin. (n=12 for auranofin, n=11 for Vehicle conditions, ROIs from three different biological replicates) **d** Representative traces of oROS-HT (magenta) with Fluo-4 (green) in hiPSC-cardiomyocytes. Peaks (Blue dots) and troughs (red crosses) of Ca^{2+} transients (CaT) are labeled. **e** oROS-HT ΔF/Fo at last frames. **f** Change in resting fluorescence intensity (ΔBaseline) of Fluo-4 from the start to the end of the imaging. **g** Representative CaT changes over time. **h** Schematic description of the CaT phenotypes extracted. **i** Characterization of CaTs from early (first 70 seconds) and late segments (last 70 seconds) of auranofin and Vehicle treated hiPSC-CM groups: ***Left*** Amplitude (amplitude of CaT at the peak), ***middle*** TtP (Time-to-Peak), and ***right*** CaTD90 (CaT

Duration 90). Descriptive Statistics: Error bars and bands represent the bootstrap confidence interval (95%) of the central tendency of values using the Seaborn (0.11.2) statistical plotting package. Inferential Statistics: t-test independent samples. *P < 0.05, **P < 0.01, ***P < 0.001. ****P < 0.0001.

3.3.4.2. Acute Trx/Gpx inhibition in hiPSC-CM leads to H_2O_2 increase and altered Ca^{2+} transients.

While there is growing evidence of a mutual interplay between redox and Ca^{2+} dynamics in biological systems[119], existing molecular imaging tools are limited to asynchronous studies of Ca^{2+} and H_2O_2 in biological systems. On the other hand, simultaneous measurements would provide a distinct advantage in establishing a better temporal and spatial correlation between these two biological phenomena. Polychromatic measurements of H_2O_2 with oROS-HT_{635} could enable simultaneous real-time observations of oxidative stress and Ca^{2+} in the same cell with a temporal resolution that can capture dynamic Ca^{2+} transients (CaTs). Here, we performed dual-color imaging of H_2O_2 and CaT using oROS-HT_{635} with Fluo-4, a Ca^{2+}-sensitive green fluorescent dye in hiPSC-CMs **[Fig. 4d].** It is widely accepted that oxidative stress perturbs key Ca^{2+} transporters like ryanodine receptors sarcoplasmic reticulum Ca^{2+} leak)[120], L-type calcium channels (I_{CaL}, inward Ca^{2+} current)[121], and sarcoplasmic reticulum calcium ATPase pumps (SERCA, decreased Ca^{2+} reuptake)[63,65,66]. Physiological effects of these perturbations can include changes in specific CaT phenotypes such as baseline Ca^{2+}level, CaT amplitudes, Time-to-Peak (TtP, on-kinetics), and Calcium Transient Duration 90% ($CaTD_{90}$, completion of 90% of one CaT period). We tested how the auranofin-induced acute oxidative stress perturbs Ca^{2+} dynamics. Previous studies reported auranofin-induced Ca^{2+} increases in some cell types[122,123]. Indeed, auranofin (5 μM) induced peroxide increase **[Fig. 4e]** during the 20-minute imaging period, accompanied by an increase in basal Ca^{2+} level **[Fig. 4f].** Next, we extracted the CaT profile from the Fluo-4 imaging data for further characterization **[Fig. 4g, h].** Compared to the vehicle control, CaTs of auranofin-treated hiPSC-CM exhibited the following phenotypes: elevated CaT peak amplitude and prolonged TtP and CaTD90 **[Fig. 4i].**

3.3.4.3. Modeled perturbation of L-type Ca^{2+} channels recapitulate the observed changes in Ca^{2+} transients.

Here, we used a previously described "generalized" computational model[124] for hiPSC-CM electrophysiology to explore mechanisms of how oxidative stress leads to the observed CaT phenotypes (i.e.,

increased amplitude, TtP, and $CaTD_{90}$). Aligned with the reported effect of oxidative stress on the Ca^{2+} transporters discussed earlier, we modeled oxidative stress by modifying parameters corresponding to Ca^{2+} uptake from the cytoplasm to the SR via SERCA, SR Ca^{2+} leak amplitude, and L-type Ca^{2+} channel (I_{CaL}) conductance. Perturbing SR Ca^{2+} leak did not significantly alter CaT profiles, while modifying I_{CaL} and SERCA levels elicited changes in CaT **[Extended Fig. 4 a-c]**. We thus carried out a bivariate analysis to determine how CaT phenotype depended on SERCA and I_{CaL} levels. This revealed that CaT phenotypes aligned with experimental observations only emerged when synergistic perturbations were modeled **[Extended Fig. 4d]**. CaT profiles were generally more sensitive to changes in I_{CaL} compared to SERCA **[Extended Fig. 4e]**, consistent with previous reports identifying L-type Ca^{2+} channel as the primary CaT driver in hiPSC-CMs due to the functional immaturity of SR-associated Ca^{2+} transporters[125–129]. However, steady-state beating frequencies from the modeled perturbations ranged from 0.479 to 0.846 Hz, with a trend towards faster activity, aligning with experimental findings where Auranofin increased frequency in 2 of 3 replicates **[Supplementary Fig. 9a]**. To verify that observed changes in CaT phenotypes stemmed from parameter modifications rather than changes in intrinsic beating rate, we ran additional simulations **[Supplementary Fig. 9b]** by overdrive pacing the baseline model (0.5 Hz) up to 0.85 Hz. This resulted only in minor or opposite changes in CaT metrics—CaT amplitude decreased with pacing but increased under modifications simulating oxidative stress. Thus, while the CaT phenotypes in hiPSC-CMs are more responsive to changes in I_{CaL}, the experimentally observed CaT profiles only arise when both plasma membrane and SR components are synergistically perturbed. In other words, perturbations of both I_{CaL} and SERCA were sufficient to recapitulate the observed phenotypes. These results highlight the complex nature of the effect of oxidative stress on Ca^{2+} dynamics in cardiomyocytes, further emphasizing the need for systemic studies on the influence of oxidative stress on specific Ca^{2+} transporters and their synergistic interactions.

Extended Figure 4 Modeled interplay between I_{CaL} and SERCA reveals oxidative stress-induced Ca^{2+} dysregulation.

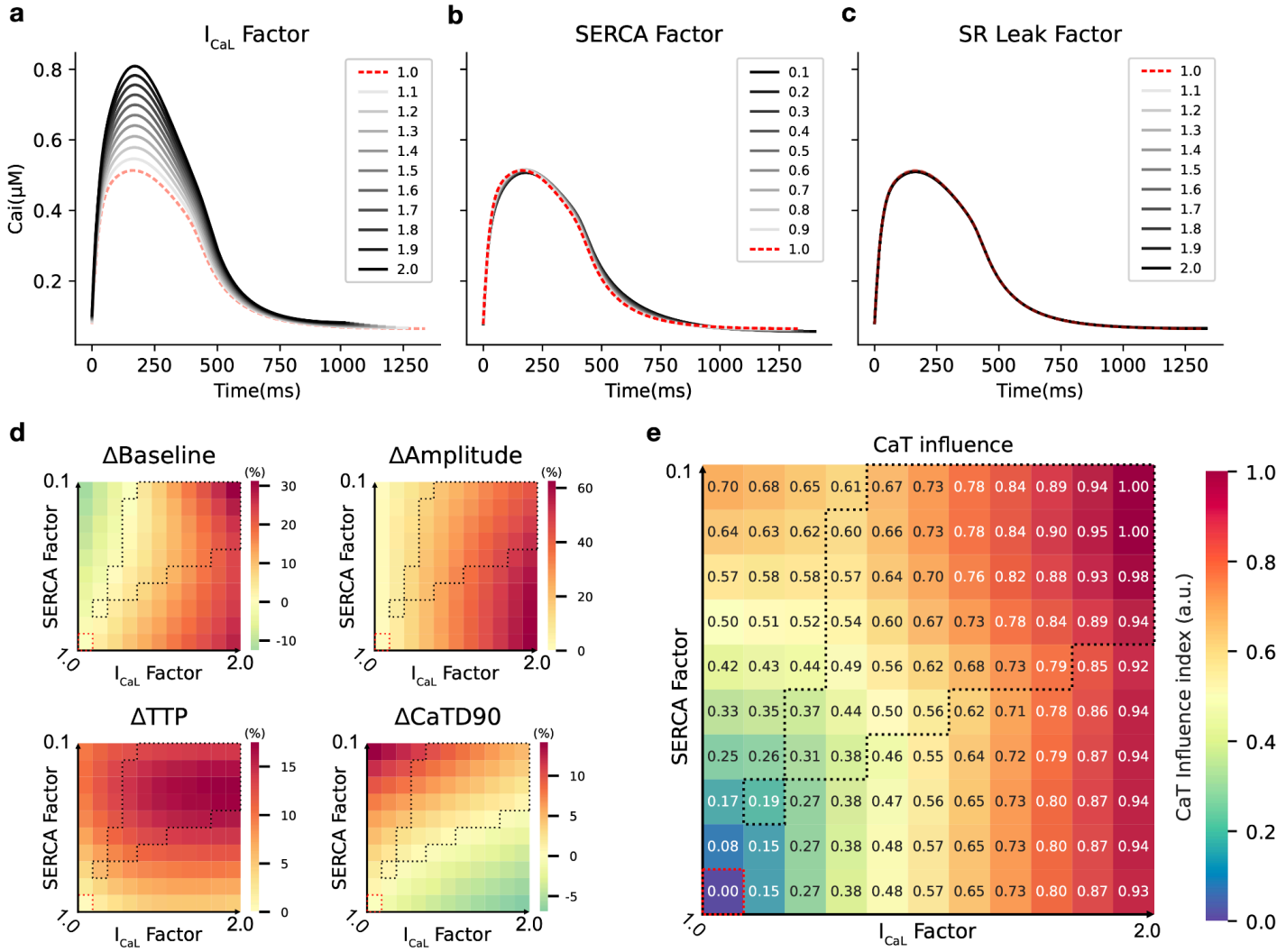

a-c Effects of oxidative stress-induced perturbation on **a** I_{CaL} conductance, **b** SERCA uptake, and **c** SR Ca^{2+} leak were simulated using a modified version of the hiPSC-CM computational model by Kernik et al. (total simulation time = 100 seconds, with baseline beating frequency of 0.5Hz calibrated to match experimental data). Plots display cytoplasmic CaT at steady state from each simulated condition. Red dash lines represent simulations without perturbation. **d** The synergy map shows the degree of difference in CaT phenotypes in each simulated condition compared to conditions with no perturbation (Δphenotype/$phenotype_{1.0}$ %). The grid boxes within the red, dotted boundary (lower left corner) indicate conditions without perturbation. The grid boxes within the black dotted boundary indicate conditions with phenotypic change consistent with experimental findings from Fig. 4 in the direction of positive (red) or negative (green) change with all four observed CaT phenotypes (ΔBaseline, ΔAmplitude, ΔTtP, ΔTtB and ΔCaTD90). **e** CaT influence map (I_{CaL} vs SERCA) derived from an additive weighting of absolute influence on each phenotype (|Δphenotype/$phenotype_{1.0}$| from ΔBaseline, ΔAmplitude, ΔTtP, ΔCaTD90). Synergistic perturbation of both I_{CaL} and SERCA was sufficient to recapitulate the experimentally observed CaT phenotypes.

3.3.5. Spatiotemporally resolved imaging of H_2O_2.

3.3.5.1. Menadione induces both intracellular and extracellular H_2O_2 generation.

We targeted oROS-HT_{635} to subcellular compartments, including the mitochondrial matrix, mitochondrial intermembrane space, actin cytoskeleton, and intracellular side of the plasma membrane, and more **[Fig. 5a, Supplementary Fig. 10].** Intracellular H_2O_2 generation is potentially localized and functionally differentiated in aerobic organisms[130], which calls for monitoring of H_2O_2 in a spatially resolved manner (e.g. in subcellular compartments)[18]. Growing evidence demonstrates the significant contribution of NADPH oxidase-sourced superoxide and peroxide in redox signaling and disease progression[6,16,46,131,132]. The oxidase generates H_2O_2 on the extracellular side of the cellular plasma membrane[133], constituting an extracellular pool of H_2O_2[39]. Furthermore, its intracellular distribution is achieved through autocrine (aquaporin-mediated diffusion of peroxide[134,135] into cells) and paracrine[136] mechanisms. We fused oROS-HT_{635} to a PDGFR transmembrane domain-based trafficking sequence (pDisplay vector, invitrogen) for extracellular membrane localization. Its co-expression with oROS-G, a sensitive and equivalently fast green variant of oROS that we previously engineered[101], was well-tolerated in HEK293 **[Fig. 5b].** We measured H_2O_2 increase in both extracellular and intracellular space upon 25 μM menadione applications. Intriguingly, we found that the extracellular peroxide response detected by oROS-HT_{635} (inverse response sensor) was faster than oROS-G (direct response sensor). This supports previous observations that menadione increases H_2O_2 in the extracellular space, potentially via NADPH oxidase-sourced H_2O_2[137–140] **[Fig. 5c, d].**

Figure 5 Spatiotemporally resolved imaging of H_2O_2.

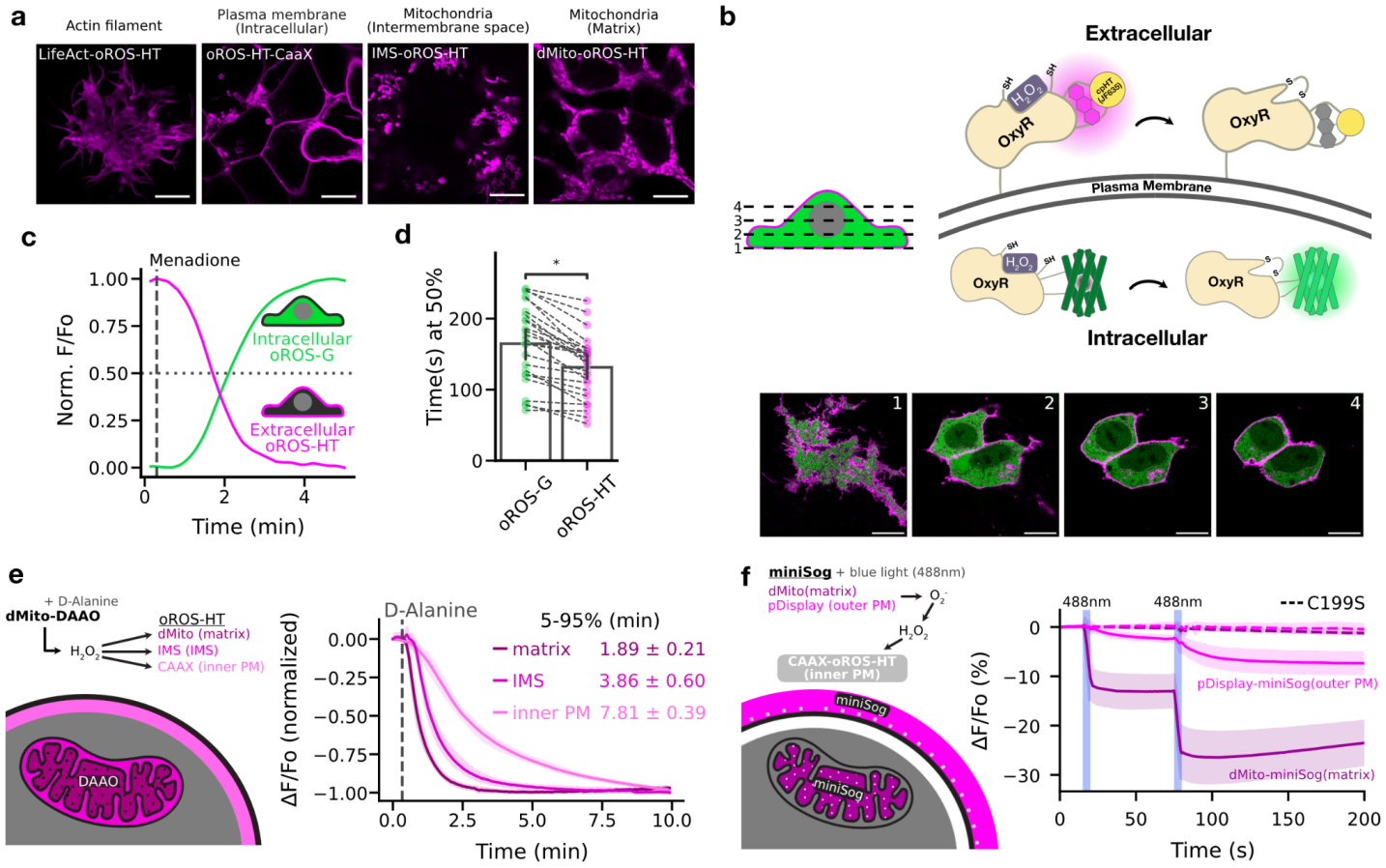

a Subcellular localization of oROS-HT_{635} was achieved by labeling peptide sequences for actin (LifeAct), mitochondrial matrix (dMito), mitochondrial intermembrane space (IMS), and intracellular side of the plasma membrane (CaaX). HEK 293 cells expressing each trafficking variant were live-imaged using a confocal microscope. Scale bar: 10 µM. **b** Confocal z-stack images of HEK293 cells co-expressing pDisplay-oROS-HT_{635} (extracellular side of the plasma membrane) and cytosolic oROS-G. Scale bar: 10 µM. **c-d** Fluorescence change of HEK 293 expressing pDisplay-oROS-HT_{635} and cytosolic oROS-G in response to 25 µM menadione imaged with epifluorescence microscope. Both sensors were imaged every second. **c** A representative trace of oROS-HT_{635} and oROS-G from a single cell. **d** Time (in minutes) at 50% sensor activation (n=25 cells from 4 biological replicates). **e** Activation kinetics of chemogenetically induced mitochondrial H_2O_2 to the mitochondrial matrix (matrix), intermembrane space (IMS), and inner plasma membrane (inner PM) (3 biological replicates, ± S.D. for 5-95% time). **f** Mini-Sog generated O^-_2 and H_2O_2 upon 488nm stimulation and was expressed at the outer PL or mitochondrial matrix. CaaX-oROS-HT measured optogenetically induced H_2O_2 diffusing to the inner PM (3 biological replicates). **Descriptive Statistics:** Error bars and bands represent the bootstrap confidence interval (95%) of the central tendency of values using the Seaborn (0.11.2) statistical plotting package. **Inferential Statistics:** t-test independent samples. *P < 0.05, **P < 0.01, ***P < 0.001. ****P < 0.0001.

3.3.5.2. Demonstration of spatial H_2O_2 diffusion towards the inner plasma membrane.

We visualized spatiotemporally resolved diffusion of H_2O_2 by combining subcellular variants of oROS-HT_{635} with compartment-specific chemogenetic and optogenetic H_2O_2-generating methods. We first targeted D-amino acid oxidase (DAAO)[28] to the mitochondrial matrix (dMito-DAAO), which generates H_2O_2 in response to D-alanine (50mM) supplementation. H_2O_2 generated in the matrix was tracked in different compartments, using subcellular oROS-HT_{635} at the source (dMito), the intermembrane space (IMS) and the inner plasma membrane (inner PM via CAAX sequence). As expected, the sensors captured the time course of the H_2O_2 diffusion from the mitochondria to the inner PM [5-95% ΔF/Fo (min ± std): dMito (1.81 ± 0.21), IMS (3.78 ± 0.60), CAAX (7.72 ± 0.39)] thereby revealing buffering along the path exemplified by the longer temporal delay of diffusion from IMS to the inner PM than from matrix to IMS **[Fig. 5e]**. In addition, the mitochondrial H_2O_2 from dMito-DAAO diffused outside of cells. We detected this paracrine diffusion of H_2O_2 in co-cultures of dMito-DAAO positive cells expressing cytosolic oROS-G (50% activation at ~20.3 minutes) and dMito-DAAO negative cells expressing cytosolic oROS-HT_{635} (50% activation at ~36.5 minutes) **[Supplementary Fig. 11]**. Furthermore, we employed the photosensitizer miniSOG. It produces singlet oxygen and superoxide upon 488 nm excitation, which subsequently dismutate to H_2O_2 via physiological mechanisms such as SOD[141,142]. By targeting miniSOG to two major endogenous H_2O_2 sources—the mitochondrial matrix (via dMito) and the outer plasma membrane (via pDisplay)—we assessed H_2O_2 diffusion toward the inner PM using CAAX-oROS-HT_{635}. Both mitochondrial and outer PM miniSOG induced detectable H_2O_2 increases at the inner PM. However, the mitochondrial matrix miniSOG produced a faster and more substantial response [First 488 nm pulse, min. ΔF/Fo (%) ± stdev: pDisplay (-2.46 ± 0.55), dMito (-13.19 ± 3.34); second 488 nm pulse, min. ΔF/Fo (%): pDisplay (-7.38 ± 2.14), dMito (-26.52 ± 5.17)] **[Fig. 5f]**. Combining dual-color H_2O_2 imaging and plasma membrane-specific expressions of oROS-HT_{635}, as demonstrated here, could establish new paradigms to study interactions between H_2O_2 sources and intra and extracellular targets with subcellular resolution.

3.4. Discussion

This study introduces a novel bright far-red chemigenetic indicator for peroxide, oROS-HT_{635}. To fully exploit the brightness of the JF635 rhodamine dye, we optimized the inverted-response sensor for higher brightness and dynamic range. Since oROS-HT_{635} maintains bright fluorescence in the sensor activation range (e.g. partially oxidized state), it detects high-fidelity signals at physiological peroxide levels **[Fig. 2g]**. By incorporating a chemigenetic reporter system (cpHaloTag-JF635), we achieved oxygen-insensitive, pH-resistant, and photochromic artifact-free imaging, extending its application range **[Fig. 3]**.

Harnessing oROS-HT_{635}'s multiplexing capability, we performed dual-color imaging paired with green fluorescence-based redox potential, Ca^{2+} and pH reporters, allowing monitoring of H_2O_2 levels simultaneously with changes in redox potential, Ca^{2+} or pH **[Fig. 3d,e, Fig. 4]**. Auranofin, a treatment for rheumatoid arthritis, is gaining attention from the cancer community as a potential therapeutic candidate due to its dose-and-cell-dependent multifaceted mode of action[143,144]. As a Trx/Gpx inhibitor, it attenuates the intracellular antioxidant capacity, which increases oxidative stress. Intriguingly, recent studies, aimed to repurpose auranofin as a potential cancer therapeutics, revealed a more nuanced role of auranofin as increasing cellular oxidative stress can activate regulators such as Nrf2 to boost cellular antioxidative capacity[143,144]. Here, we showed in real-time how low-dose auranofin initiates transient oxidative stress, followed by a Grx-independent reversal of H_2O_2 levels. The time course of the reversal correlated with increased Nrf2 translocation into the cell nucleus in HEK293 cells, supporting observations from previous studies **[Fig. 4b,c]**.

Auranofin-induced antioxidative perturbations also altered dynamic Ca^{2+} transients in hiPSC-cardiomyocytes, which we correlated with an increased level of H_2O_2. These observations could be recapitulated in our computational simulation of the effect of oxidative stress on two key Ca^{2+} transporters I_{CaL} and SERCA[66,119,120] **[Fig. 4d-i]**. Our findings align with previous work showing a close link between oxidative stress and Ca^{2+} transport across various cell types. We want to acknowledge the intricate nature of Ca^{2+} and redox interactions, which may become more pronounced in fully developed cardiomyocytes. This study focused on I_{CaL} and SERCA changes to replicate the observed responses in hiPSC-CMs. However, in mature heart cells, factors like cardiac dyad structure, mitochondrial function, and NCX activity may amplify the effects of ROS on Ca^{2+} dynamics. These complexities require further exploration of how these

interactions evolve with cellular development to better understand the roles of oxidative stress in calcium handling across diverse cell types and developmental stages.

Users can also exploit the remarkable subcellular targeting of oROS-HT$_{635}$ to monitor peroxide with higher spatial resolution closer to or farther from its sources. GEHIs have been pivotal in unraveling cellular peroxide topology by enabling optical monitoring of peroxide dynamics in a spatially resolved manner heavily focused on cytoplasmic and mitochondrial spaces[28,145]. oROS-HT$_{635}$ can aid users in studying peroxide biology by delineating the topology of peroxide from mitochondria, plasma membrane spaces[5–7], and paracrine peroxide[136], which is critical for understanding the systemic propagation of peroxide build-up in tissues. Specifically, membrane-tagged oROS-HT$_{635}$ provides new opportunities to investigate peroxide topology proximal to the plasma membranes[137–140] **[Fig. 5]**.

The JF635-based design of oROS-HT$_{635}$ led to critical advantages such as bright far-red fluorescence, oxygen-independency and reduced pH dependency. Because the dye covalently conjugates with the sensor, the fluorescence is not dependent on free dye concentration once the conjugation occurs. However, dependency on the exogenous dye creates a potential disadvantage of oROS-HT over existing cpFP based H_2O_2 sensors. The oROS-HT readout in this publication relies on intensiometric measurements, which makes signals inherently qualitative. Nevertheless, the sensor provides precise temporal and spatial correlations between H_2O_2-generating events and subsequent physiological phenomena.

The next iteration of oROS-HT$_{635}$ could be optimized for other JF dyes with shifted emission spectra ranging from (494 nm to 722 nm), further enhancing its flexibility in multiplexed optogenetic applications. Another possible avenue for future oROS-HT$_{635}$ development is maximizing its *in vivo* application capability. As a trade-off to its exceptional fluorogenicity, the bioavailability of JF635 dye can be a challenge for animal application *in vivo*. We envision two paths for optimizing the use of oROS-HT$_{635}$ in live animals. First, introducing the dye into brain tissue can be aided with engineered solutions such as injection cannulas or drug delivery systems[146,147]. Alternatively, optimization of the oROS-HT$_{635}$ with highly bioavailable dyes (e.g. JF669)[148,149] can be explored for efficient animal applications. Adapting the sensor's reporting mechanism to be more prone to quantum yield change could also improve fluorescence lifetime imaging microscopy (FLIM) compatibility for more quantitative measurement of H_2O_2 *in situ*.

In conclusion, oROS-HT_{635} enables the monitoring of peroxides with high spatiotemporal resolution, offering unparalleled flexibility in its multiplexed application with other optogenetic tools. The rapid kinetics and robust subcellular targeting capabilities of oROS-HT_{635}, particularly at the outer and inner surfaces of the plasma membrane, render it an invaluable tool for investigating peroxide topology near the plasma membrane. When used with fluorescent sensors for various analytes, oROS-HT_{635} facilitates a dynamic, multiparametric analysis of peroxide dynamics and physiological responses in real time with precise spatial information, enhancing the contextual understanding of peroxides in cell physiology.

3.5. Acknowledgments

J.D.L was supported by 1F31DA056121-01A1 and the ISCRM Fellowship. A.B was supported by the Brain Research Foundation, UW Royalty Research Fund, UW ISCRM IPA, NIGMS R01 GM139850-01, P30 DA048736-01-Pilot, NIMH RF1MH130391, NINDS U01NS128537, NIDA R21DA051193 and the McKnight Foundation's Technologies in Neuroscience Award. S.J.W. was supported by the National Science Foundation DGE-2140004 and the Herbold Foundation. K. E was supported by T32AG066574. A.M.A. Was supported by the National Institute of General Medical Sciences grant RM1 GM131981, the National Institute of Arthritis and Musculoskeletal and Skin Diseases grant P30 AR074990, American Heart Association supplement grant AHA872208 and BCTP- NIH – NIBIB - 5T32EB032787-02. We would like to thank the Janelia Materials program from Howard Hughes Medical Institute Janelia research campus for generous sharing of their Janelia Fluors essential for this study. The research received additional support from the Lynn and Mike Garvey Imaging Core, the UW NAPE Center, ISCRM Shared Equipment, Leica Center of Excellence for cellular imaging in Fred Hutch Cancer Research Center (Drs. Hoku West-Foyle, Lena Schroeder). We want to thank Dr. Randy Moon for his support.

3.5.1. Ethics Statement

This study was performed in strict accordance with the recommendations in the Guide for the Care and Use of Laboratory Animals of the National Institutes of Health. All animals were handled according to the approved

Institutional Animal Care and Use Committee (IACUC) protocols #4422-01, #4383-02 of the University of Washington and followed the National Institute of Health and the 25 Association for Assessment and Accreditation of Laboratory Animal Care International guidelines. The University of Washington has an approved Animal Welfare Assurance (#A3464) on file with the National Institute of Health Office of Laboratory Animal Welfare (OLAW), is registered with the United States Department of Agriculture (USDA, certificate #91-R-0001), and is accredited by American Association for Accreditation of Laboratory Animal Care International.

3.5.2. Material request

Plasmids for oROS-HT and its loss-of-function (C199S) and subcellular targeting variants described in this paper will be available through Addgene: pC1-lifeact-oROS-HT (#216420), pC1-IMS-oROS-HT (#216419), pC1-dmito-oROS-HT (#216418), pC1-oROS-HT-CaaX (#216417), pDisplay-oROS-HT (#216416), AAV2_CAG_oROS-HT(C199S)_WPRE (#216415), AAV2_CAG_oROS-HT_WPRE (#216414), pCAG_oROS-HT-WPRE (#216413), pCAG_oROS-HT_LF(C199S)-WPRE (#216412). Authors will also provide plasmids upon request.

3.6. Methods

3.6.1. Molecular Biology

oROS-HT variants were all cloned based on the pC1 plasmid backbone from pC1-HyPer-Red (Addgene ID: 48249) and insertion from pAAV-synapsin-HaloCaMP1a-EGFP (Addgene ID: 138327). Primers for point mutations or fragment assembly required to generate the oROS-HT screening variants were designed for In Vitro Assembly cloning (IVA) technique[82], and they were ordered from Integrated DNA Technologies (IDT). All gene fragment amplifications were done using Superfi-II polymerase (Invitrogen; 12368010). Amplification of the DNA fragment was verified with agarose gel electrophoresis. 30 minutes of DpnI enzyme treatment were done on every PCR product to remove the plasmid template from PCR samples. Circulaization or assembly of the PCR products was achieved with the IVA technique, while the linear DNA products were transformed into

competent E.Coli cells (DH5α or TOP10) and grown on agar plates that contain kanamycin selection antibiotic (50 μg/mL). Upon colony formation, single colonies were picked and grown in 5mL cultures containing LB Broth (Fisher BioReagents; BP9723-2) and selection antibiotic (/kanamycin; 50 μg/mL) overnight (37°C, 230 RPM). DNA was isolated using Machery Nagel DNA prep kits (Machery Nagel; 740490.250). Sanger sequencing (Genewiz; Seattle, WA) or Whole plasmid nanopore sequencing (Plasmidsarus; Eugene, OR) of the isolated plasmid DNA was used to confirm the presence of the intended mutation. Genes encoding the final variants were cloned into a CAG-driven backbone, pCAG-Archon1-KGC-EGFP-ER2-WPRE (Addgene; #108423), using the methods above. All subsequences were verified with Sanger sequencing (Genewiz; Seattle, WA) or Whole plasmid nanopore sequencing (Plasmidsarus; Eugene, OR). Additionally, pC1-CMV-mito-DAAO (Addgene ID: #141132), pC1-SypHer3s-IMS (Addgene ID: #108120) generously provided through Addgene. miniSog1 gene fragment was ordered from Twist Bioscience based on miniSog-C1 (Addgene ID: 54821) and replaced oROS-HT in pC1-dmito-oROS-HT and pDisplay-oROS-HT.

3.6.2. Protein structure prediction and analysis

Protein structure analysis and plotting were performed using Chimera-X-1.2.1. Oxidized [PDB:1I6A] and reduced [PDB:1I69] crystal structures of ecOxyR were imported from the Protein Data Bank (PDB). Pairwise residue distance between reduced and oxidized ecOxyR structure was achieved by aligning both structures using a matchmaker algorithm that superimposes protein structures by creating a pairwise sequence alignment and then fitting the aligned residue pairs to derive pairwise residue distances. The structure of Variant 213-214 was predicted using ColabFold[98]. (msa_method= mmseqs2, homooligomer= 1 or 2, pair_msa= False, max_msa= 512:1024, subsample_msa= True, num_relax= None or 1, use_turbo= True, use_ptm= True, rank_by= pLDDT, num_models= 3 or 5, num_samples= 1, num_ensemble= 1, max_recycles= 6, 24, 48, tol= 0, is_training= False, use_templates= False). The putative position of JF635 was incorporated into the ColabFold prediction of Variant 213-214 to report JF635 bound cpHaloTag structure (PDB:6U2M) with the matchmaker algorithm.

3.6.3. Chemicals

Halotag ligands of Janelia Fluor (JF-HTLs) 635, 585 described in this paper were generously provided by Janelia Materials. Stock solutions of JF-HTLs were prepared in 100% DMSO at 200 μM. Cells described in this study were incubated in 200nM JF-HTL for 1 hour prior to imaging unless specified. While washout of the dyes are not required, we switched the cells into imaging media before imaging. H_2O_2 working solutions were freshly prepared before every experiment from H_2O_2 solution 30 % (w/w) in H_2O (Sigma-Aldrich, H1009). A stock solution of Menadione (Sigma-Aldrich, M9429) was prepared in 100% DMSO at 50mM. A stock solution of Auranofin (Tocris Bioscience, 46-005-0) was prepared in 100% DMSO at 50mM.

3.6.4. Protein purification

oROS-HT was expressed in the NEB BL21(DE3) E. coli strain using the pET29b vector. An overnight LB culture, started from a single colony, was diluted 1:100 in TBII (MpBio) medium supplemented with 50 μg/mL kanamycin. A total of 1500 mL of expression culture was grown at 37 °C for 4 hours, followed by induction with isopropyl-β-D-thiogalactopyranoside (IPTG) and continued culturing at 18 °C for 24 hours with shaking at 225 rpm. Cells were then collected by centrifugation at 4,000 g and resuspended in 50 mM Tris (pH 8.0), 300 mM NaCl, 20 mM imidazole, 1 mM PMSF, 100 μg/mL lysozyme (Sigma-Aldrich), and 10 μg/mL DNase (Sigma-Aldrich). Cells were lysed by sonication and centrifuged at approximately 18,000 g for 30 minutes. The soluble fractions were purified using immobilized metal affinity chromatography with gravity columns packed with Ni-NTA agarose resin (Qiagen). Columns were washed with a buffer containing 20 mM imidazole, and proteins were eluted with a buffer containing 300 mM imidazole and 1.5 mM DTT. Proteins were further purified by size-exclusion chromatography (SEC) using an ÄKTA FPLC instrument equipped with a Superdex 200 Increase 10/300 GL column (GE Healthcare Life Sciences) equilibrated with 25 mM Tris (pH 8.0), 150 mM NaCl and 1.5 mM DTT.

3.6.5. Fluorimetry of oROS-HT_{635} upon attachment with JF635-HTL

Experiments to determine the quantum yield of oROS-HT_{635} were conducted using a FluoroMax-4

spectrofluorometer (Horiba). Prior to measurements, oROS-HT$_{635}$ (1.5 μM) was incubated with JF635-HTL (2 μM) in a solution containing 25 mM Tris (pH 8.0), 150 mM NaCl, and 1.5 mM DTT at room temperature for one hour. To determine the quantum yield of fluorescence of oROS-HT$_{635}$, the emission spectra of the fluorescence excited at 635 nm were measured and compared with the Nile blue dye as standard.

3.6.6. Cellular brightness comparison

Experiments comparing the cellular brightness of oROS-HT$_{635}$ and HyPerRed were conducted using HEK 293 cells expressing eGFP tandem fusions (C-terminus) of each sensor. Imaging was performed on a Stellaris Falcon Confocal system (Leica Microsystems) with an HC PL APO CS2 20x/0.75 DRY objective. Consistent imaging parameters were used across all measurements: unidirectional scan speed (400 Hz), pixel dwell time (1.41 μs), and photon counting mode via the HyD X detector. To minimize autofluorescence artifacts, pixels were Tau-gated for fluorescence lifetimes of 1.04–8 ns. Image segmentation was performed using Cellpose, enabling downstream analysis of average photon counts per cell. For 10 nm spectral peak bandpass-based brightness comparisons between HyPerRed (ex575/em600–610) and oROS-HT$_{635}$ (ex640/em650–660), photon counts were normalized to their respective tandem eGFP (ex488/em508–518) fluorescence. All three fluorophores were excited with ~49 μW laser power from a white light laser (wLL, Leica, set to 85% maximum power). Extracted average photon counts per cell were further corrected for spectral effects (i.e., shorter wavelengths correspond to higher energy photons) and the published photon detection efficiency of the HyD X detector. Lambda scans of oROS-HT$_{635}$ (ex640/em650–800 nm, 10 nm bandpass) and HyPerRed (ex575/em585–735 nm, 10 nm bandpass) were performed using identical arbitrary laser power settings (%). These scans were normalized to the actual excitation photon flux measured with an optical power meter. Finally, photon counts from the lambda scans were normalized to those of each sensor's tandem eGFP.

3.6.7. OSER assay

CytERM-mTurquoise2 (Addgene ID: #98833) CytERM-dTomato (Addgene ID: #98834) was used as negative and positive control, respectively, to perform OSER assay to compare monomericity of oROS-HT$_{635}$ and

HyPerRed. Both sensors were cloned into the CytERM plasmid to be expressed in HEK 293 cells via lipofection. Images for OSER assessment were taken using a Leica SP8 confocal microscope from Imaging Core of Institute of Stem Cell and Regenerative Medicine. Cells with or without whorl structures were manually counted to derive the OSER ratio.

3.6.8. HEK Cell culture and transfection.

Human Embryonic Kidney (HEK293; ATCC Ref: CRL-1573) cells were cultured in Dulbecco's Modified Eagle Medium + GlutaMAX (Gibco; 10569-010) supplemented with 10% fetal bovine serum (Biowest; S1620). When cultures reached 85% confluency, the cultures were seeded at 150,000/75,000 cells per well in 24/48-well plates, respectively. 24 hours after cell seeding, the cells were transfected using Lipofectamine3000 (Invitrogen; L3000015) at 1000/500 ng of DNA per well of a 24/48-well plate, according to the manufacturer's instructions. For dual-transfection experiments, 1:1 (equiv. mass) plasmid cocktails were made for the transfection.

3.6.9. Primary rat neuron isolation

Primary cortical neurons were prepared as previously described[150,151]. Briefly, 24-well tissue culture plates were coated with matrigel (mixed 1:20 in cold-PBS, Corning; 356231) solution and incubated at 4°C overnight before use. Sterile dissection tools were used to isolate cortical brain tissue from P0 rat pups (male and female). Tissue was minced until 1mm pieces remained, then dissociated in equilibrated (37°C, 5% CO2) enzyme (20 U/mL Papain (Worthington Biochemical Corp; LK003176) in 5mL of EBSS (Sigma; E3024)) solution for 30 minutes at 37°C, 5% CO2 humidified incubator. Lysed cells were centrifuged at 200xg for 5 minutes at room temperature, and the supernatant was removed before cells were resuspended in 3 mLs of EBSS (Sigma; E3024). Cells were triturated 24x with a pulled Pasteur pipette in EBSS until homogenous. EBSS was added until the sample volume reached 10 mLs before spinning at 0.7 rcf for 5 minutes at room temperature. The supernatant was removed, and enzymatic dissociation was stopped by resuspending cells in 5 mLs EBSS (Sigma; E3024) + final concentration of 10 mM HEPES Buffer (Fisher; BP299-100) + trypsin inhibitor soybean (1 mg/ml in EBSS at a final concentration of 0.2%; Sigma, T9253) + 60 µl of fetal bovine serum (Biowest;

S1620) + 30 µl 100 U/mL DNase1 (Sigma;11284932001). Cells were washed 2x by spinning at 0.7 rcf for 5 minutes at room temperature and removing supernatant + resuspending in 10 mLs of Neuronal Basal Media (Invitrogen; 10888022) supplemented with B27 (Invitrogen; 17504044) and glutamine (Invitrogen; 35050061) (NBA++). After final wash spin and supernatant removal, cells were resuspended in 10 mLs of NBA++ before counting. Just before neurons were plated, matrigel was aspirated from the wells. Neurons were plated on the prepared culture plates at the desired seeding density. Twenty-four hours after plating, 1 µM AraC (Sigma; C6645) was added to the NBA++ growth media to prevent the growth of glial cells.Plates were incubated at 37°C and 5% CO2 and maintained by exchanging half of the media volume for each well with fresh, warmed Neuronal Basal Media (Invitrogen; 10888022) supplemented with B27 (Invitrogen; 17504044) and glutamine (Invitrogen; 35050061) every three days.

3.6.10. Brain slice imaging

Organotypic whole hemisphere (OWH) rat brain slice preparation: Male rats on postnatal day (P)10 were administered an overdose intraperitoneal injection of pentobarbital (120–150 mg/kg). Animals were then quickly decapitated and whole brains were extracted, cut into hemispheres, and placed into ice-cold dissecting media consisting of 0.64% w/v glucose, 100% Hank's Balanced Salt Solution (HBSS), 1% penicillin–streptomycin. Whole-hemisphere live slices of 300 µm were obtained using a tissue chopper as previously described.[152] Slices were then transferred to 35 mm, 0.4 µm-pore membrane inserts in six-well plates and cultured in 1 ml of 5% heat-inactivated horse-serum slice culture media (SCM) consisting of 50% Minimum Essential Media (MEM), 45% HBSS, 1% GlutaMAX, and 1% penicillin–streptomycin. Slices were cultured in a sterile incubator at constant temperature (37°C), humidity, and CO_2 level (5%).

AAV transduction and confocal imaging: After one day in vitro (DIV), crude AAV9-CAG-oROS-HT prep was added to the slices to be expressed. At the end of the three-day incubation, 1 µM JF635-HTL was added to the slices for an additional 48 hours. OWH brain slices were transferred to 35mm confocal dishes (VWR, 75856-742). Confocal images were acquired with 10x (Nikon Plan Apo 10x Objective, 0.45 numerical aperture)

and 20x (Nikon Plan Apo 10x Objective, 0.75 numerical aperture) magnifications (Nikon Corporation, Minato City, Tokyo, Japan). Brain slice tile scans were obtained with the Cy5 channel before multiple representative images were taken from both the cortex and striatum of each slice. Image acquisition settings were kept consistent before and after the 300 μM H_2O_2 stimulation.

3.6.11. Differentiation of stem cell-derived cardiomyocytes and neurons

hiPSC culture and cardiomyocyte differentiation (diffusion study): Undifferentiated IMR90 (WiCell) hiPSCs were maintained on Matrigel (Corning) coated tissue culture plates in mTeSR1 (Stemcell Technologies). Cardiomyocyte-directed differentiation was performed using a modified small molecule Wnt-modulating protocol using Chiron 99021 and IWP-4 as previously described[83,84]. Lactate enrichment was performed following differentiation to purify hiPSC-CMs[85].

hiPSC culture and cardiomyocyte differentiation (Auranofin study): Undifferentiated human induced pluripotent stem cells (hiPSCs) (WTC11, Male) were maintained on Matrigel (Corning) coated tissue culture plates in mTeSR1 (Stemcell Technologies). Cardiomyocyte-directed differentiation was performed using the RBA-based modified method as previously described[153]. Spontaneous contraction was observed on day 8 post-induction. On day 12 post-induction, media was reduced to 1 mL in preparation for a 45 minutes heat-shock at 42°C on day 13. After heat shock, the media was changed to 1 mL of fresh RMPI+B27+ins. On day 14, cells were dissociated with 0.05% Trypsin (Thermo-Fisher) and frozen in BAMBANKER for storage in LN_2. These cardiomyocytes were thawed in 90% RPMI+B27+ins and 10% Knockout Serum (KSR) with 10 μM ROCK inhibitor and plated on matrigel coated plates. 24 hours after thaw, media was replaced with fresh RPMI+B27+ins and changed every other day.

3.6.12. hiPSC culture and cortical neuron differentiation

Cortical cultures were generated from the previously characterized wild type CV background human induced pluripotent stem cell line[154–156]. Neural progenitor cells (NPCs) from this cell line were differentiated from hiPSCs using dual-SMAD inhibition and NPCs were differentiated into neurons as previously described[155,156]

(Knupp et al., 2020; Shin et al., 2023). Briefly, for cortical culture differentiation from NPCs, NPCs were expanded into 10 cm plates in Basal Neural Maintenance Media (BNMM) (1:1 DMEM/F12 (#11039047 Life Technologies) + glutamine media/neurobasal media (#21103049, GIBCO), 0.5% N2 supplement (# 17502-048; Thermo Fisher Scientific,) 1% B27 supplement (# 17504-044; Thermo Fisher Scientific), 0.5% GlutaMax (# 35050061; Thermo Fisher Scientific), 0.5% insulin-transferrin-selenium (#41400045; Thermo Fisher Scientific), 0.5% NEAA (# 11140050; Thermo Fisher Scientific), 0.2% β-mercaptoethanol (#21985023, Life Technologies) + 20 ng/mL FGF (R&D Systems, Minneapolis, MN). Once the NPCs reached 100% confluence, they were switched to Neural Differentiation Media (BNMM +0.2 mg/mL brain-derived neurotrophic factor (CC# 450–02; PeproTech) + 0.2 mg/mL glial-cell-derived neurotrophic factor (CC# 450–10; PeproTech) + 0.5 M dbcAMP (CC# D0260; Sigma Aldrich). Neural Differentiation Media was changed twice a week for 21 days, at which point the differentiation is considered finished. To isolate neurons from cortical culture, we performed bead sorting purification (#557899; BD BioSciences) selecting against $CD44^+$, $CD184^+$, and $CD271^+$ cells (BD BioSciences; #550989, #557145, #557196, respectively). Purified neurons were plated in a 96-well plate at a density of 200,000 cells per well.

3.6.13. Immunofluorescence staining

Immunofluorescence staining performed for Nrf2 translocation study were done using polyclonal Nrf2 antibody (PA5-27882, Invitrogen) and Donkey anti-Rabbit IgG Alexa Fluor 488 (A21206, Invitrogen). HEK293 cells for each condition were fixed in 4% paraformaldehyde for 15 minutes and permeabilized in 0.2% Triton-x solution for 1 hour. After blocking the fixed cells for 1 hour with 0.5% Bovine Serum Albumin (BSA) blocking buffer in TBST, Cells were then incubated with primary antibodies diluted in the blocking buffer overnight at 4°C. The next day, cells were washed 3 times with PBS. They were then incubated in a secondary antibody solution containing secondary antibodies diluted in 0.5% BSA in PBS overnight at 4°C. Counterstaining was performed with Vectashield containing DAPI (Vector Labs).

3.6.14. Microscopy

Imaging experiments described in this study were performed as follows unless specifically noted. Epifluorescence imaging experiments were performed on a Leica DMI8 microscope (Semrock bandpass filter: GFPratio ex/em: FF01-391-23/FF01-520-35, GFP ex/em: FF01-474-27/FF01-520-35, RFP ex/em:FF01-554-23 or FF01-578-21/FF01-600-37, Far-red ex/em: FF01-635-18/FF01-680-42) controlled by MetaMorph Imaging software, using sCMOS camera (Photometrics Prime95B) and 20x magnification lens (Leica HCX PL FLUOTAR L 20x/0.40 NA CORR) or 10× objective (Leica HC PL FLUOTAR L 10x/0.32 NA) Confocal imaging experiments were performed on Leica SP8 confocal microscope from Imaging Core of Institute of Stem Cell and Regenerative Medicine. Cells were imaged in live cell imaging solution with 10mM glucose (LCIS+, Gibco, A14291DJ). Image analysis methods are described below.

3.6.15. Hypoxic oROS-HT$_{635}$ sensor maturation in HEK293

Two-day post-seeding of HEK293 cells in 24 well plates (150,000 cells/well), culture media was swapped from complete DMEM media (as mentioned above) to complete Fluorobrite DMEM (A1896701, Gibco) with 20mM HEPES. After two hours of acclimation, cells were transfected (Lipofectamine-based, as described above) with pC1-oROS-HT-C199S (Loss-of-function), with 100nM JF635-HTL. Immediately after the transfection, transfected cells were either incubated at 37°C in an atmospheric environment or under hypoxic conditions. For hypoxic conditions, culture plates were transferred into a sealable chamber. The chamber was flushed with N_2 for 10 min at a flow rate of 10 L/min before being placed into the incubator. Approximately 18 hours after, epifluorescence imaging was performed as described earlier.

3.6.16. Multiplexed experiments

oROS-HT/SypHer3s: HEK293 cells were co-transfected with pC1-oROS-HT/pC1-SypHer3s or pC1-oROS-HT-C199S/pC1-SypHer3s as described above. Two days post-transfection, both sensors expressed in HEK293s were imaged using an epifluorescence microscope. The pH change experiment for oROS-HT-C199S were performed with HEK293s in PBS (10010001, Gibco) prepared at pH of 6, 7.44, and 9.

Fluorescence levels for GFP and Far-red profile were captured every 1.5 seconds. Sequential pH-changes plus Menadione applications were performed with HEK293s in PBS (pH 7.44), which was changed to PBS (pH 6) followed by menadione stimulation prepared in PBS (pH 6). Fluorescence levels for GFP and Far-red profile were captured every 2 seconds.

oROS-HT/Grx1-roGFP2: HEK293 cells were co-transfected with pC1-oROS-HT and pC1-Grx1-roGFP2 as described above. Two days post-transfection, both sensors expressed in the cells with live cell imaging solution with 10mM glucose (LCIS+, Gibco, A14291DJ) were imaged using an epifluorescence microscope. For the sequential response of oROS-HT/Grx1-roGFP2 to 10μM H_2O_2, fluorescence level for GFP and Far-red profile were captured every second. For the response to Auranofin, fluorescence levels for GFPratio, GFP, and Far-red profiles were captured every minute.

oROS-HT/Fluo-4: hiPSC-CMs were transfected with pCAG-oROS-HT as described above. Two days post-transfection, cells were incubated with Fluo-4 (Invitrogen, F14201) at 5 μM and JF635-HTL in RPMI + B27+insulin for 1 hour prior to imaging. For the response to Auranofin, fluorescence level of GFP profile (10Hz) and Far-red (0.1Hz) profile were acquired every 10 seconds for hiPSC-CMs in HEPES-buffered RPMI + B27+insulin.

3.6.17. Analysis

Analysis of cell fluorescence imaging data was done by FUSE, a custom cloud-based semi-automated time series fluorescence data analysis platform written in Python. First, the cell segmentation quality of the selected Cellpose[86] model was manually verified. For the segmentation of cells expressing cytosolic fluorescent indicators, model 'cyto' was selected as our base model. If the selected Cellpose model was low-performing, we further trained the Cellpose model using the Cellpose 2.0 human-in-the-loop system[87]. Using an "optimized" segmentation model, fluorescence time-series data is extracted for each region of interest. This allows for unbiased extraction of change in cellular fluorescence information for a complete set of experimental samples. Extracted fluorescence data is normalized as specified in the text using a custom Python script. For

subcellular-targeted oROS-HT$_{635}$, pixels positive for sensor expression were extracted to minimize bias from background pixels, which may arise due to varying morphology.

3.6.18. Computational Cell Scale Modeling

We used an existing model of iPSC-CM membrane kinetics[124] with one modification. Based on experimental observations, the spontaneous beating of the iPSC-CMs was observed to be around 0.5 Hz. To reflect this observation in our computational simulations, we increased the maximal value of the inward rectifier potassium (I_{K1}) by a factor of 1.71484375 in the baseline version of the model. This change resulted in a decrease in spontaneous beating rate from 1.1 Hz to 0.5 Hz. The Kernik model comprises representations of major ionic currents, channels, and pumps (intracellular ionic species tracked: Na^+, K^+, Ca^{2+}). The SR is modeled as a distinct Ca^{2+}-rich intracellular compartment; trafficking of Ca^{2+} ions between the SR and the cytosol is mediated by three ionic fluxes: J_{up} (SR Ca^{2+} re-uptake via the SR Ca^{2+} ATPase [SERCA2a]); J_{rel} (SR Ca^{2+} release via RyR2); and J_{leak} (passive Ca^{2+} leak from the SR into the cytosol). To simulate ROS effects on iPSC-CMs, we ran simulations in which we modified parameters corresponding to maximal efflux via SERCA2a, SR leak amplitude, and maximal conductance of the L-type Ca^{2+} channel (I_{CaL}). The scaling factor for J_{up} (SERCA2a efflux) varied from 0.1 to 1.0 in steps of 0.1. Scaling factors for J_{leak} and I_{CaL} ranged from the default level (1.0) to 2.0 in steps of 0.1. Simulations of bioelectrical activity were conducted using openCARP[157], a cardiac electrophysiology modeling software that is freely available for non-commercial reuse (see: http://opencarp.org/). All simulations were run for 100 seconds of simulated time, which we systematically confirmed was long enough for each perturbed version of the model to achieve a steady state (i.e., zero beat-to-beat variability in membrane voltage or CaT shape). Simulated Ca_i time-series values were post-analyzed with custom-written python scripts. Scripts and files used to run all simulations can be found at the Github repository.

3.7. Appendix (Supplementary Information)

Supplementary Information 1

oROS-HT amino acid sequence

MEMASQQGETMSGPLHIGLIPTVGPYLLPHIIPMLHQTFPKLEMYLHEAQTHQLLAQLDSGKLD

CVILALVKESEAFIEVPLFDEPMLLAIYEDHPWANRECVPMADLAGEKLLMLEDGHCLRDQAMG

FCFEAGALSSTGETFQAFRTTDVGRKLIIDQNVFIEGTLPMGVVRPLTEVEMDHYREPFLNPVDR

EPLWRFPNELPIAGEPANIVALVEEYMDWLHQSPVPKLLFWGTPGVLIPPAEAARLAKSLPNCKA

VDIGPGLNLLQEDNPDLIGSEIARWLSTLEISGGGTGGSGGTGGSGGTGGSMAEIGTGFPFDPHY

VEVLGERMHYVDVGPRDGTPVLFLHGNPTSSYVWRNIIPHVAPTHRCIAPDLIGMGKSDKPDLGY

FFDDHVRFMDAFIEALGLEEVVLVIHDWGSALGFHWAKRNPERVKGIAFMEFIRPIPTWDEWRP

DQLDEDTHFRATSLETLRNMVAAGSGITLLPALAVPPERKRDGVVYLPCIKPEPRRTIGLVYRPGS

PLRSRYEQLAEAIRARMDGHFDKVLKQAV

OxyR cpHaloTag Insertion linkers C199 C208

Supplementary Figure 1 Superimposition of ColabFold predicted structure with resolved structures to estimate fluorophore position.

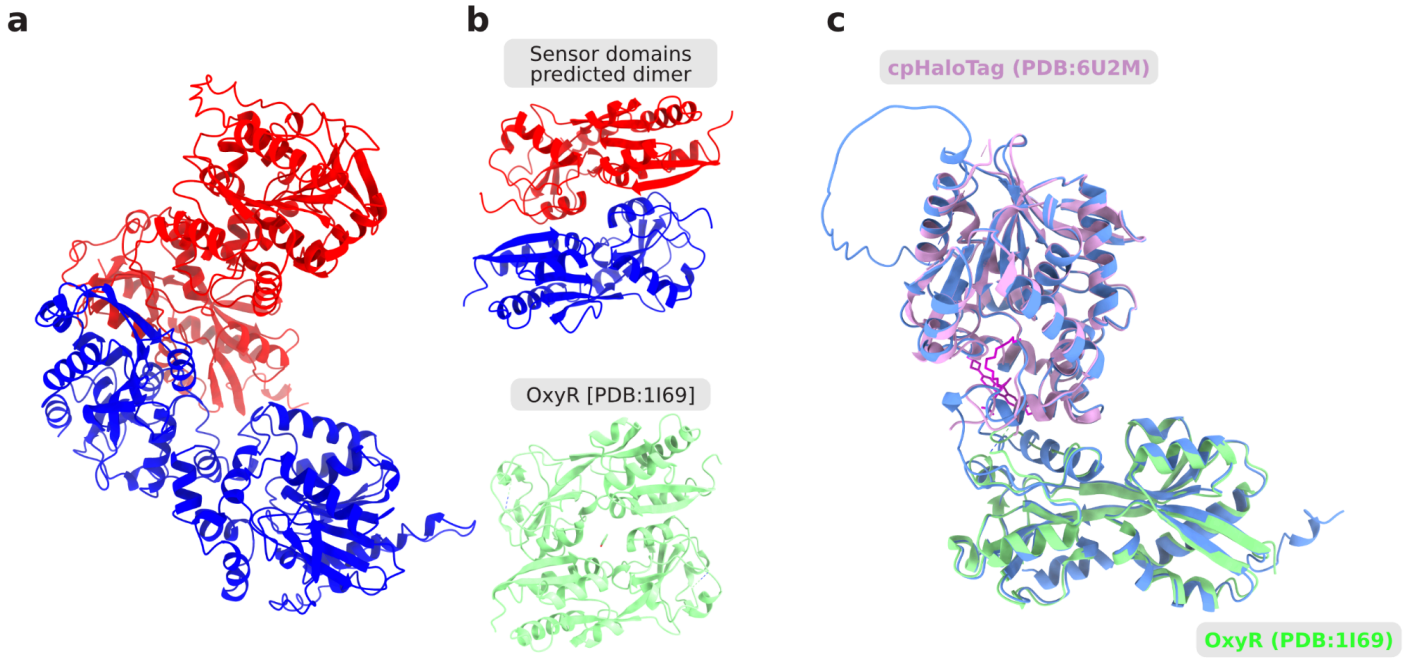

a Structure prediction of cpHaloTag 213-214 insertion variant in a dimeric state using ColabFold (AlphaFold + MMseqs2). **b** ***Top*** Sensing domains (OxyR) of each dimeric pair from cpHaloTag 213-214 insertion variant ColabFold prediction. ***Bottom*** Experimentally resolved crystal structure of reduced OxyR in a dimeric state [PDB:1I69]. **c** Superimposed structures of cpHaloTag 213-214 insertion variant and cpHaloTag with JF635 ligand (reporting domain, extracted from PDB: 6U2M) and OxyR (sensing domain, extracted from PDB: 1I69).

Supplementary Figure 2 ColabFold-guided estimation of domain positioning.

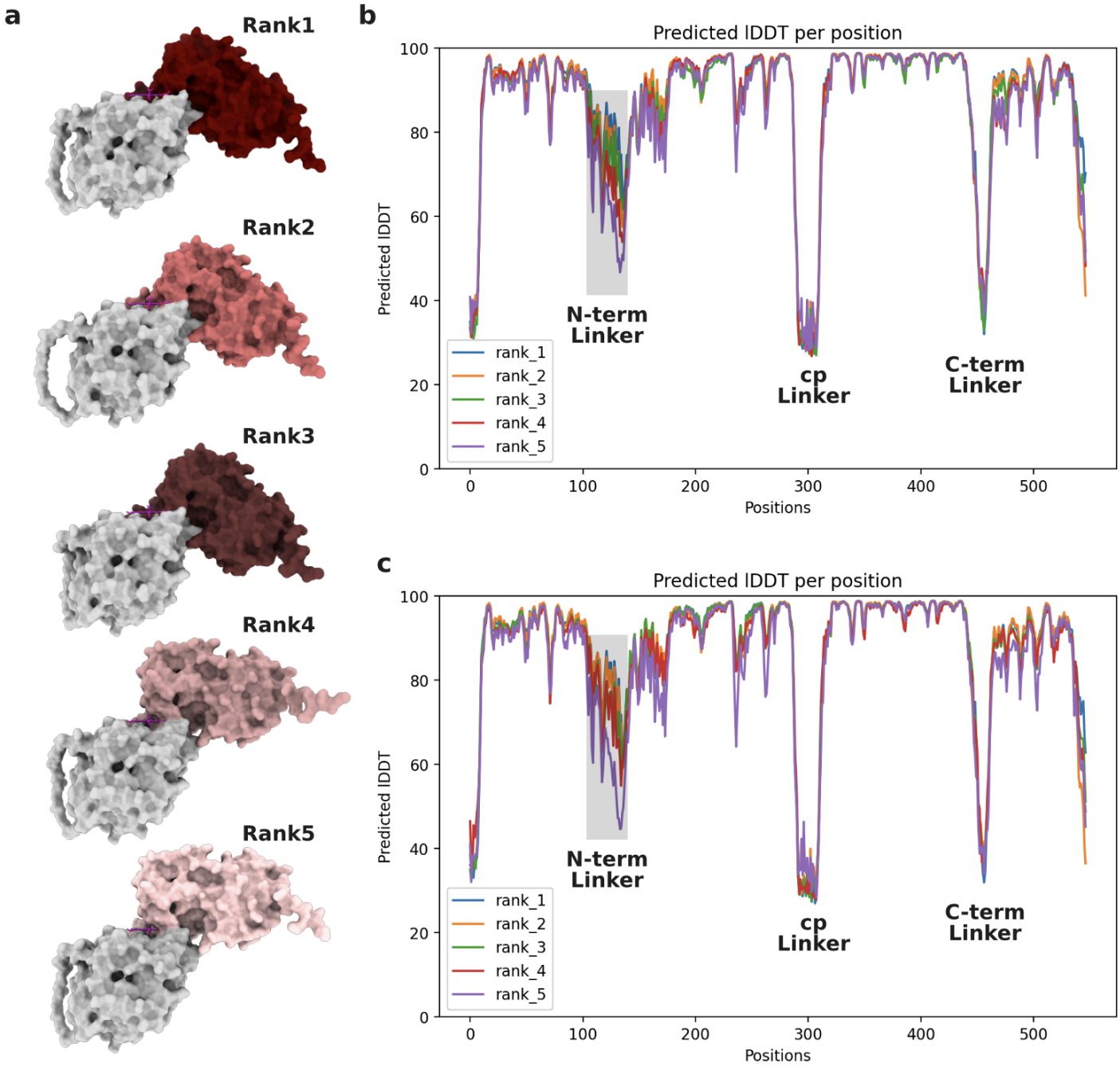

a Surface representation of 5 models predicted for cpHaloTag 213-214 insertion variant. White: cpHaloTag, Red:ecOxyR, Magenta: JF635. **b** "Exposed" domain positioning was more evident for the predictions with higher predicted local distance difference test scores (pLDDT), i.e. higher model confidence. **c** pLDDTs from prediction with higher recycle counts (48), which has been shown to improve the model accuracy. The new prediction also demonstrated a similar trend, where "exposed" domain positioning was more prominent in the predictions with higher pLDDT. Intriguingly, despite the pLDDT of the overall structure being similar across most residues, we observed that the pLDDT of the N-terminus linker arm of cpHaloTag was a major determinant of the overall pLDDT score. This may explain the successful improvement of sensor brightness and dynamics via N-term linker-biased linker optimization (XX-cpHaloTag-X), where we performed random mutagenesis of 2 residues on the N-terminus side of the linker and 1 residue on the C-terminus side of the linker using randomized primers for the sequence assembly.

Supplementary Figure 3 ColabFold-guided identification of mutational hotspot for improved brightness.

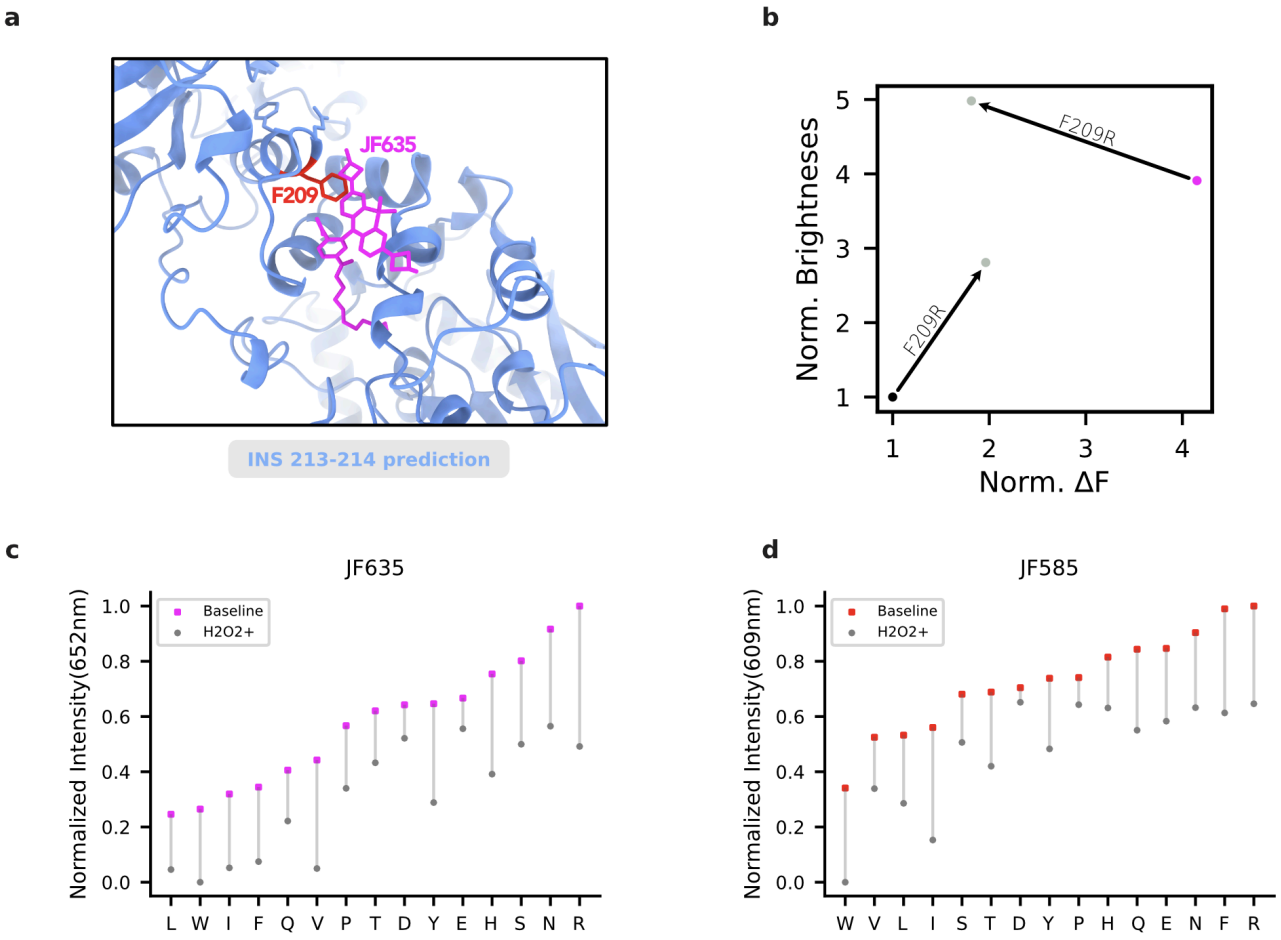

a Proximity of residue F209 to JF635 fluorophore of superimposed cpHaloTag structure. **b** Based on the structure of cpHaloTag 213-214 insertion variant predicted by ColabFold, a mutational target of F209 was identified based on proximity. F209R mutation yielded a higher fluorescence baseline. (black dot). Consistently, F209R yielded higher baseline fluorescence for oROS-HT (magenta dot) but it significantly diminished the dynamic range of the sensor. **c** Mutational screening of residue 209 in cpHaloTag 213-214 insertion variant with JF635 in HEK293 cells. (n>100 cells per variant). **d** Mutational screening of residue 209 in cpHaloTag 213-214 insertion variant with JF585 in HEK293 cells. (n>100 cells per variant).

Supplementary Figure 4 oROS-HT$_{635}$'s response to H_2O_2 from extracellular and intracellular sources.

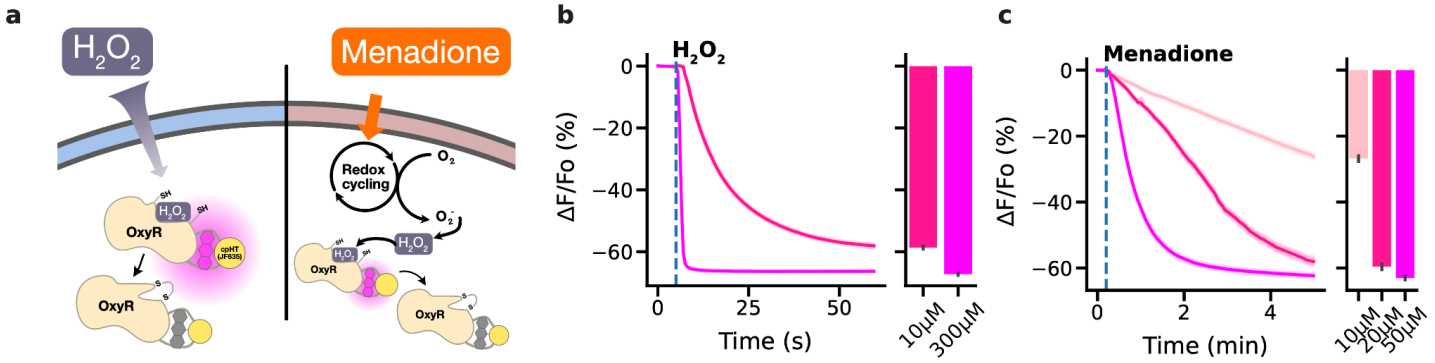

a-c oROS-HT$_{635}$ sensor characterization. **a** Schematic illustration of the methods. oROS-HT$_{635}$'s fluorescence change was characterized by its response to either exogenous H_2O_2 or Menadione (cell-sourced H_2O_2). **b** Fluorescence changes of oROS-HT$_{635}$ upon exogenous administration of high (300 µM) or low (10 µM) H_2O_2. oROS-HT$_{635}$ was expressed in HEK 293 (n>100 cells each). The barplot represents the mean of the maximum fluorescent response of ROI. **c** Fluorescence response of oROS-HT$_{635}$ in HEK 293 to varying concentrations of menadione (n>100 cells each). The barplot represents the mean of the maximum fluorescent response of ROIs. **Statistics:** Error bars and bands represent the bootstrap confidence interval (95%) of the central tendency of values using the Seaborn (0.11.2) statistical plotting package. Cells of interest were collected from three biological replicates unless noted otherwise.

Supplementary Figure 5 OSER assay.

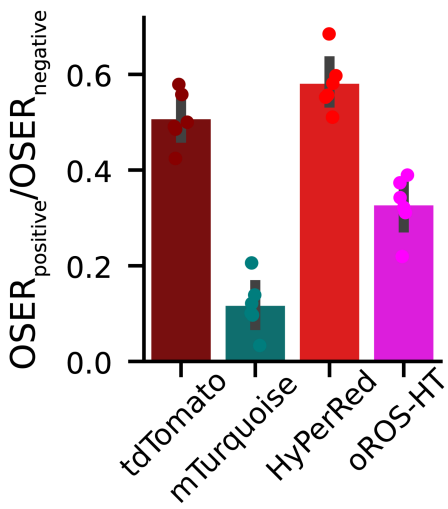

CytERM-HyPerRed and CytERM-oROS-HT635 OSER assay were used to estimate their monomericity. CytERM-tdTomato (dimeric) and CytERM-mTurquoise (monomeric) were used as a reference control. Six biological replicates with more than 100 cells were counted for each experiment. OSER ratio = OSER cells / Normal expression cells. oROS-HT monomericity falls between tdTomato and mTurquoise.

Supplementary Figure 6 Reversibility of oROS-HT$_{635}$.

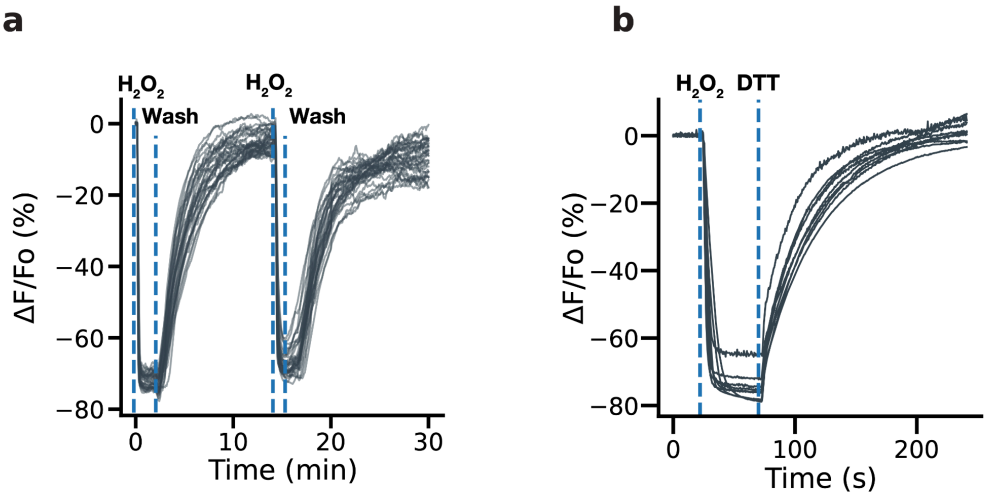

a-b Reversibility of oROS-HT$_{635}$ **a** HEK293 expressing oROS-HT$_{635}$ were stimulated with 100 µM H_2O_2 followed by media wash and 2nd stimulation. (n=32, cells) **b** HEK293 expressing oROS-HT$_{635}$ was first stimulated with 100 µM H_2O_2 and then 10 mM Dithiothreitol (DTT), a reducing agent, shortly after.

Supplementary Figure 7 Fluorescence change of oROS-HT$_{635}$ is H_2O_2 specific.

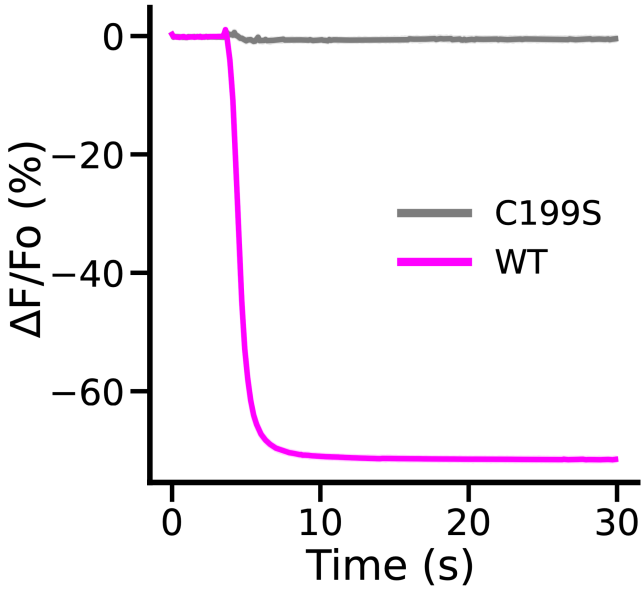

Fluorescence change of oROS-HT$_{635}$ is H_2O_2 specific. Fluorescence response of oROS-HT$_{635}$-WT and oROS-HT$_{635}$-C199S expressed in HEK293 to 300 μM H_2O_2. C199S mutation disables OxyR's H_2O_2 specific C199-C208 disulfide bonding mechanism. oROS-HT$_{635}$-C199S can be utilized as a negative control sensor.

Supplementary Figure 8 Nrf2 translocation quantification.

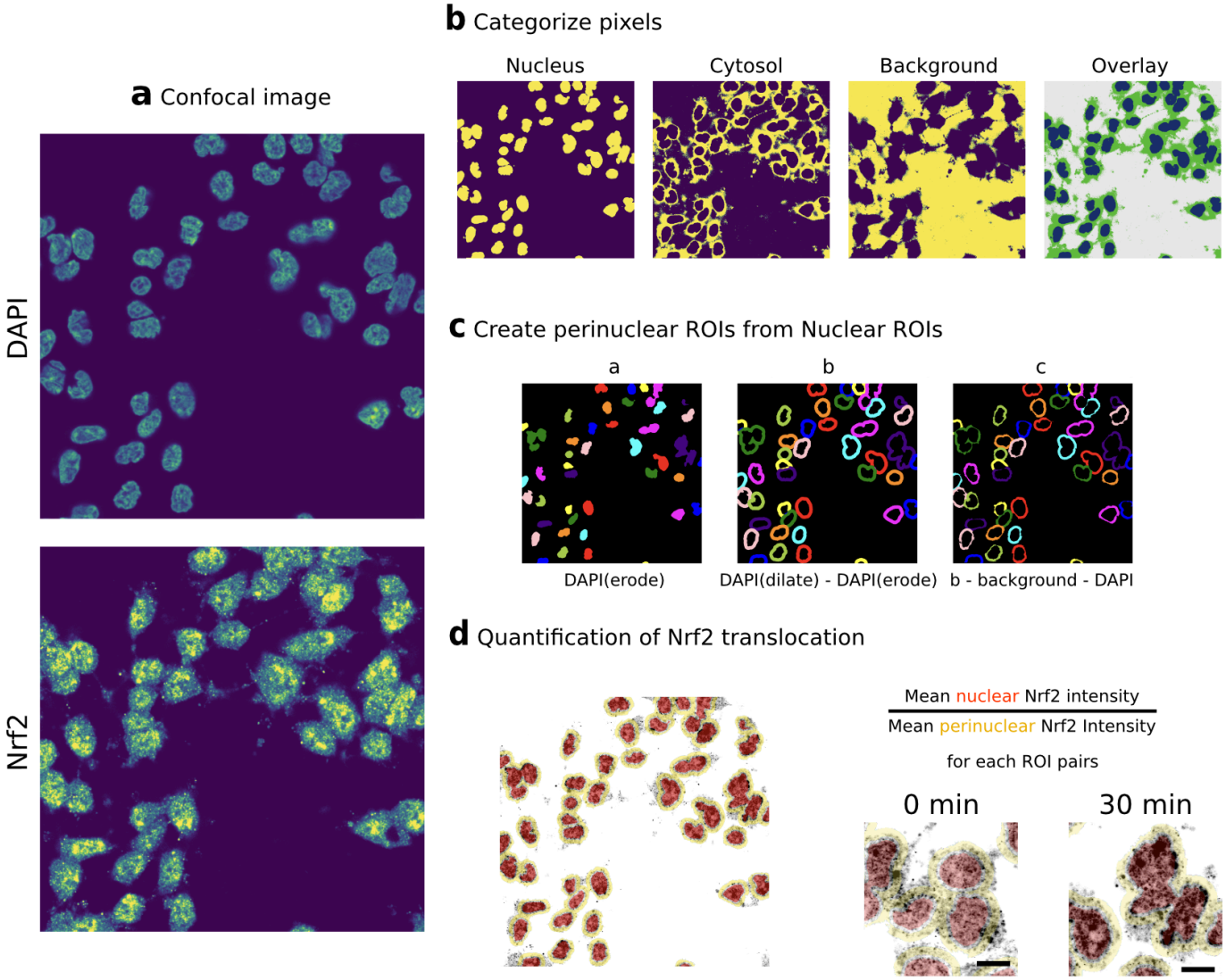

HEK 293 cells were fixed (at 0 or 30 minutes upon Auranofin 1 μM exposure), then an immunofluorescence assay was performed for Nrf2 (see methods section). **a** Next, fixed cells were imaged under a confocal microscope for Nrf2 subcellular localization. Post-processing of the images to quantify Nrf2 translocation was done using a custom analysis method. **b** We sorted each small part of the image (pixel) into three groups. If a pixel is positive for DAPI, it is considered "Nucleus". If the pixel is negative for DAPI but positive for Nrf2, it is considered "Cytosol". Pixels that are not nucleus or cytosol are considered background. **c** We made the region of interest (ROI) that shows the nucleus smaller (eroded, a) to precisely measure how much Nrf2 protein is in the nucleus. We expanded (dilated) the nucleus areas to create a ring around them (b). This "perinuclear ring" was further processed to exclude any pixels that are positive for DAPI or background, which helps us measure the amount of Nrf2 protein outside the nucleus, in the cytosol. **d** Lastly, mean nuclear and perinuclear Nrf2 intensities were calculated. The Nrf2 translocation is represented by the change in their ratio for each nuclear and perinuclear ROI pairs (see **Fig. 4C**). Bottom right images represent cells from 0 and 30 minutes upon Auranofin exposure. Scale bar = 10 μM.

Supplementary Figure 9 Increasing spontaneous beating frequency does not replicate the observed CaT phenotypes.

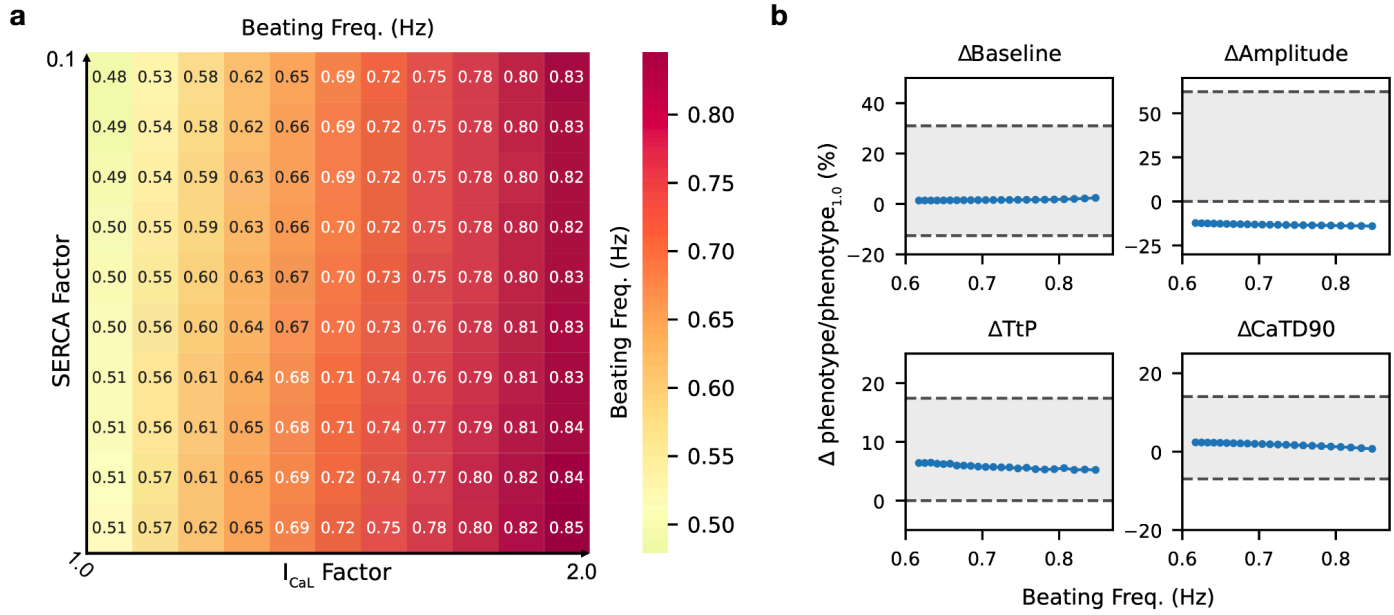

a The synergy map shows the effect of increased I_{CaL} and decreased SERCA uptake on spontaneous beating frequency (Hz). **b** CaT properties over a range of imposed pacing frequencies in the absence of any Ca^{2+} handling model modifications. Dashed lines for each plot represent maximum and minimum Δ phenotype/$phenotype_{1.0}$ (%) for each CaT phenotype reported in Extended Fig. 4d. Change in beating frequency does not have a major effect on CaT properties.

Supplementary Figure 10 Mitochondrial specificity of dMito-oROS-HT$_{635}$.

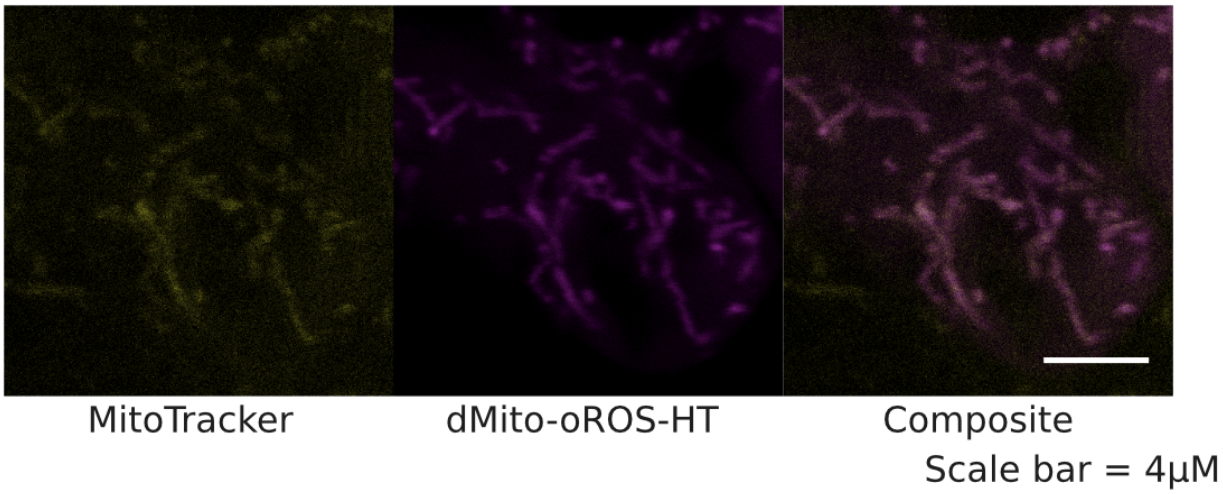

Validation of mitochondrial specificity of dMito-oROS-HT$_{635}$. HEK 293 cells expressing dMito-oROS-HT were stained with MitoTracker Orange CMTMRos for a side-by-side comparison of mitochondrial specificity. HEK 293 cells expressing each of the variants were imaged using a Leica SP8 confocal microscope.

Supplementary Figure 11 Observation of paracrine diffusion of mitochondrial H_2O_2.

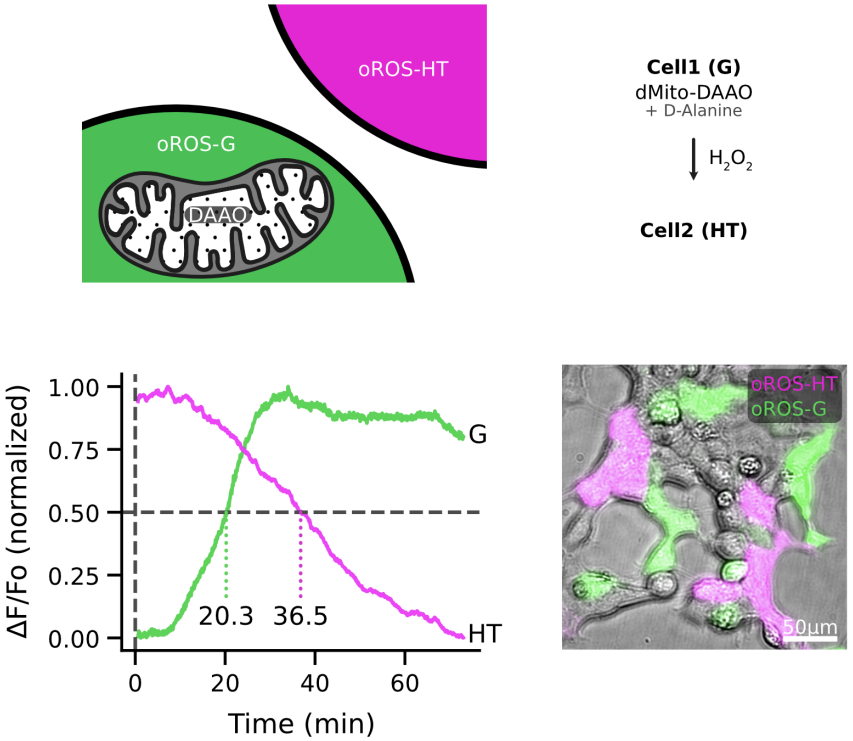

HEK293 cells that are expressed with either dMito-DAAO/oROS-G or oROS-HT_{635} were co-cultured 1 day after the lipofection. Cells were exposed to 50mM D-Alanine at Time (min) = 0. The plot represents fluorescence changes of the whole field-of-view.

Chapter 4. Conclusion

4.1. oROS expands molecular tools for biological H_2O_2 imaging.

This dissertation describes the development of oROS sensor family and their applications that expands our ability to detect real-time H_2O_2 dynamics in biological systems. The second chapter discusses oROS-G, a green fluorescent protein based H_2O_2 sensor, which was the first oROS sensor that exhibited significantly improved sensitivity and kinetics over its predecessors using ecOxyR as their sensing domain for H_2O_2 specific sensing mechanism. oROS-G showed its robust functionality in clinically relevant systems such as mammalian animal models and human stem cell derived models, enabling investigation of changes in H_2O_2 levels in both physiological and pathophysiological context. Specifically, the study showed opioid induced H_2O_2 buildup in kappa-opioid receptor expressing neurons and mu-opioid receptor expressing neurons in Ventral Tegmental Area of using mouse models, confirming induction of H_2O_2 elevation mechanism governed by G-protein biased agonists that were reported to contribute on beta-arrestin independent inactivation mechanism of opioid receptors. oROS-G also demonstrated its utility on validating the therapeutic efficacy of monoamine oxidase-B (MAO-B) inhibitor in mouse astrocyte model, by demonstrating the inhibitor's ability to successfully suppress astrocytic H_2O_2 in the presence of amyloid-beta and putrescine, a GABA precursor, that is reported to contribute to oxidative stress in the Alzhemer's disease.

The third chapter reports the development of oROS-HT_{635}, a bright and far-red chemigenetic fluorescence indicator for H_2O_2, which exhibited the highest sensitivity towards H_2O_2, compared to any OxyR-based H_2O_2 indicator reported by the time of this dissertation's publication. By incorporating recently reported cpHaloTag and Janelia Fluor 635 (JF635) based sensor design, oROS-HT_{635} demonstrates much red-shifted (far-red) 20-fold higher brightness compared to the state-of-the-art red fluorescence indicator for H_2O_2. oROS-HT also comes with many advantages such as compatibility for multicolor imaging, higher resistance for pH and oxygen independent fluorescence mechanism. In this study, we demonstrated

contextually-rich H_2O_2 imaging by performing multicolor imaging of H_2O_2 in conjunction with pH, Ca^{2+}, and redox potential indicators. Specifically, multiplexed monitoring of the effect of Auranofin on Ca^{2+} and H_2O_2 of human iPSC-CMs showed that the acute oxidative stress induced by inhibition of the redox enzymes lead to distinct Ca^{2+} transient (CaT) signatures. With computational modeling of electrophysiology of hiPSC-CMs, we showed that oxidative stress induced perturbation on I_{CaL} and SERCA was sufficient to recapitulate the observed CaT signature, potentially exemplifying the functional immaturity of the hiPSC-CMS. With multiplexed use of oROS-HT_{635} with oROS-G, we demonstrated true multi-site H_2O_2 imaging that enabled visualization of source and the sink of the H_2O_2 production in real-time. Lastly, subcellular targeting of oROS-HT_{635}, especially by the outer and inner plasma membrane space paved a new opportunity to study plasma membrane H_2O_2 biology.

4.2. Contextually enriched imaging of H_2O_2.

As discussed in the introduction, the need to improve precision in studying H_2O_2 biology is greater than ever before[18,39], as it was discussed in a recent experts opinion piece calling for improved methodologies and specificity in studying reactive oxygen species (ROS) in biology. H_2O_2, together with superoxides, are the primary ROS agents that are the most abundant in the aerobic biological system[3]. Relative stability of H_2O_2 compared to other ROS agents makes it a central contributor for redox signaling via different post-translational modifications, and also a pathological biomarker for oxidative stress[36]. Despite increasing evidence of compartmentalized cellular redox environments, most of the ROS detection has been limited to whole-cell or mitochondrial ROS measurements. With the advancement of genetically encoded tools for redox biology, we can ask more questions about H_2O_2 with much greater precision. The flexibility of genetically encoded tools over chemical tracers for detection of ROS enables us to ask questions regarding ROS not necessarily trimmed for limited snapshots of a dynamic system.

4.2.1. Temporal context.

In this study, we showed how menadione, a popular pharmaceutical oxidative stress model, can induce a temporally perplexing outcome for intracellular H_2O_2 level over the course of 10 hours in HEK 293 cells. While

the H_2O_2 level changed in a dose-dependent manner for the first 5 minutes, we observed stronger fluctuation of H_2O_2 level with higher dose of menadione which transiently presented a dose-independent H_2O_2 trend, presumably due to cellular antioxidative defense mechanism, before it recovered dose-dependent trend. Use of chemical ROS tracers with a limited temporal window of detection is not suitable for such dynamic changes, which must be considered in order to improve precision in our understanding of H_2O_2 in biological systems.

4.2.2. Spatial context.

Intriguingly, it is not clear where and how menadione induces generation of ROS. In other words, we lack spatiotemporal precision in understanding how relevant menadione induces oxidative stress models in the context of redox biology and diseases. While multiple reports mitochondria-dependent mechanisms of menadione induced ROS generation in various cell types[51–53], menadione could also lead to faster oxidation of the cytoplasm than of the mitochondria in embryonic chick cardiomyocytes[51], showing that there are compartmentalized differences in the ROS environment yet the source of this complication remains elusive. Intriguingly, there are also contradicting reports regarding the involvement of NADPH oxidase (NOX) for menadione induced ROS generation[158], which calls for cell-specific, and sub compartment-specific understanding of redox biology is critical. Recent advancements in genetically encoded toolkits enabled us to witness true compartmentalized differences in cellular redox environments. For example, Kritsiligkou et al. performed proteome-wide tagging of HyPer7 in yeast to demonstrate how diverse, local, differentiated, and dynamic the H_2O_2 is in the system[130]. Koren et al. and Hoehne et.al. also beautifully demonstrated how genetically encoded tools can decipher diverse locality of H_2O_2 in mammalian cells in nucleus, mitochondrial compartments, and cytoplasm[145,159].

4.2.2. NADPH oxidase.

The NOX family is one of the main contributors of the intracellular H_2O_2 pool by generating superoxide that dismutases into H_2O_2 readily or enzymatically[3]. Specifically, plasma membrane-localized isoforms of NOX create superoxide toward the extracellular side of the cell, which is known as a primary mechanism of oxidative

stress-driven defense against pathogens. Intriguingly, extracellular H_2O_2 from NOX diffuses back into the cytoplasm via aquaporins (AQP)[49,134,160]. Previous studies showed diverse H_2O_2 permeability among aquaporin proteins, where downregulating or upregulating the level of AQP expression led to changes in extracellular to intracellular H_2O_2 ratio[161]. Montiel et al. showed increased AQP1 expression in mouse and human hypertrophic heart tissue. Deletion or pharmacological blockade of AQP1 successfully ameliorated the cardiac hypertrophy phenotype in a mouse model, where they also observed colocalization of AQP1, NOX2, potentially facilitating the influence of NOX2 on its downstream prohypertrophic effectors[46]. Schattauer et al. demonstrated the potential implication of NOX2's involvement in opioid receptor inactivation mechanism by oxidizing Gαi and disrupting Gαi palmitoylation, jamming the G-protein receptor complex in an inactive conformation[6]. Consistently, several studies reported the significant contribution of local plasma membrane H_2O_2 to be highly involved in the membrane receptor modulation, and reported distinct microdomain of H_2O_2 pool proximal to inner plasma membrane[5–7]. Despite growing interesting in understanding membrane H_2O_2 and their role in physiology and pathology, application of existing genetically encoded H_2O_2 monitoring tools were mostly targeted for inner cellular subcompartments such as nucleus, mitochondria, and endoplasmic reticulum.

4.2.3. Plasma membrane H_2O_2.

Dual imaging of membrane-bound oROS-HT_{635} and cytoplasmic oROS-G enabled visualization of faster extracellular H_2O_2 elevation compared to cytoplasmic levels, providing functional evidence of the potential involvement of NOX in menadione-induced oxidative stress. This observation aligns with previous studies on purified enzyme systems, which demonstrated that membrane-bound NOX could oxidize menadione, leading to superoxide formation[162]. This highlights the significance of membrane-targeted H_2O_2 sensors in providing functional biophysical insights specific to plasma membrane-associated H_2O_2. By using the inner plasma membrane-targeted oROS-HT_{635} along with the photosensitizer miniSOG, which generates singlet oxygen and superoxide, we explored the diffusion dynamics of mitochondrial H_2O_2 and outer plasma membrane-derived H_2O_2 toward the inner plasma membrane space. Intriguingly, mitochondrial H_2O_2 exhibited much faster and

more pronounced diffusion toward the inner plasma membrane space, despite the greater physical distance from the mitochondria to the inner plasma membrane compared to the outer plasma membrane. While it is possible that mitochondrial H_2O_2 is more accessible to the inner plasma membrane than extracellularly generated H_2O_2, this phenomenon may reveal a potential limitation in current cell culture-based analyses of cellular redox biology.

4.2.4. Extracellular H_2O_2.

The extracellular concentration of H_2O_2 *in vivo* is widely recognized to be two to three orders of magnitude higher than its intracellular concentration. Nevertheless, studies of cellular redox environments often describe H_2O_2-free extracellular conditions, sometimes supplemented with antioxidants such as pyruvate. Future research should systematically assess how extracellular H_2O_2 influences intracellular redox dynamics. Understanding the role of extracellular H_2O_2 is particularly important for accurately interpreting paracrine or intercellular H_2O_2 signaling (e.g., systemic propagation)[136], which is often considered in degenerative diseases and injuries[14,163] and cellular defense mechanism against them[136]. We co-cultured cells expressing oROS-G/dMito-DAAO with oROS-HT_{635} cells to visualize the paracrine diffusion of mitochondrial H_2O_2 in real time. While this system successfully demonstrated proof-of-concept paracrine H_2O_2 diffusion, we frequently observed H_2O_2 elevation in oROS-G cells (source) without a corresponding increase in oROS-HT cells (sink). These findings suggest that the potential impact of extracellular H_2O_2 has been underappreciated in *in vitro* redox biology models. Thus, there is a need for systematic analyses of how extracellular H_2O_2 affects the biophysics of H_2O_2 dynamics and its downstream effects.

4.2.5. H_2O_2 and interactants.

Despite the dynamic and multifaceted biophysical nature of H_2O_2 and its diverse interactants, current analytic methods face significant limitations due to their reliance on mono-parametric measurements and the lack of integrated, real-time monitoring across multiple parameters. The inability to simultaneously track these changes in cellular physiology, along with their response to various insults, restricts our comprehensive

understanding of H_2O_2-mediated processes and their role in disease pathology. These methodological constraints hinder the development of precise therapeutic strategies and delay our ability to fully elucidate the complex interplay between oxidative stress and cellular homeostasis. The dissertation study described the use of oROS-HT_{635} sensors in conjunction with green fluorescent indicators for different analytes, such as pH, Ca^{2+}, and glutathione redox potential, which enables new opportunities for simultaneous multi parametric study of H_2O_2 and its core interactants *in situ*.

4.2.6. Better precision in understanding H_2O_2 in biology.

The considerable gap between the abundance of evidence demonstrating perturbed redox homeostasis and unsuccessful clinical translation of antioxidative therapeutic strategies calls for alternative perspectives in redox biology research. The development of oROS and its diverse applications, as outlined in this study, represent a critical step forward in refining methods of investigating H_2O_2 dynamics. By offering real-time, site-specific insights into the intricate roles of H_2O_2 in cellular processes and disease mechanisms, oROS not only enhances our ability to probe redox signaling with greater accuracy but also paves the way for more effective therapeutic interventions. This progress expands our conceptual and methodological frameworks, enabling a deeper understanding of H_2O_2 in both normal physiology and pathological states, particularly in clinically relevant biological systems.

5. Reference

1. Falkowski, P. G. *et al.* The rise of oxygen over the past 205 million years and the evolution of large placental mammals. *Science* **309**, 2202–2204 (2005).
2. Koch, L. G. & Britton, S. L. Aerobic metabolism underlies complexity and capacity. *J. Physiol.* **586**, 83–95 (2008).
3. Sies, H. & Jones, D. P. Reactive oxygen species (ROS) as pleiotropic physiological signalling agents. *Nat. Rev. Mol. Cell Biol.* **21**, 363–383 (2020).
4. Henriksen, E. J. Effects of H2O2 on insulin signaling the glucose transport system in mammalian skeletal muscle. *Methods Enzymol.* **528**, 269–278 (2013).
5. Woo, H. A. *et al.* Inactivation of peroxiredoxin I by phosphorylation allows localized H(2)O(2) accumulation for cell signaling. *Cell* **140**, 517–528 (2010).
6. Schattauer, S. S. *et al.* Peroxiredoxin 6 mediates Gαi protein-coupled receptor inactivation by cJun kinase. *Nat. Commun.* **8**, 743 (2017).
7. DeYulia, G. J., Jr, Cárcamo, J. M., Bórquez-Ojeda, O., Shelton, C. C. & Golde, D. W. Hydrogen peroxide generated extracellularly by receptor-ligand interaction facilitates cell signaling. *Proc. Natl. Acad. Sci. U. S. A.* **102**, 5044–5049 (2005).
8. Tan, D. Q. & Suda, T. Reactive oxygen species and mitochondrial homeostasis as regulators of stem cell fate and function. *Antioxid. Redox Signal.* **29**, 149–168 (2018).
9. Oswald, M. C. W., Garnham, N., Sweeney, S. T. & Landgraf, M. Regulation of neuronal development and function by ROS. *FEBS Lett.* **592**, 679–691 (2018).
10. Wilson, C., Muñoz-Palma, E. & González-Billault, C. From birth to death: A role for reactive oxygen species in neuronal development. *Semin. Cell Dev. Biol.* **80**, 43–49 (2018).
11. Birnbaum, J. H. *et al.* Oxidative stress and altered mitochondrial protein expression in the absence of amyloid-β and tau pathology in iPSC-derived neurons from sporadic Alzheimer's disease patients. *Stem*

Cell Res. **27**, 121–130 (2018).

12. Tönnies, E. & Trushina, E. Oxidative stress, synaptic dysfunction, and Alzheimer's disease. *J. Alzheimers. Dis.* **57**, 1105–1121 (2017).
13. Kim, A. C., Lim, S. & Kim, Y. K. Metal ion effects on Aβ and tau aggregation. *Int. J. Mol. Sci.* **19**, 128 (2018).
14. Chun, H. *et al.* Severe reactive astrocytes precipitate pathological hallmarks of Alzheimer's disease via H2O2- production. *Nat. Neurosci.* **23**, 1555–1566 (2020).
15. Binda, C., Hubálek, F., Li, M., Edmondson, D. E. & Mattevi, A. Crystal structure of human monoamine oxidase B, a drug target enzyme monotopically inserted into the mitochondrial outer membrane. *FEBS Lett.* **564**, 225–228 (2004).
16. Schattauer, S. S. *et al.* Reactive oxygen species (ROS) generation is stimulated by κ opioid receptor activation through phosphorylated c-Jun N-terminal kinase and inhibited by p38 mitogen-activated protein kinase (MAPK) activation. *J. Biol. Chem.* **294**, 16884–16896 (2019).
17. Gillis, A. *et al.* Critical Assessment of G Protein-Biased Agonism at the μ-Opioid Receptor. *Trends Pharmacol. Sci.* **41**, 947–959 (2020).
18. Murphy, M. P. *et al.* Guidelines for measuring reactive oxygen species and oxidative damage in cells and in vivo. *Nat Metab* **4**, 651–662 (2022).
19. Iwashita, H., Castillo, E., Messina, M. S., Swanson, R. A. & Chang, C. J. A tandem activity-based sensing and labeling strategy enables imaging of transcellular hydrogen peroxide signaling. *Proc. Natl. Acad. Sci. U. S. A.* **118**, e2018513118 (2021).
20. Li, S., Xiao, Y., Chen, C. & Jia, L. Recent progress in organic small-molecule fluorescent probe detection of hydrogen peroxide. *ACS Omega* **7**, 15267–15274 (2022).
21. Gutscher, Sobotta & Wabnitz. Proximity-based Protein Thiol Oxidation by H2O2-scavenging Peroxidases*♦. *Boll. Soc. Ital. Biol. Sper.*

22. Morgan, B. *et al.* Real-time monitoring of basal H2O2 levels with peroxiredoxin-based probes. *Nat. Chem. Biol.* **12**, 437–443 (2016).

23. Belousov, V. V. *et al.* Genetically encoded fluorescent indicator for intracellular hydrogen peroxide. *Nat. Methods* **3**, 281–286 (2006).

24. Markvicheva, K. N. *et al.* A genetically encoded sensor for H2O2 with expanded dynamic range. *Bioorg. Med. Chem.* **19**, 1079–1084 (2011).

25. Bilan, D. S. *et al.* HyPer-3: a genetically encoded H(2)O(2) probe with improved performance for ratiometric and fluorescence lifetime imaging. *ACS Chem. Biol.* **8**, 535–542 (2013).

26. Ermakova, Y. G. *et al.* Red fluorescent genetically encoded indicator for intracellular hydrogen peroxide. *Nat. Commun.* **5**, 5222 (2014).

27. Subach, O. M. *et al.* Slowly Reducible Genetically Encoded Green Fluorescent Indicator for In Vivo and Ex Vivo Visualization of Hydrogen Peroxide. *Int. J. Mol. Sci.* **20**, (2019).

28. Pak, V. V. *et al.* Ultrasensitive Genetically Encoded Indicator for Hydrogen Peroxide Identifies Roles for the Oxidant in Cell Migration and Mitochondrial Function. *Cell Metab.* **31**, 642–653.e6 (2020).

29. Westerblad, H. & Allen, D. G. Emerging roles of ROS/RNS in muscle function and fatigue. *Antioxid. Redox Signal.* **15**, 2487–2499 (2011).

30. Barnham, K. J., Masters, C. L. & Bush, A. I. Neurodegenerative diseases and oxidative stress. *Nat. Rev. Drug Discov.* **3**, 205–214 (2004).

31. Lee, Y. M., He, W. & Liou, Y.-C. The redox language in neurodegenerative diseases: oxidative post-translational modifications by hydrogen peroxide. *Cell Death Dis.* **12**, 58 (2021).

32. Forrester, S. J., Kikuchi, D. S., Hernandes, M. S., Xu, Q. & Griendling, K. K. Reactive Oxygen Species in Metabolic and Inflammatory Signaling. *Circ. Res.* **122**, 877–902 (2018).

33. D'Autréaux, B. & Toledano, M. B. ROS as signalling molecules: mechanisms that generate specificity in ROS homeostasis. *Nat. Rev. Mol. Cell Biol.* **8**, 813–824 (2007).

34. Schieber, M. & Chandel, N. S. ROS function in redox signaling and oxidative stress. *Curr. Biol.* **24**, R453–62 (2014).

35. Finkel, T. Signal transduction by reactive oxygen species. *J. Cell Biol.* **194**, 7–15 (2011).

36. Sies, H. Hydrogen peroxide as a central redox signaling molecule in physiological oxidative stress: Oxidative eustress. *Redox Biol* **11**, 613–619 (2017).

37. Chen, Q. M., Tu, V. C., Wu, Y. & Bahl, J. J. Hydrogen peroxide dose dependent induction of cell death or hypertrophy in cardiomyocytes. *Arch. Biochem. Biophys.* **373**, 242–248 (2000).

38. Afanas'ev, I. New nucleophilic mechanisms of ros-dependent epigenetic modifications: comparison of aging and cancer. *Aging Dis.* **5**, 52–62 (2014).

39. Sies, H. *et al.* Defining roles of specific reactive oxygen species (ROS) in cell biology and physiology. *Nat. Rev. Mol. Cell Biol.* **23**, 499–515 (2022).

40. Gutscher, M. *et al.* Proximity-based protein thiol oxidation by H2O2-scavenging peroxidases. *J. Biol. Chem.* **284**, 31532–31540 (2009).

41. Pang, Y. *et al.* SHRIMP: Genetically Encoded mScarlet-derived Red Fluorescent Hydrogen Peroxide Sensor with High Brightness and Minimal Photoactivation. *bioRxiv* 2023.08.09.552302 (2023) doi:10.1101/2023.08.09.552302.

42. Lee, C. *et al.* Redox regulation of OxyR requires specific disulfide bond formation involving a rapid kinetic reaction path. *Nat. Struct. Mol. Biol.* **11**, 1179–1185 (2004).

43. Jo, I. *et al.* Structural details of the OxyR peroxide-sensing mechanism. *Proc. Natl. Acad. Sci. U. S. A.* **112**, 6443–6448 (2015).

44. Akerboom, J. *et al.* Optimization of a GCaMP calcium indicator for neural activity imaging. *J. Neurosci.* **32**, 13819–13840 (2012).

45. Bienert, G. P. & Chaumont, F. Aquaporin-facilitated transmembrane diffusion of hydrogen peroxide. *Biochim. Biophys. Acta* **1840**, 1596–1604 (2014).

46. Montiel, V. *et al.* Inhibition of aquaporin-1 prevents myocardial remodeling by blocking the transmembrane transport of hydrogen peroxide. *Sci. Transl. Med.* **12**, (2020).

47. Wragg, D., Leoni, S. & Casini, A. Aquaporin-driven hydrogen peroxide transport: a case of molecular mimicry? *RSC Chem Biol* **1**, 390–394 (2020).

48. Lim, J. B., Langford, T. F., Huang, B. K., Deen, W. M. & Sikes, H. D. A reaction-diffusion model of cytosolic hydrogen peroxide. *Free Radic. Biol. Med.* **90**, 85–90 (2016).

49. Bienert, G. P. *et al.* Specific aquaporins facilitate the diffusion of hydrogen peroxide across membranes. *J. Biol. Chem.* **282**, 1183–1192 (2007).

50. Ledo, A., Fernandes, E., Salvador, A., Laranjinha, J. & Barbosa, R. M. In vivo hydrogen peroxide diffusivity in brain tissue supports volume signaling activity. *Redox Biol* **50**, 102250 (2022).

51. Loor, G. *et al.* Menadione triggers cell death through ROS-dependent mechanisms involving PARP activation without requiring apoptosis. *Free Radic. Biol. Med.* **49**, 1925–1936 (2010).

52. Criddle, D. N. *et al.* Menadione-induced reactive oxygen species generation via redox cycling promotes apoptosis of murine pancreatic acinar cells. *J. Biol. Chem.* **281**, 40485–40492 (2006).

53. Shneyvays, V., Leshem, D., Shmist, Y., Zinman, T. & Shainberg, A. Effects of menadione and its derivative on cultured cardiomyocytes with mitochondrial disorders. *J. Mol. Cell. Cardiol.* **39**, 149–158 (2005).

54. Jan, Y.-H. *et al.* Vitamin K3 (menadione) redox cycling inhibits cytochrome P450-mediated metabolism and inhibits parathion intoxication. *Toxicol. Appl. Pharmacol.* **288**, 114–120 (2015).

55. Ishii, T., Warabi, E. & Mann, G. E. Mechanisms underlying Nrf2 nuclear translocation by non-lethal levels of hydrogen peroxide: p38 MAPK-dependent neutral sphingomyelinase2 membrane trafficking and ceramide/PKCζ/CK2 signaling. *Free Radic. Biol. Med.* **191**, 191–202 (2022).

56. Espinosa-Diez, C. *et al.* Antioxidant responses and cellular adjustments to oxidative stress. *Redox Biol* **6**, 183–197 (2015).

57. Wong, H.-S., Dighe, P. A., Mezera, V., Monternier, P.-A. & Brand, M. D. Production of superoxide and hydrogen peroxide from specific mitochondrial sites under different bioenergetic conditions. *J. Biol. Chem.* **292**, 16804–16809 (2017).

58. Huang, J.-H., Co, H. K., Lee, Y.-C., Wu, C.-C. & Chen, S.-H. Multistability maintains redox homeostasis in human cells. *Mol. Syst. Biol.* **17**, e10480 (2021).

59. Forman, H. J. & Zhang, H. Targeting oxidative stress in disease: promise and limitations of antioxidant therapy. *Nat. Rev. Drug Discov.* **20**, 689–709 (2021).

60. Zhang, Y. *et al.* A comparative genomics study of carbohydrate/glucose metabolic genes: from fish to mammals. *BMC Genomics* **19**, 246 (2018).

61. Audzeyenka, I. *et al.* Hyperglycemia alters mitochondrial respiration efficiency and mitophagy in human podocytes. *Exp. Cell Res.* **407**, 112758 (2021).

62. Klima, J. C. *et al.* Incorporation of sensing modalities into de novo designed fluorescence-activating proteins. *Nat. Commun.* **12**, 856 (2021).

63. Goodman, J. B. *et al.* Redox-Resistant SERCA [Sarco(endo)plasmic Reticulum Calcium ATPase] Attenuates Oxidant-Stimulated Mitochondrial Calcium and Apoptosis in Cardiac Myocytes and Pressure Overload-Induced Myocardial Failure in Mice. *Circulation* **142**, 2459–2469 (2020).

64. Qin, F. *et al.* Cytosolic H2O2 mediates hypertrophy, apoptosis, and decreased SERCA activity in mice with chronic hemodynamic overload. *Am. J. Physiol. Heart Circ. Physiol.* **306**, H1453–63 (2014).

65. Gonnot, F. *et al.* SERCA2 phosphorylation at serine 663 is a key regulator of Ca2+ homeostasis in heart diseases. *Nat. Commun.* **14**, 3346 (2023).

66. Akaike, T. *et al.* A Sarcoplasmic Reticulum Localized Protein Phosphatase Regulates Phospholamban Phosphorylation and Promotes Ischemia Reperfusion Injury in the Heart. *JACC: Basic to Translational Science* **2**, 160–180 (2017).

67. Pedre, B., Barayeu, U., Ezeriņa, D. & Dick, T. P. The mechanism of action of N-acetylcysteine (NAC):

The emerging role of H2S and sulfane sulfur species. *Pharmacol. Ther.* **228**, 107916 (2021).

68. Ezeriņa, D., Takano, Y., Hanaoka, K., Urano, Y. & Dick, T. P. N-Acetyl Cysteine Functions as a Fast-Acting Antioxidant by Triggering Intracellular H2S and Sulfane Sulfur Production. *Cell Chem Biol* **25**, 447–459.e4 (2018).
69. Chun, H., Lim, J., Park, K. D. & Lee, C. J. Inhibition of monoamine oxidase B prevents reactive astrogliosis and scar formation in stab wound injury model. *Glia* **70**, 354–367 (2022).
70. Lee, S. *et al.* Channel-mediated tonic GABA release from glia. *Science* **330**, 790–796 (2010).
71. Jo, S. *et al.* GABA from reactive astrocytes impairs memory in mouse models of Alzheimer's disease. *Nat. Med.* **20**, 886–896 (2014).
72. Jankowsky, J. L. *et al.* Mutant presenilins specifically elevate the levels of the 42 residue beta-amyloid peptide in vivo: evidence for augmentation of a 42-specific gamma secretase. *Hum. Mol. Genet.* **13**, 159–170 (2004).
73. Stanicka, J., Russell, E. G., Woolley, J. F. & Cotter, T. G. NADPH oxidase-generated hydrogen peroxide induces DNA damage in mutant FLT3-expressing leukemia cells. *J. Biol. Chem.* **290**, 9348–9361 (2015).
74. Brewer, T. F., Garcia, F. J., Onak, C. S., Carroll, K. S. & Chang, C. J. Chemical approaches to discovery and study of sources and targets of hydrogen peroxide redox signaling through NADPH oxidase proteins. *Annu. Rev. Biochem.* **84**, 765–790 (2015).
75. Muñoz, M. *et al.* Hydrogen peroxide derived from NADPH oxidase 4- and 2 contributes to the endothelium-dependent vasodilatation of intrarenal arteries. *Redox Biol* **19**, 92–104 (2018).
76. Johnson, F. & Giulivi, C. Superoxide dismutases and their impact upon human health. *Mol. Aspects Med.* **26**, 340–352 (2005).
77. El Daibani, A. *et al.* Molecular mechanism of biased signaling at the kappa opioid receptor. *Nat. Commun.* **14**, 1338 (2023).
78. Schattauer, S. S., Kuhar, J. R., Song, A. & Chavkin, C. Nalfurafine is a G-protein biased agonist having

significantly greater bias at the human than rodent form of the kappa opioid receptor. *Cell. Signal.* **32**, 59–65 (2017).

79. Douglas, A. J. *et al.* Effects of the kappa-opioid agonist U50,488 on parturition in rats. *Br. J. Pharmacol.* **109**, 251–258 (1993).
80. Aslund, F., Zheng, M., Beckwith, J. & Storz, G. Regulation of the OxyR transcription factor by hydrogen peroxide and the cellular thiol-disulfide status. *Proc. Natl. Acad. Sci. U. S. A.* **96**, 6161–6165 (1999).
81. Kritsiligkou, P., Shen, T. K. & Dick, T. P. A comparison of Prx- and OxyR-based H2O2 probes expressed in S. cerevisiae. *J. Biol. Chem.* **297**, 100866 (2021).
82. García-Nafría, J., Watson, J. F. & Greger, I. H. IVA cloning: A single-tube universal cloning system exploiting bacterial In Vivo Assembly. *Sci. Rep.* **6**, 27459 (2016).
83. Lian, X. *et al.* Directed cardiomyocyte differentiation from human pluripotent stem cells by modulating Wnt/β-catenin signaling under fully defined conditions. *Nat. Protoc.* **8**, 162–175 (2013).
84. Bremner, S. B. *et al.* Full-length dystrophin deficiency leads to contractile and calcium transient defects in human engineered heart tissues. *J. Tissue Eng.* **13**, 20417314221119628 (2022).
85. Tohyama, S. *et al.* Distinct metabolic flow enables large-scale purification of mouse and human pluripotent stem cell-derived cardiomyocytes. *Cell Stem Cell* **12**, 127–137 (2013).
86. Stringer, C., Wang, T., Michaelos, M. & Pachitariu, M. Cellpose: a generalist algorithm for cellular segmentation. *Nat. Methods* **18**, 100–106 (2021).
87. Pachitariu, M. & Stringer, C. Cellpose 2.0: how to train your own model. *Nat. Methods* **19**, 1634–1641 (2022).
88. Woo, D. H. *et al.* TREK-1 and Best1 channels mediate fast and slow glutamate release in astrocytes upon GPCR activation. *Cell* **151**, 25–40 (2012).
89. Ren, X. *et al.* Redox Signaling Mediated by Thioredoxin and Glutathione Systems in the Central Nervous System. *Antioxid. Redox Signal.* **27**, 989–1010 (2017).

90. Marinho, H. S., Real, C., Cyrne, L., Soares, H. & Antunes, F. Hydrogen peroxide sensing, signaling and regulation of transcription factors. *Redox Biol* **2**, 535–562 (2014).

91. Halliwell, B. Understanding mechanisms of antioxidant action in health and disease. *Nat. Rev. Mol. Cell Biol.* (2023) doi:10.1038/s41580-023-00645-4.

92. Kishi, S., Nagasu, H., Kidokoro, K. & Kashihara, N. Oxidative stress and the role of redox signalling in chronic kidney disease. *Nat. Rev. Nephrol.* (2023) doi:10.1038/s41581-023-00775-0.

93. Eid, M., Barayeu, U., Sulková, K., Aranda-Vallejo, C. & Dick, T. P. Using the heme peroxidase APEX2 to probe intracellular H2O2 flux and diffusion. *Nat. Commun.* **15**, 1239 (2024).

94. Patriarchi, T. *et al.* An expanded palette of dopamine sensors for multiplex imaging in vivo. *Nat. Methods* **17**, 1147–1155 (2020).

95. Dana, H. *et al.* Sensitive red protein calcium indicators for imaging neural activity. *Elife* **5**, (2016).

96. Wu, J. *et al.* Improved orange and red Ca^{2}± indicators and photophysical considerations for optogenetic applications. *ACS Chem. Neurosci.* **4**, 963–972 (2013).

97. Ning, L. *et al.* A Bright, Nontoxic, and Non-aggregating red Fluorescent Protein for Long-Term Labeling of Fine Structures in Neurons. *Front Cell Dev Biol* **10**, 893468 (2022).

98. Mirdita, M. *et al.* ColabFold: making protein folding accessible to all. *Nat. Methods* **19**, 679–682 (2022).

99. Pedre, B. *et al.* Structural snapshots of OxyR reveal the peroxidatic mechanism of H_2O_2 sensing. *Proc. Natl. Acad. Sci. U. S. A.* **115**, E11623–E11632 (2018).

100. Tao, K. In vivo oxidation-reduction kinetics of OxyR, the transcriptional activator for an oxidative stress-inducible regulon in Escherichia coli. *FEBS Lett.* **457**, 90–92 (1999).

101. Lee, J. D. *et al.* Structure-guided engineering of a fast genetically encoded sensor for real-time H2O2 monitoring. *bioRxiv* 2024.01.31.578117 (2024) doi:10.1101/2024.01.31.578117.

102. Choi, H. *et al.* Structural basis of the redox switch in the OxyR transcription factor. *Cell* **105**, 103–113 (2001).

103. Fenno, L. E. *et al.* Comprehensive Dual- and Triple-Feature Intersectional Single-Vector Delivery of Diverse Functional Payloads to Cells of Behaving Mammals. *Neuron* **107**, 836–853.e11 (2020).

104. Deo, C. *et al.* The HaloTag as a general scaffold for far-red tunable chemigenetic indicators. *Nat. Chem. Biol.* **17**, 718–723 (2021).

105. Grimm, J. B. *et al.* A general method to fine-tune fluorophores for live-cell and in vivo imaging. *Nat. Methods* **14**, 987–994 (2017).

106. Tongul, B. & Tarhan, L. The effect of menadione-induced oxidative stress on the in vivo reactive oxygen species and antioxidant response system of Phanerochaete chrysosporium. *Process Biochem.* **49**, 195–202 (2014).

107. Heppert, J. K. *et al.* Comparative assessment of fluorescent proteins for in vivo imaging in an animal model system. *Mol. Biol. Cell* **27**, 3385–3394 (2016).

108. Campbell, B. C. *et al.* mGreenLantern: a bright monomeric fluorescent protein with rapid expression and cell filling properties for neuronal imaging. *Proc. Natl. Acad. Sci. U. S. A.* **117**, 30710–30721 (2020).

109. Application Note: The Power HyD family of detectors. https://www.nature.com/articles/d42473-020-00398-0.

110. Lambert, T. J. FPbase: a community-editable fluorescent protein database. *Nat. Methods* **16**, 277–278 (2019).

111. Yamada, Y. & Mikoshiba, K. Quantitative comparison of novel GCaMP-type genetically encoded Ca2+ indicators in mammalian neurons. *Front Cell Neurosci* **6**, 1–9 (2012).

112. Han, L. *et al.* RFP tags for labeling secretory pathway proteins. *Biochem. Biophys. Res. Commun.* **447**, 508–512 (2014).

113. Abdelfattah, A. S. *et al.* A bright and fast red fluorescent protein voltage indicator that reports neuronal activity in organotypic brain slices. *J. Neurosci.* **36**, 2458–2472 (2016).

114. Taniguchi, J. *et al.* Comment on ‘Accumbens cholinergic interneurons dynamically promote dopamine

release and enable motivation'. *Elife* **13**, (2024).

115. Heim, R., Prasher, D. C. & Tsien, R. Y. Wavelength mutations and posttranslational autoxidation of green fluorescent protein. *Proc. Natl. Acad. Sci. U. S. A.* **91**, 12501–12504 (1994).
116. Ma, Y., Sun, Q. & Smith, S. C. The mechanism of oxidation in chromophore maturation of wild-type green fluorescent protein: a theoretical study. *Phys. Chem. Chem. Phys.* **19**, 12942–12952 (2017).
117. Takahashi, E. *et al.* Genetic oxygen sensor: GFP as an indicator of intracellular oxygenation. *Adv. Exp. Med. Biol.* **566**, 39–44 (2005).
118. Covas, G., Marinho, H. S., Cyrne, L. & Antunes, F. Chapter Nine - Activation of Nrf2 by H2O2: De Novo Synthesis Versus Nuclear Translocation. in *Methods in Enzymology* (eds. Cadenas, E. & Packer, L.) vol. 528 157–171 (Academic Press, 2013).
119. Görlach, A., Bertram, K., Hudecova, S. & Krizanova, O. Calcium and ROS: A mutual interplay. *Redox Biol* **6**, 260–271 (2015).
120. Nikolaienko, R., Bovo, E. & Zima, A. V. Redox Dependent Modifications of Ryanodine Receptor: Basic Mechanisms and Implications in Heart Diseases. *Front. Physiol.* **9**, 1775 (2018).
121. Johnstone, V. P. A. & Hool, L. C. Glutathionylation of the L-type Ca2+ channel in oxidative stress-induced pathology of the heart. *Int. J. Mol. Sci.* **15**, 19203–19225 (2014).
122. Varghese, E. & Büsselberg, D. Auranofin, an Anti-Rheumatic Gold Compound, Modulates Apoptosis by Elevating the Intracellular Calcium Concentration ([Ca2+]i) in MCF-7 Breast Cancer Cells. *Cancers* **6**, 2243–2258 (2014).
123. Harper, M. T. Auranofin, a thioredoxin reductase inhibitor, causes platelet death through calcium overload. *Platelets* **30**, 98–104 (2019).
124. Kernik, D. C. *et al.* A computational model of induced pluripotent stem-cell derived cardiomyocytes incorporating experimental variability from multiple data sources. *J. Physiol.* **597**, 4533–4564 (2019).
125. Lee, Y.-K. *et al.* Calcium homeostasis in human induced pluripotent stem cell-derived cardiomyocytes.

Stem Cell Rev Rep **7**, 976–986 (2011).

126. Tu, C., Chao, B. S. & Wu, J. C. Strategies for Improving the Maturity of Human Induced Pluripotent Stem Cell-Derived Cardiomyocytes. *Circ. Res.* **123**, 512–514 (2018).
127. Goversen, B., van der Heyden, M. A. G., van Veen, T. A. B. & de Boer, T. P. The immature electrophysiological phenotype of iPSC-CMs still hampers in vitro drug screening: Special focus on IK1. *Pharmacol. Ther.* **183**, 127–136 (2018).
128. Itzhaki, I. *et al.* Calcium handling in human induced pluripotent stem cell derived cardiomyocytes. *PLoS One* **6**, e18037 (2011).
129. Koivumäki, J. T. *et al.* Structural Immaturity of Human iPSC-Derived Cardiomyocytes: In Silico Investigation of Effects on Function and Disease Modeling. *Front. Physiol.* **9**, 80 (2018).
130. Kritsiligkou, P. *et al.* Proteome-wide tagging with an H_2O_2 biosensor reveals highly localized and dynamic redox microenvironments. *Proc. Natl. Acad. Sci. U. S. A.* **120**, e2314043120 (2023).
131. Terzi, A. & Suter, D. M. The role of NADPH oxidases in neuronal development. *Free Radic. Biol. Med.* **154**, 33–47 (2020).
132. Ma, M. W. *et al.* NADPH oxidase in brain injury and neurodegenerative disorders. *Mol. Neurodegener.* **12**, 7 (2017).
133. Schröder, K. NADPH oxidases: Current aspects and tools. *Redox Biol* **34**, 101512 (2020).
134. Miller, E. W., Dickinson, B. C. & Chang, C. J. Aquaporin-3 mediates hydrogen peroxide uptake to regulate downstream intracellular signaling. *Proc. Natl. Acad. Sci. U. S. A.* **107**, 15681–15686 (2010).
135. Thiagarajah, J. R., Chang, J., Goettel, J. A., Verkman, A. S. & Lencer, W. I. Aquaporin-3 mediates hydrogen peroxide-dependent responses to environmental stress in colonic epithelia. *Proc. Natl. Acad. Sci. U. S. A.* **114**, 568–573 (2017).
136. Haskew-Layton, R. E. *et al.* Controlled enzymatic production of astrocytic hydrogen peroxide protects neurons from oxidative stress via an Nrf2-independent pathway. *Proc. Natl. Acad. Sci. U. S. A.* **107**,

17385–17390 (2010).

137. Niemczyk, E. *et al.* A possible involvement of plasma membrane NAD(P)H oxidase in the switch mechanism of the cell death mode from apoptosis to necrosis in menadione-induced cell injury. *Acta Biochim. Pol.* **51**, 1015–1022 (2004).

138. Thor, H. *et al.* The metabolism of menadione (2-methyl-1,4-naphthoquinone) by isolated hepatocytes. A study of the implications of oxidative stress in intact cells. *J. Biol. Chem.* **257**, 12419–12425 (1982).

139. Yamashoji, S., Ikeda, T. & Yamashoji, K. Extracellular generation of active oxygen species catalyzed by exogenous menadione in yeast cell suspension. *Biochim. Biophys. Acta* **1059**, 99–105 (1991).

140. Suzuki, Y. & Ono, Y. Involvement of reactive oxygen species produced via NADPH oxidase in tyrosine phosphorylation in human B- and T-lineage lymphoid cells. *Biochem. Biophys. Res. Commun.* **255**, 262–267 (1999).

141. Shu, X. *et al.* A genetically encoded tag for correlated light and electron microscopy of intact cells, tissues, and organisms. *PLoS Biol.* **9**, e1001041 (2011).

142. Barnett, M. E., Baran, T. M., Foster, T. H. & Wojtovich, A. P. Quantification of light-induced miniSOG superoxide production using the selective marker, 2-hydroxyethidium. *Free Radic. Biol. Med.* **116**, 134–140 (2018).

143. Seo, M. J. *et al.* Dual inhibition of thioredoxin reductase and proteasome is required for auranofin-induced paraptosis in breast cancer cells. *Cell Death Dis.* **14**, 42 (2023).

144. Renken, S. *et al.* Targeting of Nrf2 improves antitumoral responses by human NK cells, TIL and CAR T cells during oxidative stress. *J Immunother Cancer* **10**, (2022).

145. Koren, S. A. *et al.* All-optical spatiotemporal mapping of ROS dynamics across mitochondrial microdomains in situ. *Nat. Commun.* **14**, 6036 (2023).

146. Xu, C., Peng, B. & Liu, S. Using intra-brain drug infusion to investigate neural mechanisms underlying reward-seeking behavior in mice. *STAR Protoc* **3**, 101221 (2022).

147. Xavier, A. L. R. *et al.* Cannula Implantation into the Cisterna Magna of Rodents. *J. Vis. Exp.* (2018) doi:10.3791/57378.

148. Farrants, H. *et al.* A modular chemigenetic calcium indicator enables in vivo functional imaging with near-infrared light. *bioRxiv* (2023) doi:10.1101/2023.07.18.549527.

149. Grimm, J. B. *et al.* A general method to optimize and functionalize red-shifted rhodamine dyes. *Nat. Methods* **17**, 815–821 (2020).

150. Catapano, L. A., Arnold, M. W., Perez, F. A. & Macklis, J. D. Specific neurotrophic factors support the survival of cortical projection neurons at distinct stages of development. *J. Neurosci.* **21**, 8863–8872 (2001).

151. Martin, D. L. Synthesis and release of neuroactive substances by glial cells. *Glia* **5**, 81–94 (1992).

152. McKenna, M. *et al.* Organotypic whole hemisphere brain slice models to study the effects of donor age and oxygen-glucose-deprivation on the extracellular properties of cortical and striatal tissue. *J. Biol. Eng.* **16**, 14 (2022).

153. Yoo, D. *Studying the Role of Mechanical Contraction in Cardiac Muscle Development Using Genetically Engineered Non-Contractile Human Stem Cell-Derived Cardiomyocytes*. (2021).

154. Young, J. E. *et al.* Elucidating molecular phenotypes caused by the SORL1 Alzheimer's disease genetic risk factor using human induced pluripotent stem cells. *Cell Stem Cell* **16**, 373–385 (2015).

155. Shin, Y. J. *et al.* Amyloid beta peptides (Aβ) from Alzheimer's disease neuronal secretome induce endothelial activation in a human cerebral microvessel model. *Neurobiol. Dis.* **181**, 106125 (2023).

156. Knupp, A. *et al.* Depletion of the AD Risk Gene SORL1 Selectively Impairs Neuronal Endosomal Traffic Independent of Amyloidogenic APP Processing. *Cell Rep.* **31**, 107719 (2020).

157. Plank, G. *et al.* The openCARP simulation environment for cardiac electrophysiology. *Comput. Methods Programs Biomed.* **208**, 106223 (2021).

158. Sakane, F., Takahashi, K. & Koyama, J. Purification and characterization of a membrane-bound

NADPH-cytochrome c reductase capable of catalyzing menadione-dependent O2- formation in guinea pig polymorphonuclear leukocytes. *J. Biochem.* **96**, 671–678 (1984).

159. Hoehne, M. N. *et al.* Spatial and temporal control of mitochondrial H2 O2 release in intact human cells. *EMBO J.* **41**, e109169 (2022).
160. Fisher, A. B. Redox signaling across cell membranes. *Antioxid. Redox Signal.* **11**, 1349–1356 (2009).
161. Carmona, M. *et al.* Monitoring cytosolic H2O2 fluctuations arising from altered plasma membrane gradients or from mitochondrial activity. *Nat. Commun.* **10**, 4526 (2019).
162. Nisimoto, Y., Tamura, M. & Lambeth, J. D. A menadione-stimulated pyridine nucleotide oxidase from resting bovine neutrophil membranes. Purification, properties, and immunochemical cross-reactivity with the human neutrophil NADPH oxidase. *J. Biol. Chem.* **263**, 11657–11663 (1988).
163. Mittal, M., Siddiqui, M. R., Tran, K., Reddy, S. P. & Malik, A. B. Reactive oxygen species in inflammation and tissue injury. *Antioxid. Redox Signal.* **20**, 1126–1167 (2014).